
# ON THE INERTIA OF POWER ELECTRONICS CONVERTERS

André Ramos de Castro

Tese de Doutorado apresentada ao Programa de Pós-graduação em Engenharia Elétrica, COPPE, da Universidade Federal do Rio de Janeiro, como parte dos requisitos necessários à obtenção do título de Doutor em Engenharia Elétrica.

Orientador: Mauricio Aredes

Rio de Janeiro
Setembro de 2018

ON THE INERTIA OF POWER ELECTRONICS CONVERTERS

André Ramos de Castro

TESE SUBMETIDA AO CORPO DOCENTE DO INSTITUTO ALBERTO LUIZ COIMBRA DE PÓS-GRADUAÇÃO E PESQUISA DE ENGENHARIA (COPPE) DA UNIVERSIDADE FEDERAL DO RIO DE JANEIRO COMO PARTE DOS REQUISITOS NECESSÁRIOS PARA A OBTENÇÃO DO GRAU DE DOUTOR EM CIÊNCIAS EM ENGENHARIA ELÉTRICA.

Examinada por:

Prof. Mauricio Aredes, Dr.-Ing.

Prof. Luís Guilherme Barbosa Rolim, Dr.-Ing.

Prof. Glauco Nery Taranto, Ph.D.

Prof. Vitor Hugo Ferreira, D.Sc.

Prof. Denizar Cruz Martins, Dr. Ing.

RIO DE JANEIRO, RJ – BRASIL
SETEMBRO DE 2018

Castro, André Ramos de

On the inertia of power electronics converters/André Ramos de Castro. – Rio de Janeiro: UFRJ/COPPE, 2018.

XXII, 144 p.: il.; 29, 7cm.

Orientador: Mauricio Aredes

Tese (doutorado) – UFRJ/COPPE/Programa de Engenharia Elétrica, 2018.

Referências Bibliográficas: p. 127 – 135.

1. Frequency stability. 2. Inertia. 3. Synchronverter. 4. Frequency stability contribution. I. Aredes, Mauricio. II. Universidade Federal do Rio de Janeiro, COPPE, Programa de Engenharia Elétrica. III. Título.

*Dedico este trabalho à minha esposa, Mariana.*

# Agradecimentos

Aos meus pais, Heitor e Margarida, pelo apoio incondicional em toda a minha trajetória.

À minha esposa e amiga, Mariana, por estar sempre ao meu lado.

Ao meu orientador, Professor Mauricio Aredes, pelas oportunidades, pela confiança e pela amizade durante meu período de estudos dentro de seu laboratório.

Aos meus colegas de laboratório, Jorge Caicedo, pelas muitas discussões, pelo aprendizado, pela amizade e pelo apoio fundamental à conclusão deste trabalho; Leonardo Silva, pelo aprendizado essencial ao trabalho em bancada experimental, pelo companheirismo e pela amizade; Juliano Caldeira, Emanuel van Emmerik, Bruno França e Gustavo Figueiredo, pelas discussões e pelos trabalhos em conjunto ao longo dos anos.

O presente trabalho foi realizado com apoio do CNPq, Conselho Nacional de Desenvolvimento Científico e Tecnológico - Brasil.

Resumo da Tese apresentada à COPPE/UFRJ como parte dos requisitos necessários para a obtenção do grau de Doutor em Ciências (D.Sc.)

# SOBRE A INÉRCIA DE CONVERSORES ELETRÔNICOS DE POTÊNCIA

André Ramos de Castro

Setembro/2018

Orientador: Mauricio Aredes

Programa: Engenharia Elétrica

Os sistemas elétricos de potência passam por um momento de transição da matriz energética. Crescem em número as unidades de geração baseadas em fontes renováveis de energia e as unidades de geração distribuída. Há uma preocupação entre acadêmicos e operadores do sistema elétrico de que a falta da inércia de uma massa girante nessas novas unidades geradoras contribua negativamente para a estabilidade de frequência de sistemas elétricos de potência. Entretanto, não há um meio adequado estabelecido de quantificar a contribuição de uma unidade geradora baseada em eletrônica de potência à estabilidade de frequência da rede. Este trabalho busca a definição de tal meio e a análise de técnicas de controle sob a perspectiva da contribuição à estabilidade de frequência de sistemas elétricos de potência.

Abstract of Thesis presented to COPPE/UFRJ as a partial fulfillment of the requirements for the degree of Doctor of Science (D.Sc.)

ON THE INERTIA OF POWER ELECTRONICS CONVERTERS

André Ramos de Castro

September/2018

Advisor: Mauricio Aredes

Department: Electrical Engineering

Electrical power systems are going through a transition in its energy matrix. Renewable energy sources based generation and distributed generation grow in number. There is a concern among academics and system operators that the lack of spinning mass' inertia in these new generating units will negatively contribute to frequency stability in electrical power systems. However, there is not an adequate established method for quantifying the contribution a power electronics based generating unit provides to grid frequency stability. This work seeks to define such a method and to analyze control techniques from the point of view of contribution to electrical power systems frequency stability.

# Contents

# List of Figures

# List of Tables

# List of Abbreviations

| | |
|---|---|
| ADC | Analog-to-Digital Converter, p. 16 |
| AESO | Alberta Electric System Operator, p. 4 |
| AGC | Automatic Generation Control, p. 4 |
| CCS | Code Composer Studio, p. 108 |
| DFIG | Doubly-Fed Induction Generator, p. 126 |
| DG | Distributed Generation, p. 3 |
| DR | Distributed Resource, p. 9 |
| EPLL | Enhanced Phase-Locked Loop, p. 14 |
| EPS | Electric Power System, p. 5 |
| ERCOT | Electric Reliability Council of Texas, p. 4 |
| ESS | Energy Storage System, p. 15 |
| FCWTG | Full Converter Wind Turbine Generators, p. 17 |
| GDP | Gross Domestic Product, p. 1 |
| GHE | Greenhouse Effect, p. 1 |
| GHG | Greenhouse Gas, p. 1 |
| HVDC | High-Voltage Direct Current, p. 18 |
| ICE | Individual Conditional Expectation, p. 54 |
| IPCC | Intergovernmental Panel on Climate Change, p. 1 |
| LFC | Load-Frequency Control, p. 6, 21 |
| MISO | Midcontinent System Operator, p. 4 |

| | |
|---|---|
| MPO | Manual for Operating Procedures, p. 8 |
| MPPT | Maximum Power Point Tracking, p. 3 |
| MPP | Maximum Power Point, p. 74 |
| NREL | National Renewable Energy Laboratory, p. 13 |
| ONS | Operador Nacional do Sistema Elétrico, Brazilian Power System Operator, p. 8 |
| PDP | Partial Dependence Plot, p. 54 |
| PI | Proportional-Integral, p. 5 |
| PLL | Phase-Locked Loop, p. 14, 108 |
| PRODIST | Procedimentos de Distribuição de Energia Elétrica no Sistema Elétrico Nacional, Procedures for Electric Energy Distribution in the National Electric System, p. 9 |
| PSCO | Xcel/Public Service of Colorado, p. 4 |
| PV | Photovoltaic generation unit, p. 8 |
| PWM | Pulse-Width Modulation, p. 18 |
| RES | Renewable Energy Sources, p. 2 |
| RMS | Root Mean Square, p. 29 |
| ROCOF | Rate Of Change Of Frequency, p. 3 |
| RSG | Rotational Synchronous Generators, p. 18 |
| SIN | Sistema Interligado Nacional, Brazilian Interconnected Power System, p. 8 |
| SPC | Synchronous Power Controller, p. 16 |
| SPWM | Sine Pulse-Width Modulation, p. 29 |
| SRF | Synchronous Reference Frame, p. 15 |
| SSG | Static Synchronous Generator, p. 15, 18 |
| SSM | Static Synchronous Machine, p. 36 |
| THD | Total Harmonic Distortion, p. 102 |

| | |
|---|---|
| TSO | Transmission System Operators, p. 20 |
| UCTE | Union for the Coordination of the Transmission of Electricity, p. 20 |
| UFLS | Under-Frequency Load Shedding, p. 8 |
| VISMA | Virtual Synchronous Machine, p. 15 |
| VSC | Voltage Source Converter, p. 4 |
| VSM | Virtual Synchronous Machine, p. 14 |
| WTG | Wind Turbine Generators, p. 3 |

# Chapter 1

# Introduction

After centuries of unrestrained growth, in the twentieth century, human civilization began discussing environmental and sustainability issues. The greenhouse effect (GHE) is the entrapment of heat in the Earth's atmosphere by so-called greenhouse gases (GHG). It keeps the Earth surface's temperatures at levels well suited for life forms to thrive. It was pointed out as early as 1896 [3] that GHE could be intensified by an increase in carbon dioxide concentration in the Earth's atmosphere. Throughout the twentieth century, research continued on the effects of human activities that increased the concentration of GHG in the Earth's atmosphere, such as fossil fuel burning, which became known as climate change or global warming [4–6]. The growing interest on the subject led to the establishment of the Intergovernmental Panel on Climate Change (IPCC) in 1988 to study the possible resulting climate changes and their socio-economic and environmental impacts. Growing evidence of this phenomenon and concerns about its consequences on the the Earth's climate drove efforts to more efficiently use our energy resources and explore alternative energy sources, such as wind and solar power [7].

The impacts of fossil fuel energy sources can be diminished through the reduction of the total amount of used energy. This path is often linked to the increase of energy use efficiency, leading to the proliferation of energy efficiency policies worldwide, present in at least 146 countries by the end of 2015 [8]. Increasing energy efficiency is, however, an indirect measure and higher efficiency might not result in lower total energy consumption [9]. Figure 1.1 shows a graph from [8] with world trends of primary energy intensity and total primary energy demand. Energy intensity is defined as the ratio between used energy and Gross Domestic Product (GDP). Hence, it is a way of quantifying energy efficiency with respect to economic output. Primary energy is the energy theoretically available in an energy source before accounting for losses in conversion, storage, transmission or whichever other processes are necessary before final use. The energy available after these processes is called final energy. Figure 1.1 then shows that, even though energy efficiency is rising (energy intensity

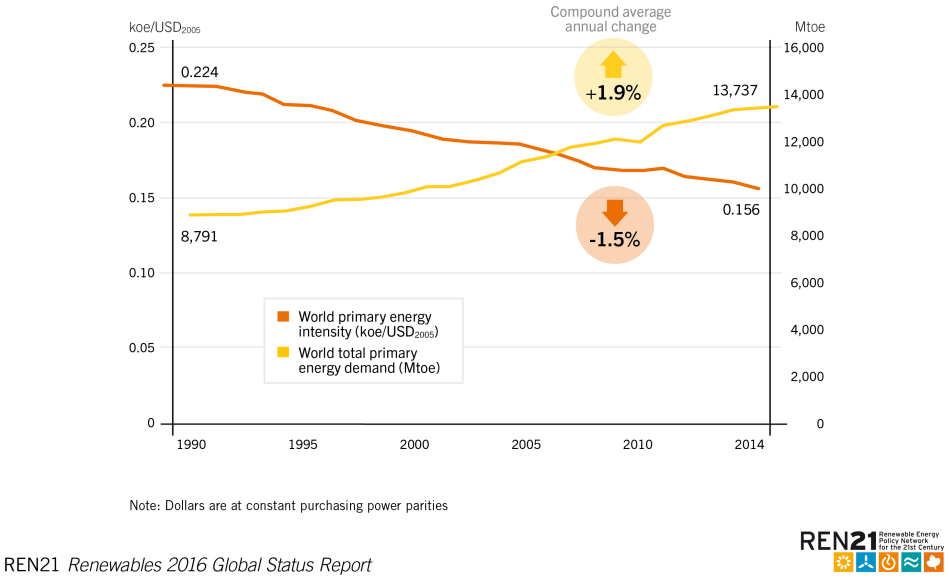


Figure 1.1: Global Primary Energy Intensity and Total Primary Energy Demand, 1990-2014. Dollars are at constant purchasing power parities. Original from REN21, 2016 Global Status Report Paris, REN21 Secretariat.

is falling), total energy consumption is rising.

Renewable Energy Sources (RES) are energy sources that are restored in a human timescale. RES have the benefit of being virtually infinite, while fossil fuels (e.g. coal, oil) are depleted at a faster rate than they are restored. They play an important role in shifting our energy economy towards a sustainable growth model. Additionally, RES are commonly identified as clean energy resources, meaning exploration of these resources does not emit GHG. This benefit has led to incentivising of RES exploration as part of the efforts to mitigate the effects of global warming. By the end of 2015, policy targets for RES shares had been set in at least 173 countries [8]. The European Union has set Renewable Energy Targets of 20% of their final energy use by the year of 2020 and 27% by the year of 2030, from the current number of 16% [8, 10]. Brazil has a RES share of 39,4% of its final energy use and aims for a 45% share by the year of 2030 [8]. There are also targets for the share of electricity generation from RES, with Brazil's being of 23% by the year of 2030 (excluding hydropower).

Power electronics technologies have been of great importance in making RES other than hydropower (alternative energy sources) viable for electric power generation. Most electric power generation solutions based on alternative energy sources

require power electronics devices. Wind Turbine Generators (WTG), for example, may be connected directly to the grid. However, this implicates fixed speed operation, which limits the efficiency of the unit. The most efficient configurations use back-to-back converters connected either to its stator or to its rotor windings [11]. PV and hydrogen fuel cells are DC sources and require inverters to connect to traditional AC grids and possibly also DC/DC converters to connect to a DC bus. Additionally, converters may be used to control the generating unit to keep it at the best possible operating point in terms of power extraction (Maximum Power Point Tracking, MPPT).

Distributed Generation (DG) is another trend that both feeds on and drives RES based generation growth. DG has been defined as an active power generation unit connected to the distribution network or on the customer side of the meter [12]. In practice, it means a larger, better distributed set of generating units. Industrial facilities, commercial centers and residences become potential sites for a DG plant. DG promises to lower dependence on new transmission lines, as it places generation units closer to consumers. Power supply reliability potentially increases as the number of components between generation and load decreases and the effects of loss of any single generating unit decreases. Even if a number of DG units of power equivalent to a traditional power plant is tripped, the effect on grid frequency is smaller than if the traditional power plant had been tripped [13]. DG projects are typically smaller in size and complexity, presenting lower financial risks than traditional power plants. Additionally, DG diversifies energy sources and increases competition in the energy market [14]. The Brazilian government launched, in December of 2015, a program to increase development of DG based on RES, ProGD. The program aims to introduce new regulations, more credit for DG projects, workforce training, incentives for DG equipment industry, fiscal incentives for the DG owner, lower importing taxes, among others.

## 1.1 Motivation

RES show a growing trend [10]. The increasing participation of RES based generation presents concerns to academia and to power system operators with respect to its impacts on power system stability. RES based generation's lack of physical rotating inertia is one source of concern. It is widely regarded that this fact is detrimental to the grid's frequency stability, subjecting grids to higher Rate Of Change Of Frequency (ROCOF) and larger transient frequency deviations due to disturbances [15–21]. The Nordic power system, comprised of the power systems in Finland, Norway, Sweden and eastern Denmark, has been experiencing frequency deviations of growing amplitudes [21]. This issue is thought to be caused by a

decreasing share of synchronous machine based generation and consequently a decreasing system inertia.

RES's varying power availability is another issue that contributes to stability concerns [22]. The usual principle for controlling RES generating units is MPPT, which forces them to inject as much power as possible for every operating condition. Combining MPPT with a varying power availability results in a varying power output, which can affect both frequency and voltage stability [23, 24].

There are two characteristics in the core of the concerns related to widespread use of RES for electrical power generation:

- RES power availability is difficult to predict and may change relatively quickly during operation;
- generating units deliver power through power electronics converters, instead of synchronous machines.

However, system operators have been updating their procedures with some success to cope with wind and PV generation variability. The Midcontinent Independent System Operator (MISO), which manages 14 GW of wind power, has been placing wind power plants on Automatic Generation Control (AGC) since 2011. Xcel/Public Service of Colorado (PSCO) has AGC capability on 2.2 GW of its wind power generation [25]. Wind and solar power can be curtailed and can, therefore, provide power reserves to respond to frequency changes at potentially faster rates than traditional synchronous generators. Other examples include the Electric Reliability Council of Texas (ERCOT) [26] and the Alberta Electric System Operator (AESO) [27], which require primary frequency control participation from WTG, and Hydro-Quebec, which requires inertia-mimicking controls [13].

It is argued that converters don't have a physical rotating inertia and, therefore, do not contribute to maintaining a steady grid frequency. Even though converters do not have a physical rotating inertia, they do have parameters that define characteristics in ways comparable to a synchronous machine's inertia. Indeed, converters can be controlled to behave as a synchronous machine within varying degrees of approximation. Interest in equipping converters with the capability of emulating synchronous generators' inertia has led to numerous papers on synchronous generator mimicking controllers [28–33].

One should note that converters do store energy (typically much less than synchronous generators). Voltage Source Converters (VSC) usually do so in capacitors with a regulated DC voltage, which could be used to define a converter's inertia constant $H_C$ equivalent to an electrical machine's inertia constant $H$. If $v_{dcbase}$ is the DC link's rated voltage, $P_{base}$ is the converter's rated power and $C$ is the DC

link capacitance, then equation (1.1) defines such an inertia constant.

$$H_C = \frac{1}{2}\frac{C v_{dcbase}^2}{P_{base}} \tag{1.1}$$

It cannot be said, however, that $H_C$ has the same meaning for converters as $H$ has for synchronous machines. That cannot be said even for the virtual inertia constant $H_V$ in synchronous generator mimicking controllers, if that converter must regulate its own DC link voltage. A VSC's DC link voltage is typically regulated through a Proportional-Integral (PI) controller. Such a controller will have a significant impact on the converter's power flow if it satisfactorily performs its job. Therefore, if one's concerned about a converter's active power response during frequency disturbances, the DC link dynamics must be considered.

Furthermore, a converter's capacity to respond to frequency deviations can be improved if its primary power source output is allowed to change. That would correspond to using a governor controller, similarly to synchronous generators, but with a faster response. In this way, the impact of the converter's small $H_C$ (little stored energy) is diminished. If the power source that feeds the converter can act sufficiently fast and it has enough power reserve, a generating unit may provide frequency support comparable to a synchronous machine's inertial response.

Hence, the inertia constant of a generating unit may not be a good metric to characterize its contribution to grid frequency stability. A good metric should incorporate the effects of other relevant parameters in the converter's control, such as its energy storage dynamics (e.g. the DC link voltage controller, batteries) and primary power source and its characteristics. In a global context of growing RES shares in Electric Power Systems (EPS), with target shares being set through intergovernmental agreements, being able to satisfactorily assess RES based generation contribution to grid frequency stability is a relevant matter.

## 1.2 Objective

This work's objective is to improve our capacity of evaluating the quality of grid frequency support a power electronics converter based generating unit can provide. This involves investigating how the concepts of inertia and primary frequency control can be extended to power electronics converters and their controllers and how those are affected by control parameters, primary power source and converter energy storage system.

Intended final products of this work are:

- at least one metric to evaluate quality of grid frequency support provided by a power electronics converter based generating unit;

- a methodology for a test to experimentally determine one of these metrics;
- estimation of metrics for two VSC controllers, considering a photovoltaic or wind power source through mathematical modeling and simulation;
- an analysis on the metrics' dependence on control parameters.

The developed metric can be used as a design criterion, a basis for comparison between generation solutions or as a requirement set by grid codes, standards and policies.

## 1.3 Methodology

In order to seek the stated objective, I will survey the literature on the topics of impacts of RES on grid frequency stability and grid supporting VSC control strategies. Studying the impacts of RES on grid frequency stability will help determine relevant aspects of the problem in order to fashion a metric which will better capture the desired information. Knowledge of grid supporting VSC control strategies will be used to estimate how different control strategies fare under proposed metrics and to study the relationships between their parameters and said metrics.

Primary power source considerations will focus on wind and solar photovoltaic generation. However, whenever possible, characterization of the power source will be generic, such as stating maximum power slew rate or typical rising time.

I will use simulations to test different systems' responses to frequency disturbances and load-generation unbalances. These responses will be necessary for evaluating new frequency support metrics. Simulations will include system equivalent models used in Load-Frequency Control (LFC) studies coupled with individual VSC controller models in small and large signal forms.

Lastly, I will use an experimental setup to test one of the metrics and propose an experimental methodology to evaluate it. The laboratory is equipped with RES emulating converters, which is sufficient for the intended objectives.

# Chapter 2

# Problem definition and existing research

## 2.1 Electric power system frequency stability fundamentals

EPS are complex, nonlinear dynamic systems of great dimensions. Although its stability is a characteristic of the whole system, it is helpful to classify events that take them away from stable, viable operating conditions as different kinds of stability issues. One way of classifying stability issues is suggested by KUNDUR *et al.* [34] and shown in figure 2.1. The first level of classification, as rotor angle stability, frequency stability and voltage stability, considers the main system variable through which instability is observed. Further subdivisions may be made with respect to time scales of most relevant processes, analysis techniques and disturbance intensity.

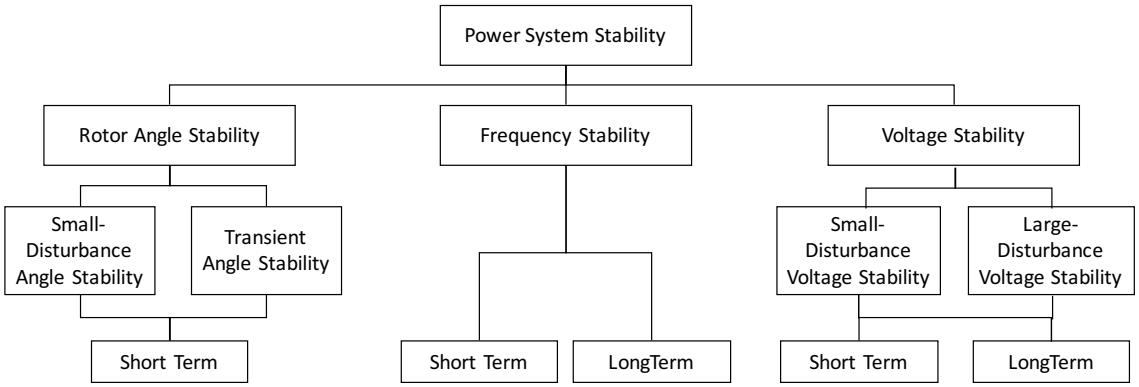


Figure 2.1: Classification of power system stability issues.

Frequency stability issues may be sustained frequency oscillation, or a frequency deviation with too high an amplitude or rate of change, leading to tripping of system elements. They are basically caused by an inability to recover, without loss of load,

from a condition of load-generation unbalance after a disturbance. Examples of such disturbances include tripping of loads or generating units, short circuits, loss of transmission lines and system islanding. This class of system stability is specially relevant in smaller EPS, such as isolated systems, microgrids and islanded systems that broke off from the main EPS due to a protection relay tripping.

Frequency stability can be subdivided in short and long term stability. Relevant processes for short term frequency stability include frequency based protections, either on loads or generators, such as trend relays and Under-Frequency Load Shedding (UFLS), electrical machines inertial responses, primary frequency controls and load-frequency response. These effects range from tens of milliseconds to seconds. Long term aspects of frequency stability may involve processes such as primary and secondary frequency control and protections and controls of boilers or reactors. These effects range from tens of seconds to minutes.

### 2.1.1 Grid codes and standards

Brazil's National Operator of the Electric System (Operador Nacional do Sistema Elétrico, ONS) coordinates and controls operations of generation and transmission facilities in Brazil's National Interconnected System (Sistema Interligado Nacional, SIN). ONS's Manual for Operating Procedures (MPO, Module 10 in ONS's Grid Procedures, Procedimentos de Rede) states that manual load shedding is necessary in cases of sustained under-frequency of 59.5 Hz or less [35]. In that case, load will be manually shed until the grid frequency stabilizes at least at 59.7 Hz and no load will be reconnected until the grid frequency is back at 60 Hz. ONS also defines minimum requirements for generating units' operation outside rated grid frequency [36], when connected to the transmission grid, or to distribution grid at voltage levels of 69 kV or higher, as per figure 2.2. For thermal power plants, if frequency goes outside the 57-63 Hz range, the unit is allowed to trip instantaneously. It is not allowed to trip at all if frequency is in the 58.5-61.5 Hz frequency range. It must be able to maintain operation below 57.5 Hz for at least 5 seconds and below 58.5 Hz for 10 seconds. The same graph presents similar requirements for hydro, wind and Photovoltaic (PV) power stations.

ONS defines a UFLS system, called ERAC (*Esquemas Regionais de Alívio de Carga por Subfrequência*, Portuguese for Regional Under Frequency Load Relief Schemes), which establishes frequency and ROCOF values that trigger automatic load shedding [37]. The Brazilian SIN is divided in regions, each one with different ERAC settings. Load shedding is divided in up to five levels, each one set to a different frequency, possibly a ROCOF value and possibly with a timer. Frequency trigger values range from 58.5 to 57 Hz, while ROCOF trigger values range from 0.5

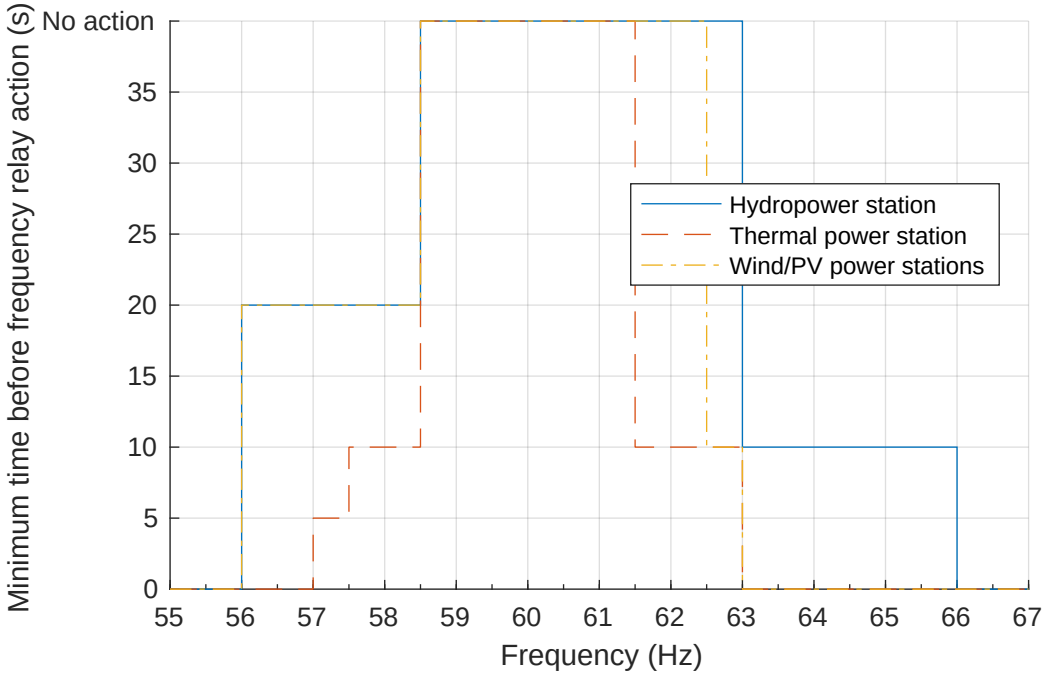


Figure 2.2: Minimum time ONS requires power stations to remain connected, for different grid frequencies, before any frequency protection scheme takes action.

to 10 Hz/s. Each protection level, when triggered, automatically sheds a fraction of region load between 6 and 16%.

Brazilian code for the distribution network (Procedimentos de Distribuição de Energia Elétrica no Sistema Elétrico Nacional, PRODIST) requires DG to employ under, over frequency and anti-islanding protection. It is further required that DG guarantees that, if a disturbance originated in the distribution system drives frequency outside the range between 59.5 and 60.5 Hz, frequency is restored to values within said range up to 30 seconds after leaving it [1]. In extreme conditions, when load shedding is necessary, frequency must still obey ranges specified by table 2.1.

Table 2.1: Allowed frequency ranges for extreme disturbances, when load shedding is necessary, as defined by PRODIST [1].

| Frequency (Hz) | Time Allowed Within Frequency Range (s) |
|---|---|
| $62.0 < f < 63.5$ | 30 |
| $57.5 < f < 58.5$ or $63.5 < f < 66.0$ | 10 |
| $56.5 < f < 57.5$ | 5 |
| $f < 56.5$ or $f > 66.0$ | not allowed |

IEEE's Standard for Interconnecting Distributed Resources with Electric Power Systems [2] defines frequency values above and below which a Distributed Resource (DR, a superset of DG that includes energy storage systems) must cease to energize the Area EPS within specified clearing times. These frequency values are defined

according to DR power levels, as per table 2.2. The stated reasons for this relaying include island detection and prevention of over or under frequency damage to other equipment [38].

Table 2.2: Frequency ranges for which DR must cease to energize Area EPS, according to [2].

| DR Power (kW) | Frequency (Hz) | Clearing Time (s) |
|---|---|---|
| $P \leq 30$ | $f > 60.5$ | up to 0.16 |
| | $f < 59.3$ | up to 0.16 |
| $P > 30$ | $f > 60.5$ | 0.16 |
| | $f < \{59.8 - 57.0\}$ (adjustable) | 0.16-300 (adjustable) |
| | $f < 57.0$ | 0.16 |

### 2.1.2 A load-generation disturbance

Figure 2.3 exemplifies the behavior of the frequency of an EPS equipped with primary frequency control after a sudden generation-load unbalance, such as the loss of a big generation unit. The illustrated case models a hydroelectric power plant's generator, turbine and governor and EPS load after a generation-load unbalance equivalent to 19.7% of the system's total generation capacity. Three relevant metrics for this type of event are highlighted.

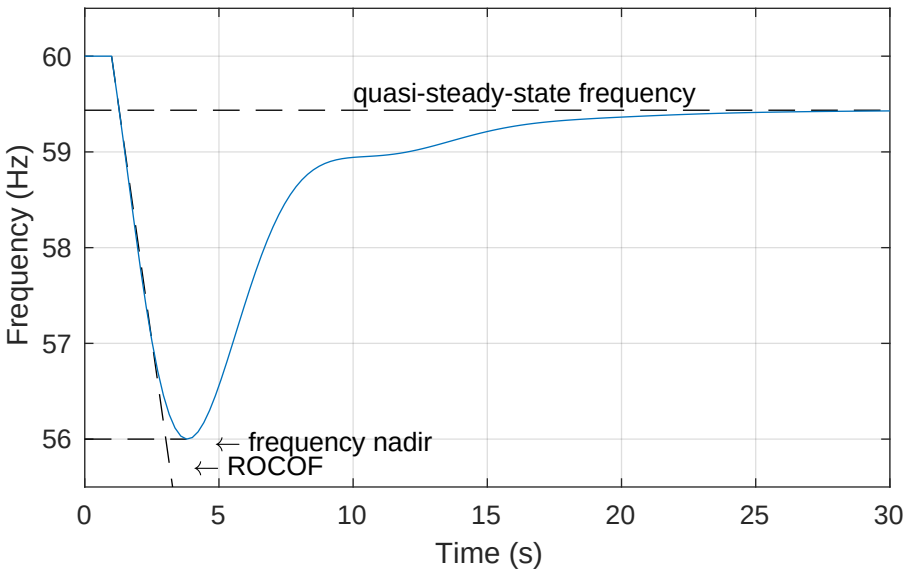


Figure 2.3: Typical frequency response to a step load increase or loss in generation capacity.

### Frequency nadir

After a disturbance that generates a mismatch between load and generation powers, system frequency will deviate from its nominal value. In the case that a disturbance causes a generation deficit, where load consumes more power than is being generated, system frequency will drop. The frequency nadir is the lowest frequency reached after a generation deficit disturbance (frequency zenith is the maximum frequency in the case of a generation surplus disturbance). Its importance comes from the fact that there are relays in EPS that act when frequency reaches a certain value below the rated frequency, such as:

- UFLS, to help stabilize frequency;
- generating units and loads protections, for safety and equipment integrity reasons;
- island detection schemes.

Frequency nadir determining factors include disturbance amplitude and dynamics, inertia of generators, motors and synchronous compensators connected to the system, primary control reserves, number of assigned units and dynamics and load-frequency response (how power consumed by the load changes with frequency deviations) [39].

The Nordic power system, which has a maximum load around 70 GW, has been reporting decreasing frequency nadirs [21]. The lowest value reported for N-1 contingencies was close to 49.35 Hz (for a rated frequency of 50 Hz).

In a scenario with increasing levels of RES based DG, if these fail to provide adequate frequency support, frequency deviations will grow in intensity and become more frequent. This means a higher probability of load shedding schemes coming into action. Furthermore, the share of generation under protections such as the ones shown in table 2.2 will also increase, therefore the amount of generation capacity lost due to a large frequency deviation will increase, potentially leading to greater cascade effects.

### Quasi-steady-state frequency

Quasi-steady-state frequency is the frequency reached after action of the primary frequency control stabilizes system frequency, but before secondary frequency control has taken noticeable action. It is a deviation from the nominal frequency, as primary frequency control employs a proportional controller, known as droop control, which does not guarantee zero steady state error. Droop control, on its own, implements a relationship between a generating unit's active power output and frequency $\Delta\bar{\omega} =$

$-R\Delta\bar{P}$, which enables stable operation of multiple generating units and equitable load sharing between them. The parameter $R$ is the droop setting, typically 5% considering a per unit system [40], meaning a 5% drop in frequency will cause a 1 p.u. increase in power output.

Primary control reestablishes balance between load and generation. Secondary control, on the other hand, is slower and implements integral action and is used to drive system frequency back to its nominal value. It may also be used to keep tie line power flow at the desired levels.

Quasi-steady-state frequency is a function of disturbance amplitude, primary control regulation and load frequency response. The combined effect of primary control regulation of all units participating in primary control and the load frequency response is called composite frequency response characteristic, or network power frequency characteristic.

#### Rate of change of frequency

The ROCOF is simply the rate of change of frequency, highlighted in figure 2.3 at its maximum value, at the initial moments after the disturbance. It is another variable on which some protection relays act, specially anti-islanding protection for DG. DG is required to disconnect from the Area EPS in case islanding occurs [2] and ROCOF has been a variable commonly chosen to infer islanding. However, if a disturbance causes high ROCOF, anti-islanding schemes may incorrectly interrupt DG units operation, further aggravating power unbalance [21]. ROCOF relay threshold values may range from 0.4 Hz/s to 10.0 Hz/s.

## 2.2 RES's impact on grid frequency stability

ULBIG *et al.* [15] have argued that increased RES penetration will lower grid inertia and increase its time variability. They used simulations of one and two-area system models to show that lower aggregated inertia causes higher frequency and tie-line power transfer overshoots during faults. The authors calculated the aggregated inertia constant for operation of the German power system during the period of December of 2012 to show that these problems may already be a reality in some power systems. Their estimations showed an aggregated inertia constant varying between 3 and 6 s. For this, they assumed a constant inertia value for conventional generators and that RES generators did not provide any inertia. ULBIG *et al.* [16] continued their work comparing meshed and non-meshed grids, showing the importance of topology to grid frequency behavior. They concluded that better meshed grids are less susceptible to frequency and tie-line power oscillations.

TIELENS and HERTEM [19] discussed important aspects of the role of inertia in power systems. They argue that RES currently do not contribute to grid inertia due to electrical decoupling between generator and grid and to the absence of an energy buffer (e.g. machine rotor's kinetic energy) in some of these sources. With growing participation of RES, power system inertia would decrease, which could lead to problems related to rotor angle stability and frequency stability. The rotor angle stability problem can be exemplified by the fact that lower inertia results in lower damping and higher oscillating frequency for a synchronous machine connected to an infinite bus. The authors admit, however, that there is no consensus in the literature about the effects of lower inertia on rotor angle stability. The frequency stability concerns come from the decrease of grid frequency robustness for lower system inertia values. A power balance disturbance in a system with lower inertia causes a larger grid frequency deviation with higher ROCOF. The authors point out that these effects can trigger frequency-based protections, which in turn would generate more power balance disturbances in a cascade effect. There is also concern about the effects high ROCOF might have on synchronous generators, possibly catastrophic failure or lifetime reduction.

BOEMER *et al.* [41] have reported that the forecast for the All-Island Irish power system (Northern Ireland and Republic of Ireland) has a stable operation limit between 60% and 80% of share of power sources that do not provide inertia. Their model for frequency stability studies considers a single busbar, consequently it has all rotating masses in perfect synchronism. This model includes dynamics of turbines, governors, boilers and load and analyses maximum ROCOF and frequency excursion after a disturbance in generation capacity or load to determine critical scenarios.

The National Renewable Energy Laboratory (NREL) have conducted a study to investigate the impacts of high wind and solar penetrations on the Western Electric Power System of the United States. Part of the research considers the effects on frequency response after a large load-generation unbalance, with promising results [13]. Additional WTG controls considered include governor and inertial controls [42], as well as each of these separately. When both controls were used together, simulations resulted in an improvement in frequency nadir of 0.15 mHz per MW of wind power primary frequency control reserve. The report concludes that RES based generation can provide an effective, positive contribution to frequency nadir and quasi-steady-state frequency through employment of frequency-responsive controls.

## 2.3 Grid supporting control strategies

The prospects of increasing participation of RES, DG and power electronics-interfaced generation in general in power systems has led to studies about how these power electronics converters are controlled. A shift will be required from grid feeding strategies, which are irresponsive to grid voltage and frequency and typically associated with current control, to grid supporting strategies (also called grid forming), which contribute to grid frequency and voltage regulation and are typically associated with voltage control [43]. Part of these studies focuses on integrating synchronous generators' characteristics and/or their control strategies into converters. This would enable taking advantage of existing knowledge on synchronous generators and power systems control and avoiding the cited stability issues even as RES and DG participations increase.

D'ARCO and SUUL [33, 44] have made a literature survey on Virtual Synchronous Machines (VSM) and demonstrated an equivalence with microgrid droop controllers. They have shown that control as a synchronous machine has been pursued with varying degrees of detail, from 7th order models [28] down to 1st order models [29] and microgrid droop controllers [45]. The equivalence between microgrid droop controllers and VSM is deduced for small signals with the assumption that active and reactive powers used in the droop controllers are filtered with a low-pass first order filter. If the filter's transfer function is

$$G(s) = \frac{\omega_f}{s + \omega_f}, \tag{2.1}$$

the microgrid droop gain is $m_p$ and the VSM has inertia constant $H$ and damping constant $k_d$, then these controllers will be equivalent if

$$H = \frac{1}{\omega_f m_p} \tag{2.2}$$

and

$$k_d = \frac{1}{m_p}. \tag{2.3}$$

ZHONG and BOROYEVICH [46] have compared the structures of an Enhanced Phase-Locked Loop (EPLL), one of the Phase-Locked Loop (PLL) topologies, and a microgrid droop controller. They show there is a close relationship between those two control structures, although they're not identical. The microgrid droop controller is in fact a PLL, but one with parameters defined by the physical parameters of the converter's coupling impedance.

SAO and LEHN [47] study and propose a more flexible droop control technique for VSC which requires a remote bus voltage measurement. The new scheme allows

for changing the poles of the closed-loop active and reactive power systems without changing steady-state power output. Additionally, it decouples steady-state reactive output from grid parameters.

Useful research for this topic also comes from research on parallel connection of UPS systems and control strategies for microgrid converters [45, 48–50]. These incorporate variations on droop controllers between active power and frequency and between reactive power and voltage amplitude and virtual impedance emulation through control to improve power sharing between generating units and dynamic performance.

BECK and HESSE [28] have suggested the development of a Virtual Synchronous Machine (VISMA), an inverter controlled in such a way that mimics the synchronous generator behavior. The simulated machine model included Synchronous Reference Frame (SRF) impedances of stator, damper and exciter windings and their coupling impedances. The machine model is solved for current at each sampling period and the machine current is used as a reference for the converter's current control. VISMA uses a more sophisticated synchronous machine model than other control strategies that mimic synchronous machines. It is more complex and requires more computational power. The requirements for simulating a high inertia machine on the DC link voltage and the energy source that regulates it are not considered.

DRIESEN and VISSCHER [29] also suggest the shift from grid feeding control strategies to grid supporting control strategies through synchronous generator mimicking. They emphasize the need for emulating the inertia of synchronous generators, although they suggest doing so through addition of an Energy Storage System (ESS), instead of through control strategies only.

ZHONG and WEISS [30] introduced a VSC control topology which was at first published as Static Synchronous Generator (SSG), but later named synchronverter [31], as SSG had already been defined by [51]. The basic idea behind it was to use a synchronous generator model to guide the operation of an inverter. A synchronverter emulates a cylindrical rotor synchronous machine through its rotational motion differential equation, its power flows calculations, and its internal voltage calculation. It also includes active power-frequency and reactive power-voltage amplitude droop controllers. The synchronverter model is developed considering a cylindrical rotor synchronous machine with no damping circuits. Additionally, the effect that the derivative of the field winding current $i_f$ has on the machine's internal voltage is neglected. The synchronverter can be represented in a per unit system by the diagram in figure 2.4, where

- $H_V$ is the emulated machine's virtual inertia constant;
- $R_p$ is the emulated machine's droop setting;

- $\bar{\omega}$ is the emulated machine's rotor speed;
- $\theta$ is the emulated machine's rotor position;
- $\omega_b$ is the base angular frequency;
- $M_f$ is the maximum mutual inductance between field winding and any of the stator phase windings;
- $i_f$ is the current circulating in the virtual field winding.
- $\bar{P}_{set}$ is the set point for output power;
- $\bar{T}_m$ is the emulated mechanical torque;
- $\bar{T}_e$ is the calculated electromagnetic torque;
- $\bar{T}_d$ is the damping torque, due to frequency deviation.

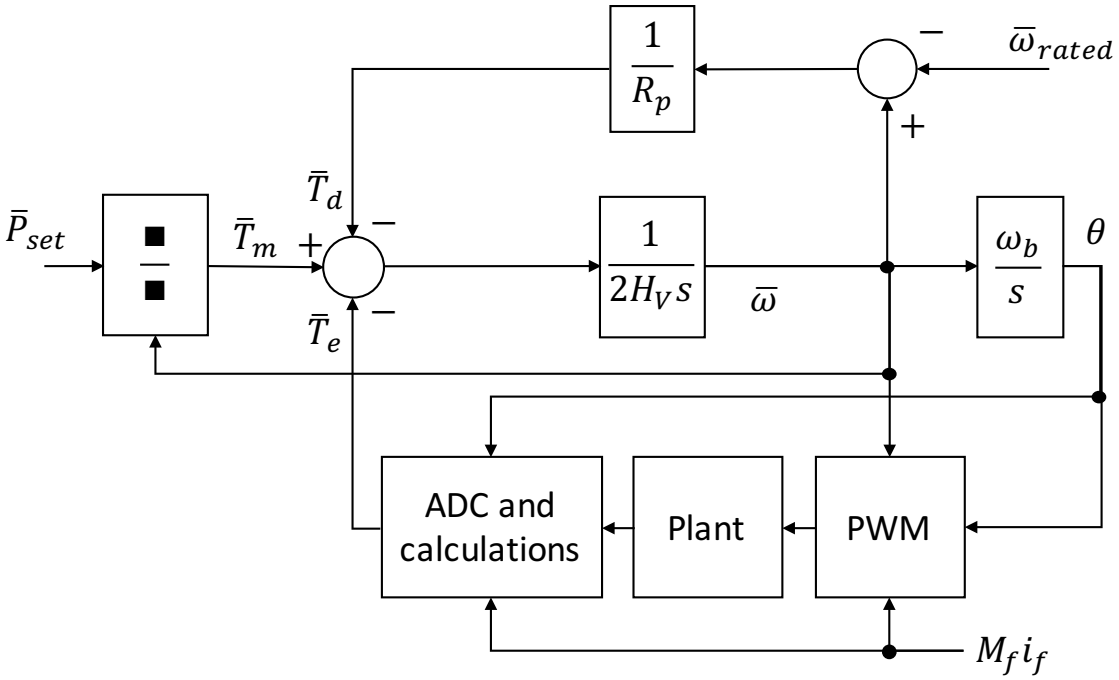


Figure 2.4: Synchronverter controller diagram.

RODRIGUEZ *et al.* [43, 52] have suggested a control strategy for voltage source converters that mimics synchronous generators, but avoids some of its disadvantages. This control strategy is called Synchronous Power Controller (SPC). The generated voltage frequency comes from a transfer function from power tracking error. Damping ratio and frequency bandwidth parameters of this transfer function can be adjusted to obtain the desired behavior, instead of being characteristics set by a machine's physical properties. The generated voltage amplitude can be

controlled, for example, through a PI controller to track a desired reactive injection level. They propose a method for virtual impedance emulation that does not require digital implementation of derivatives. The resulting impedance of the converter and its filter is given by the virtual impedance chosen in the controller.

REMON *et al.* [53] have continued the work on [43, 52] by suggesting an interesting approach to deal both with DC link regulation and frequency measurement simultaneously. They equate the kinetic energy in a synchronous machine's rotor and the electrostatic energy in the DC link capacitor, noting that the angular frequency of the internal voltage can be taken from the DC link voltage through a static gain.

$$E = \frac{1}{2}J\omega^2 = \frac{1}{2}Cv_{dc}^2 \tag{2.4}$$

$$\omega = v_{dc}\sqrt{\frac{C}{J}} \tag{2.5}$$

They observe that the resulting active power loop would have no damping and therefore suggest a proportional derivative transfer function from DC link voltage to internal voltage angular frequency, instead of using equation 2.5. Furthermore, they propose using a storage system coupled to a DC/DC converter to control the DC link voltage in such a way that they can emulate different capacitance values.

REMON *et al.* [54] showed the behavior of the SPC when injecting power from a Photovoltaic generation unit (PV) into a small power system supplied also by a diesel generator unit. Simulations are used to compare scenarios where the PV is operated at the MPPT with scenarios where SPC is used. The SPC was shown to have a substantially positive impact on grid frequency and voltage behaviors during power imbalances. It assumes, however, that an ESS is available and does not model its dynamics or DC link voltage regulation.

CONROY and WATSON [55] have investigated how Full Converter Wind Turbine Generators (FCWTG) can provide frequency support. Regarding the power reference given to the converter connected to the generator, they proposed a part of such reference that is activated only when abnormal frequency conditions are detected. This part is composed of a droop component, which is proportional to frequency deviation, and an allegedly inertial response component that is proportional to ROCOF. This way, they intend to incorporate into WTG the desired aspects of synchronous generators to mitigate frequency-related problems caused by an increased wind power penetration ratio.

ZHANG *et al.* [56] have proposed to simplify the control naturally found on synchronous machines by removing one of its integrators. That is, there are two integrators from net torque to rotor angular position in a synchronous machine

rotor's rotational motion mathematical model.

$$T_m(t) - T_e(t) - T_d(t) = T_{net}(t) = J\frac{d\omega(t)}{dt} = J\frac{d^2\theta(t)}{dt^2} \tag{2.6}$$

The small-signal open loop transfer function from net power to load angle of such a model is given by equation (2.7).

$$\frac{\Delta\delta(s)}{\Delta P_{net}(s)} = \frac{K}{s^2} \tag{2.7}$$

The authors proposed a transfer function of one integrator from power error to rotor angular position (or output voltage phase) in order to increase phase margin, as shown in equation (2.8).

$$\frac{\Delta\delta(s)}{\Delta P_{net}(s)} = \frac{K}{s} \tag{2.8}$$

This was proposed for VSC-HVDC (High-Voltage Direct Current) transmission applications, but may be applied to VSC in general.

XIONG *et al.* [57] have performed an interesting analysis on Static Synchronous Generators (SSG), which they defined simply as a grid-tied Pulse-Width Modulation (PWM) inverter. They drew comparisons between SSG and Rotational Synchronous Generators (RSG) on generation system structure, power flow relationships, physical parameters, dynamic models and small-signal and transient stability. The considered SSG uses the typical current control based on a DC link voltage outer loop with a SRF inner current loop, both with PI controllers. The authors showed, through small-signal analysis, that a SSG controlled this way has a RSG equivalent model. They also stablished the relationships between the DC link voltage PI controller's proportional and integral gains and the RSG's damping and synchronizing torque parameters. The inertia constant $H_C$ of the equivalent RSG is given by the energy stored in the converter's DC link capacitor bank, as shown in equation (2.9).

$$H_C = \frac{1}{2}\frac{Cv_{dcbase}^2}{P_{base}} \tag{2.9}$$

## 2.4 An inverter's inertia

With the prospects of growing RES based generation and DG, concerns over grid frequency stability are also growing. There is great interest in the literature in control strategies that mimic synchronous generators with the purpose of providing inertia to the system and stabilizing grid frequency.

Frequency inertia is related to the dynamics of the state variable that represents the generated voltage's frequency. In a rotating electrical machine, it is highly

correlated with the rotating mass' moment of inertia. This rotating mass is composed of the machine's rotor and the turbine that moves it. A converter's control and physical parameters have similar influence in the voltage frequency's dynamics. Control strategies designed to operate with MPPT or constant power (active or reactive) injection are specifically designed to very quickly detect and adapt to grid voltage changes. This is done through fast PLLs, specifically so that even if frequency changes or voltage amplitude changes, injected power does not change.

The amount of kinetic energy stored in an electrical machine's rotor is directly related to its frequency inertia. That is, however, not the case with converters. A voltage source converter can operate for a certain DC link voltage range. The inertia in the sense of amount of energy stored for a given rated voltage level determines the disturbance magnitude required to take the converter out of its stable operation region. So, a big capacitance leads to a sturdy converter, i.e. it has a large amount of stored energy and, more importantly, it requires a large amount of energy flow to take it out of required operating conditions.

These two concepts, frequency inertia and stored energy, are tightly bound in electric machines, but they're not explicitly tightly bound in power electronics converters. The stored energy in a converter is still coupled with its output voltage frequency (if it regulates its own DC link voltage), as a decrease in DC link voltage will cause the converter to transiently change its output voltage amplitude and frequency in order to change active power flow and restore rated DC link voltage. If the front end converter must emulate a synchronous generator, increasing injected power following a frequency drop, then a fast-acting back end converter would help in constituting a sturdy converter, as it would be able to quickly react to changes in stored energy. Therefore, a comprehensive analysis of a converter's capabilities of providing inertia to the grid must take into account the prime mover's dynamics as well, and not only its own inertia.

A larger frequency inertia can be emulated as long as we can keep the DC link voltage within operational levels, to which the following characteristics contribute:

- the back end converter can quickly respond to the DC link voltage variations (implies dynamic requirements and the capacity of maintaining a power reserve);
- high DC link voltage inertia, i.e. amount of stored energy (either higher DC link capacitance and voltage or presence of another ESS)
- wide operational range for DC link voltage.

## 2.5 A grid frequency support metric

Inertia constants have been taken as an indicator of contribution to grid frequency stability as individual units' inertia constants compose the aggregated inertia constant used in a Load-Frequency Control (LFC) model. When neglecting primary frequency control, a system with aggregated inertia constant $H_{sys}$ and load damping constant $D$ changes frequency due to generation-load unbalance with a time constant given by $\tau = 2H_{sys}/D$.

However, one should not compare power electronics based generation's capacity to offer grid frequency support with synchronous machine based generation's considering only their inertia constants. RES and DG have the potential to provide faster primary frequency control, possibly comparable to a synchronous generator's inertial response. The Union for the Coordination of the Transmission of Electricity (UCTE), an association of Transmission System Operators (TSO) for the European interconnected EPS, allows for a maximum deployment time for primary control reserves between 15 and 30 s, depending on the size of the power reserve [39].

On the other hand, for wind power, the back end converter, which controls electric torque on the generator, may transiently increase extracted power from the turbine, slowing it down, to provide fast response to frequency deviations [13]. This strategy has been called inertial control, being compared with the inertial response provided naturally by synchronous generators, and does not employ a mechanical governor system. The response time provided through this mechanism is therefore faster, depending on electromagnetic dynamics. Wind can also be curtailed, constituting a power reserve, and operated with the typical primary frequency control strategy. The speed of response, in this case, is comparable to hydroelectric machines and mechanical stress limitations may apply. For PV units, there is no rotational inertia and inertial control is therefore not possible. Curtailment, however, is possible and its use for primary frequency control can also achieve faster response times [13].

In the current scenario, it would be beneficial to be able to measure the quality of grid frequency support provided by a generating unit. For new generation technologies, the inertia constant does not seem to be a clear indication of such a characteristic. Being able to quantify the quality of grid frequency support provided by a generating unit allows for grid codes and utilities to demand good frequency response from RES and DG projects, for clients to compare converters and power generation solutions and for comparison of converter control strategies.

# Chapter 3

# Model development

## 3.1 Load-Frequency Control model

The frequency stability issue is dealt with through Load-Frequency Control (LFC). LFC's objective is to regulate system frequency and tie-line power flows despite disturbances caused by unbalances between generated and consumed power. The model for LFC studies developed in [58] will be used to assess time responses by generation units connected to an EPS. Classical hydroelectric plant governor and turbine models from the same reference are employed.

The feature to be studied more closely is the frequency nadir. Primary frequency control is more critical to frequency nadir, as it is the fastest control to act on mechanical power input. It reestablishes power balance, stopping frequency deviation, but it allows a steady-state frequency error. Secondary frequency control, responsible for reestablishing reference values for system frequency and tie-line power flows, has a slower response, with little influence on these variables, and will not be modelled.

### 3.1.1 Hydraulic turbine and governor LFC model

A generator with a mismatch between delivered mechanical torque $T_m(t)$ and exerted electrical torque $T_e(t)$, whose rotor has an inertia $J$ and spins at a mechanical angular speed $\omega_r(t)$, experiences a rotor acceleration described by equation (3.1).

$$T_m(t) - T_e(t) = J\frac{d\omega_r(t)}{dt} \tag{3.1}$$

If it is desired to work in a per unit system, one may define the inertia constant $H = E/P_{base} = 0.5J\omega_{base}^2/P_{base}$, where $P_{base}$ is a base power and $\omega_{base}$ is a base mechanical angular speed, typically taken as the machine's rated values, and rewrite equation (3.1) as equation (3.2), where overbars denote a variable in the per unit

system. The index $r$ for angular speed is dropped, as mechanical and electrical angular speeds are equal in a per unit system.

$$\bar{T}_m(t) - \bar{T}_e(t) = 2H\frac{d\bar{\omega}(t)}{dt} \tag{3.2}$$

Expressing equation (3.2) in terms of small deviations around a stable equilibrium at $t = 0$ given by set of equations (3.3), where $\bar{T}_m(0) = \bar{T}_e(0)$ and $\bar{\omega}(0) = \bar{\omega}_{base} = 1$, gives equation (3.4).

$$\begin{aligned} \Delta\bar{T}_m(t) &= \bar{T}_m(t) - \bar{T}_m(0) \\ \Delta\bar{T}_e(t) &= \bar{T}_e(t) - \bar{T}_e(0) \\ \Delta\bar{\omega}(t) &= \bar{\omega}(t) - \bar{\omega}(0) \end{aligned} \tag{3.3}$$

$$\Delta\bar{T}_m(t) - \Delta\bar{T}_e(t) = 2H\frac{d\Delta\bar{\omega}(t)}{dt} \tag{3.4}$$

The per unit power being delivered associated with a torque is given by equation (3.5) and can be likewise expanded in terms of small deviations, which gives equation (3.6).

$$\bar{p}(t) = \bar{\omega}(t)\bar{T}(t) \tag{3.5}$$

$$\Delta\bar{p}(t) + \bar{p}(0) = \left[\Delta\bar{\omega}(t) + \bar{\omega}(0)\right]\left[\Delta\bar{T}(t) + \bar{T}(0)\right] \tag{3.6}$$

Terms composed only of initial values cancel out. Neglecting second order deviation terms gives equation (3.7).

$$\Delta\bar{p}(t) = \bar{T}(0)\Delta\bar{\omega}(t) + \bar{\omega}(0)\Delta\bar{T}(t) \tag{3.7}$$

Calculating the power deficit (subtracting electrical power from mechanical power) and applying equation (3.7) results in equation (3.8).

$$\Delta\bar{p}_m(t) - \Delta\bar{p}_e(t) = \left[\bar{T}_m(0) - \bar{T}_e(0)\right]\Delta\bar{\omega}(t) + \bar{\omega}(0)\left[\Delta\bar{T}_m(t) - \Delta\bar{T}_e(t)\right] \tag{3.8}$$

Starting from equilibrium, at rated speed, $\bar{T}_m(0) = \bar{T}_e(0)$ and $\bar{\omega}(0) = 1$, which results in equation (3.9).

$$\Delta\bar{p}_m(t) - \Delta\bar{p}_e(t) = \Delta\bar{T}_m(t) - \Delta\bar{T}_e(t) \tag{3.9}$$

Therefore, equation (3.4) can be rewritten with respect to powers instead of torques, as in (3.10).

$$\Delta\bar{p}_m(t) - \Delta\bar{p}_e(t) = 2H\frac{d\Delta\bar{\omega}(t)}{dt} \tag{3.10}$$

The electric power can be expressed in two separate terms to account for load variation with frequency. Equation (3.11) does so, with $D$ being the load's damping constant. A typical value considered for D is 1 [39, 58], meaning a frequency deviation will cause an equal load variation in a per unit system.

$$\Delta\bar{p}_e(t) = \Delta\bar{p}_L(t) + D\Delta\bar{\omega}(t) \tag{3.11}$$

Substituting in equation (3.10) gives

$$\Delta\bar{p}_m(t) - \Delta\bar{p}_L(t) - D\Delta\bar{\omega}(t) = 2H\frac{d\Delta\bar{\omega}(t)}{dt} \tag{3.12}$$

Primary frequency control drives change in gate position $\Delta y(t)$ to change input mechanical power through a speed governor. It may be implemented with mechanical-hydraulic or electrohydraulic systems, analog or digital. For hydraulic plants, a transient droop $R_T$ is used to increase stability margins, needed to enable the typical permanent droop of $R_P = 5\%$. The reset time constant for the transient droop is $T_R$. A simplified representation of the hydraulic turbine governor [58], considering a governor actuator characterized by a time constant $T_G$, is given by the transfer function from frequency deviation to change in gate position in equation (3.13).

$$\frac{\Delta\bar{Y}(s)}{\Delta\bar{\Omega}(s)} = -\frac{1}{R_P}\left(\frac{1}{1+sT_G}\right)\left(\frac{1+sT_R}{1+s(R_T/R_P)T_R}\right) \tag{3.13}$$

ONS requires that generating units rated above 30 MW must have $R_P$ adjustable between 0.02 and 0.08, while $R_T$ must be adjustable between 0.1 and 5.0 [36]. It further sets a standard value $R_P = 0.05$, unless studies indicate such value to be inadequate [40].

Finally, the classical, lossless transfer function for the hydraulic turbine relates gate position change and output mechanical power, as given by equation (3.14). The parameter $T_W$ varies with turbine loading, typically ranging from 0.5 to 4 s at full load, and is called water starting time.

$$\frac{\Delta\bar{P}_m(s)}{\Delta\bar{Y}(s)} = \frac{1-sT_W}{1+\frac{1}{2}sT_W} \tag{3.14}$$

Equations (3.13) and (3.14) assume a per unit system with bases given by variables' steady-state, pre-disturbance values.

The model is graphically summarized by the block diagram in figure 3.1. It can be regarded as a single area model of an EPS, neglecting speed deviations between generators within this area. That is, it represents the power balance within an

isolated control area (no tie line power flow to other control areas) of an EPS and a collective rotor speed among the generators in that control area.

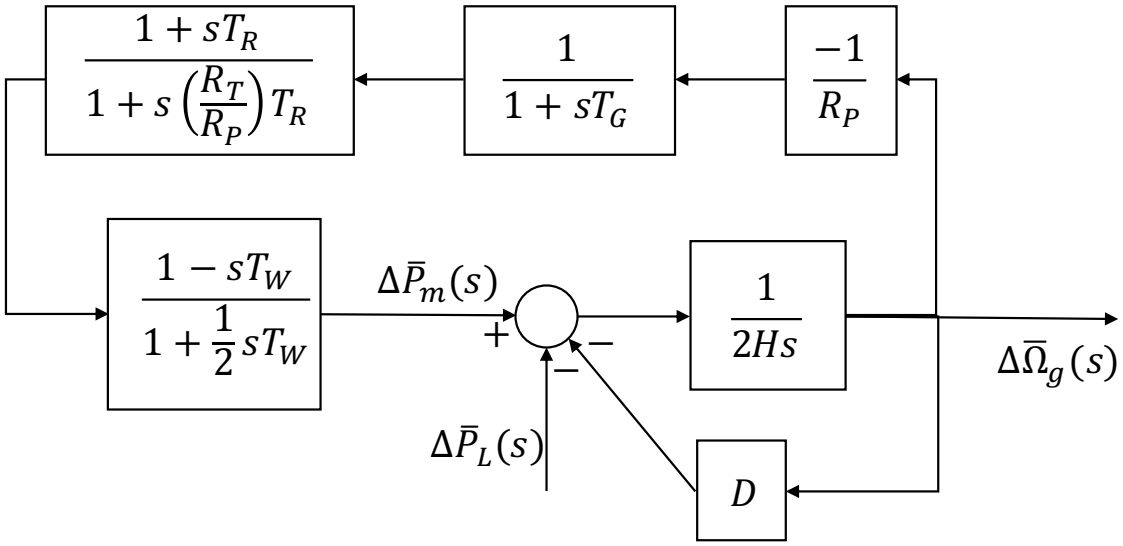


Figure 3.1: Single area LFC model with hydraulic turbine and governor.

### 3.1.2 Steam turbine and governor LFC models

Two additional models were used to test for dependence on the LFC model being used, models for reheat and non-reheat steam turbines. The model for a system based on a steam plant, with turbine and governor transfer functions and load damping is presented as a block diagram in figure 3.2.

The system is dependent on time constants related to the dynamics of steam displacement through piping, valves and reheating circuits, and on the fraction of power that is generated in each turbine section. A steam turbine may be composed of multiple sections, fed with steam at different pressure levels. The model shown in figure 3.2 corresponds to that of a system fed by a steam turbine with high, intermediate and low pressure sections, with a reheater [58, 59]. The time constant of the main inlet volume and steam chest, a volume of steam associated with the main valve that feeds the turbine, is identified as $T_{CH}$. A steam turbine may have a reheater, an additional pass through the boiler between turbine sections for improved efficiency. It adds an associated time constant $T_{RH}$. The fraction of total turbine power generated by the high pressure turbine section is $F_{HP}$. The time constant associated with the crossover piping, which takes steam from intermediate to low pressure turbine sections, may be neglected in a simplified model for a reheat steam turbine, as the crossover time constant is negligible in comparison with the reheat time constant. Typical parameter values are presented in table 3.1 [58].

The diagram for the system with no reheat and a single, high pressure turbine

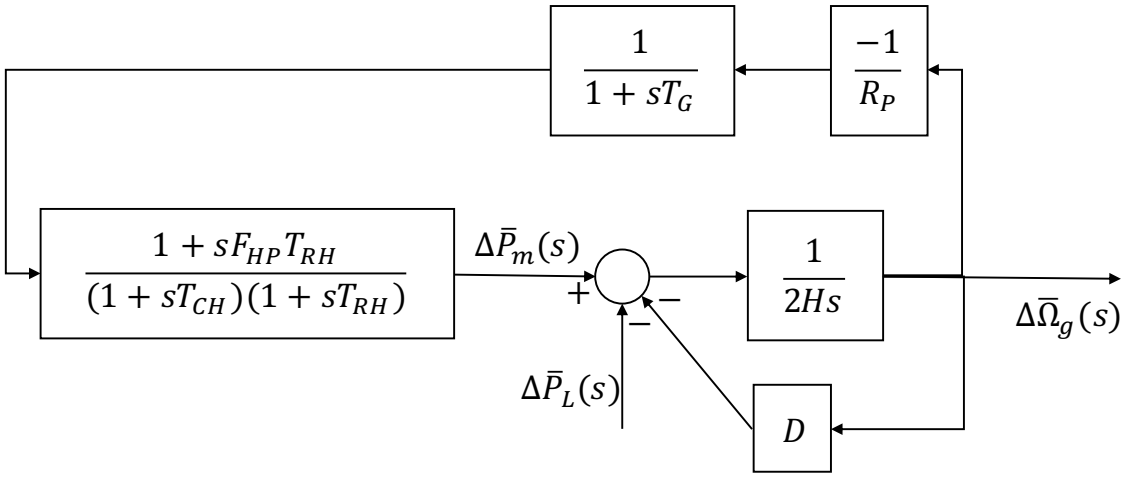


Figure 3.2: Single area LFC model with steam turbine and governor.

section is presented in figure 3.3. It is simpler than the one in figure 3.2, a consequence of having a zero reheater time constant, $T_{RH} = 0$.

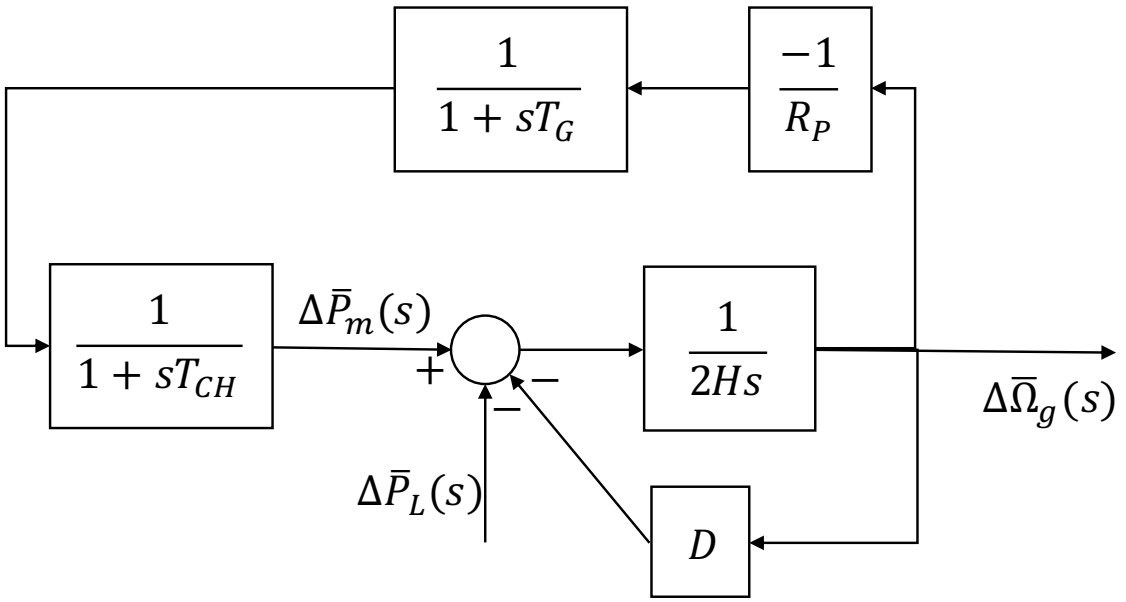


Figure 3.3: Single area LFC model with steam with no reheat turbine and governor.

## 3.2 Synchronverter

In this section, a state space model is developed for a synchronverter connected to a three phase voltage source. The three phase voltage source has constant amplitude $E_{TH}$ and variable frequency $\omega_g(t)$. The synchronverter and the voltage source are connected through per phase impedance $\vec{Z} = Z\angle\theta$. The synchronverter's DC link voltage balance is taken into account. The synchronverter being modelled was implemented in a 3.4 kW experimental setup and experimental results were pub-

Table 3.1: Typical parameters for a reheat steam turbine model.

| Parameter Name | Parameter Symbol | Value |
|---|---|---|
| Governor permanent droop | $R_P$ | 0.05 p.u./p.u. |
| Steam chest time constant | $T_{CH}$ | 0.3 s |
| High pressure turbine section power fraction | $F_{HP}$ | 0.3 |
| Reheat time constant | $T_{RH}$ | 7.0 s |
| Servomotor time constant | $T_G$ | 0.2 s |
| Inertia constant | $H$ | 5.0 s |
| Load damping constant | $D$ | 1.0 p.u./p.u. |

lished [60]. However, this small signal model does not consider a variable inertia, nor does it consider reactive power control, whose control variable is $M_f i_f(t)$, an input signal. A diagram for the modelled controller is presented in figure 3.4.

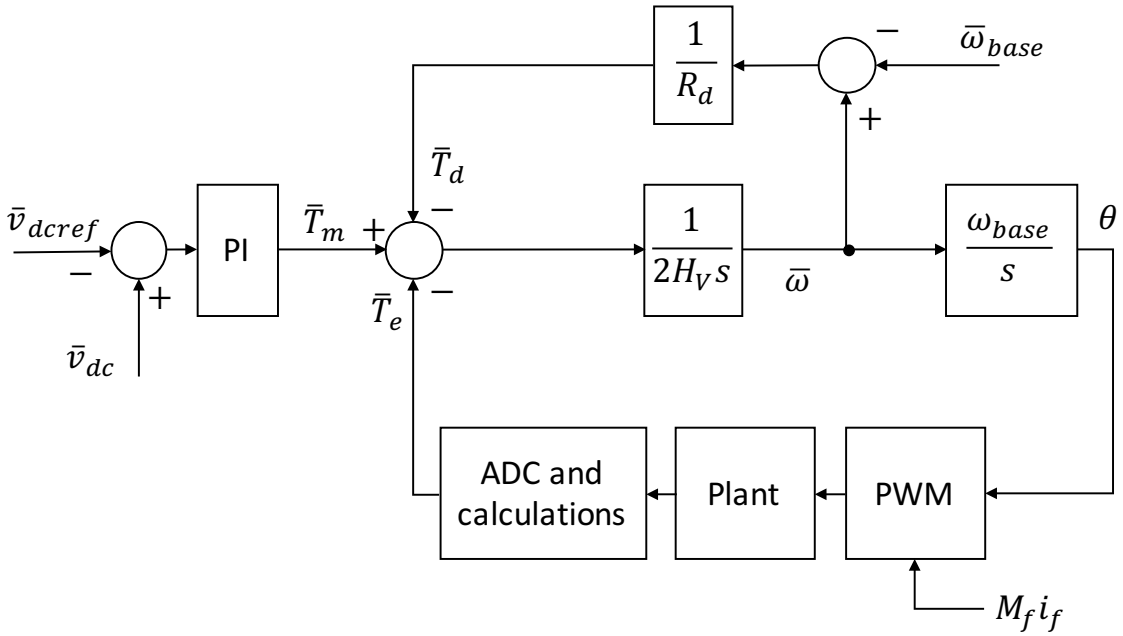


Figure 3.4: Diagram of implemented synchronverter controller.

### 3.2.1 Small-signals model

The synchronverter's swing equation is given by equation (3.15), where $J_V$ is its virtual inertia.

$$J_V \frac{d\omega(t)}{dt} = T_m(t) - T_e(t) - T_d(t) \tag{3.15}$$

Using the relationship $J_V = 2H_V P_{base}/\omega_{base}^2 = 2H_V T_{base}/\omega_{base}$ to substitute into equation (3.15), its form in per unit system may be obtained, as in equation (3.16).

$$2H_V \frac{d\bar{\omega}(t)}{dt} = \bar{T}_m(t) - \bar{T}_e(t) - \bar{T}_d(t) \tag{3.16}$$

Equation (3.16) can be written in terms of variations around a stable equilibrium point, as in equation (3.17).

$$2H_V \frac{d\Delta\bar{\omega}(t)}{dt} = \Delta\bar{T}_m(t) - \Delta\bar{T}_e(t) - \Delta\bar{T}_d(t) \tag{3.17}$$

The DC link dynamics are described by a similar differential equation, considering the circuit shown in figure 3.5, given by equation (3.18), where

- $C$ is the DC link capacitor bank's total capacitance;
- $v_{dc}(t)$ is the voltage across the DC link capacitor bank;
- $i_{be}(t)$ is the DC link current that comes from the back end converter (connected to a power source);
- $i_{fe}(t)$ is the DC link current that goes into the front-end converter (connected to the grid);
- $i_R(t)$ is the DC link current that goes into the resistance connected in parallel with the capacitor bank.

$$C\frac{dv_{dc}(t)}{dt} = i_{be}(t) - i_{fe}(t) - i_R(t) \tag{3.18}$$

A capacitor inertia constant may be defined as in equation (3.19) and used to

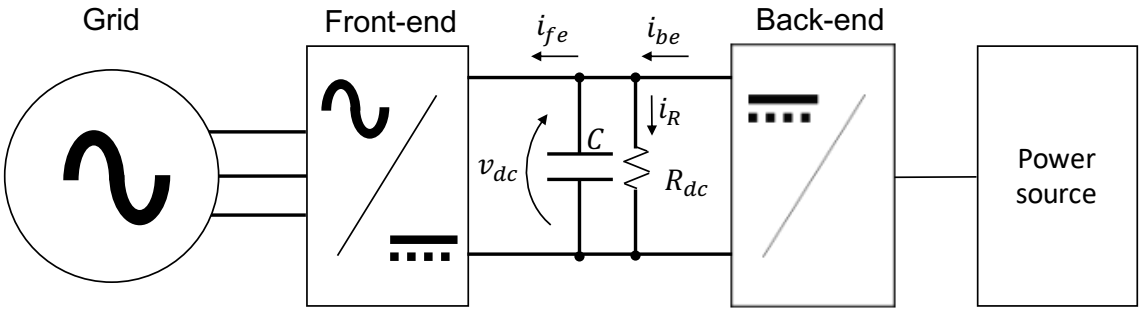


Figure 3.5: Diagram for considered power electronics based generating unit topology. The front-end converter is the one directly connected to the grid. The back-end converter is the interface to the primary power source (generator in a wind turbine or photovoltaic modules) and may be DC-AC or DC-DC.

rewrite equation (3.18) in per unit system.

$$H_C = \frac{1}{2}\frac{Cv_{dcbase}^2}{P_{base}} \tag{3.19}$$

A base current is also defined for DC link currents, as per equation (3.20).

$$i_{dcbase} = \frac{P_{base}}{v_{dcbase}} \tag{3.20}$$

Combining equations (3.19) and (3.20) gives (3.21).

$$C = \frac{2H_C i_{dcbase}}{v_{dcbase}} \tag{3.21}$$

The per unit capacitor differential equation is then given by equation (3.22).

$$2H_C \frac{d\bar{v}_{dc}(t)}{dt} = \bar{i}_{be}(t) - \bar{i}_{fe}(t) - \bar{i}_R(t) \tag{3.22}$$

The DC link current from the back end converter can be calculated from the power provided by the back end converter and the DC link voltage through a non-linear relationship, as shown in equation (3.23).

$$\bar{i}_{be}(t) = \frac{\bar{p}_{be}(t)}{\bar{v}_{dc}(t)} \tag{3.23}$$

It can be linearized around the operating point at $t = 0$, as shown in equation (3.24).

$$\Delta\bar{i}_{be}(t) = -\frac{\bar{p}_{be}(0)}{\bar{v}_{dc}^2(0)}\Delta\bar{v}_{dc}(t) + \frac{1}{\bar{v}_{dc}(0)}\Delta\bar{p}_{be}(t) = -\bar{p}_{be}(0)\Delta\bar{v}_{dc}(t) + \Delta\bar{p}_{be}(t) \tag{3.24}$$

The current drained by the parallel resistance in the DC link $R_{dc}$ is given simply by equation (3.25). The base value for a DC link resistance is given by $R_{dcbase} = v_{dcbase}^2/P_{base}$.

$$\bar{i}_R(t) = \frac{\bar{v}_{dc}(t)}{\bar{R}_{dc}} \therefore \Delta\bar{i}_R(t) = \frac{\Delta\bar{v}_{dc}(t)}{\bar{R}_{dc}} \tag{3.25}$$

The active power $p_{fe}(t)$ provided by the synchronverter, considering two three phase voltage sources with per unit amplitudes $\bar{e}_{synch}(t)$ and $\bar{E}_{TH}$, a phase difference $\delta(t)$ and coupling impedance $\bar{\bar{Z}} = \bar{Z}\angle\theta$, as illustrated in figure 3.6, is given by equation (3.26). This expression neglects current transients and equals the steady state active power if we consider constant $\bar{e}_{synch}(t)$ and $\delta(t)$.

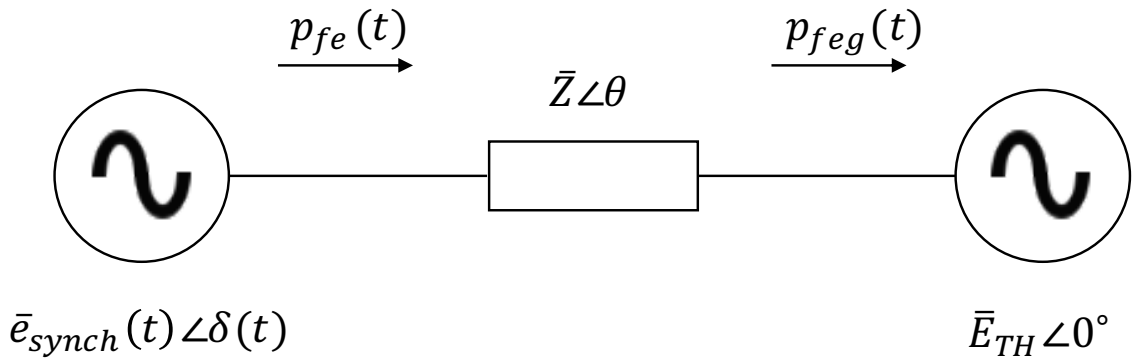


Figure 3.6: Single-line diagram of synchronverter connected to a voltage source.

$$\bar{p}_{fe}(t) = \frac{\bar{e}_{synch}(t)}{\bar{Z}} \left[\bar{e}_{synch}(t)\cos\theta - \bar{E}_{TH}\cos\left(\theta + \delta(t)\right)\right] \tag{3.26}$$

The DC link current going into the front-end converter can then be calculated as per equation (3.27).

$$\bar{i}_{fe}(t) = \frac{\bar{p}_{fe}(t)}{\bar{v}_{dc}(t)} = \frac{\bar{e}_{synch}(t)}{\bar{v}_{dc}(t)\bar{Z}} \left[\bar{e}_{synch}(t)\cos\theta - \bar{E}_{TH}\cos\left(\theta + \delta(t)\right)\right] \tag{3.27}$$

The synchronverter's Root Mean Square (RMS), phase-to-phase internal voltage amplitude $e_{synch}(t)$ is proportional to $M_f i_f(t)$, which will be redefined according to equation (3.28). Its per unit form is given by equation (3.29).

$$\psi_f(t) = M_f i_f(t) \tag{3.28}$$

$$\bar{\psi}_f(t) = \frac{M_f i_f(t)}{\psi_{fbase}} \tag{3.29}$$

In this implementation, the synchronverter's internal voltage did not take into account its speed $\bar{\omega}(t)$, considering its deviations from 1 p.u. to be negligible. Considering the amplitude of the fundamental component in Sine Pulse-Width Modulation (SPWM), the synchronverter's internal voltage is then given by equation (3.30), where $\psi_f(t)$ may be regarded as an amplitude modulation ratio [61].

$$e_{synch}(t) = \frac{\sqrt{3}}{2\sqrt{2}} v_{dc}(t)\psi_f(t) \tag{3.30}$$

The per unit voltage can be obtained dividing equation (3.30) by the base RMS phase-to-phase voltage $V_{base}$. Substituting the DC link voltage for the product between its per unit value and its base value helps us define a base value for $\psi_f(t)$, as shown in equation (3.31).

$$\bar{e}_{synch}(t) = \frac{e_{synch}(t)}{V_{base}} = \frac{\sqrt{3}}{2\sqrt{2}} \frac{v_{dcbase}}{V_{base}} \bar{v}_{dc}(t)\psi_f(t) \tag{3.31}$$

If we then choose the base value for $\psi_f(t)$ as shown in equation (3.32), the synchronverter per unit voltage amplitude can be expressed as the product between DC link voltage and the amplitude modulation ratio, as in equation (3.33), where $v_{base}$ is the peak phase voltage.

$$\psi_{fbase} = \frac{2\sqrt{2}}{\sqrt{3}} \frac{V_{base}}{v_{dcbase}} = 2\frac{v_{base}}{v_{dcbase}} \tag{3.32}$$

$$\bar{e}_{synch}(t) = \bar{v}_{dc}(t)\bar{\psi}_f(t) \tag{3.33}$$

Substituting (3.33) into (3.27) gives (3.34).

$$\bar{i}_{fe}(t) = \frac{1}{\bar{Z}}\left[\bar{v}_{dc}(t)\bar{\psi}_f^2(t)\cos\theta - \bar{\psi}_f(t)\bar{E}_{TH}\cos\left(\theta + \delta(t)\right)\right] \tag{3.34}$$

Linearizing equation (3.34) leads to equation(3.35), where $k = 2\bar{\psi}_f(0)\bar{v}_{dc}(0)\cos\theta - \bar{E}_{TH}\cos\left(\theta + \delta(0)\right)$.

$$\begin{aligned}\Delta\bar{i}_{fe}(t) = \frac{1}{\bar{Z}}\Big\{&\bar{\psi}_f(0)\bar{E}_{TH}\sin\left(\theta + \delta(0)\right)\Delta\delta(t) + \\ &\bar{\psi}_f(0)^2\cos\theta\Delta\bar{v}_{dc}(t) + k\Delta\bar{\psi}(t)\Big\}\end{aligned} \tag{3.35}$$

Equations (3.22), (3.24), (3.25), (3.35) can now be used to write the first linearized differential equation, equation (3.36).

$$\frac{d\Delta\bar{v}_{dc}\left(t\right)}{dt} = \frac{1}{2H_C}\left[\Delta\bar{i}_{be}\left(t\right) - \Delta\bar{i}_{fe}\left(t\right) - \Delta\bar{i}_R\left(t\right)\right] \tag{3.36}$$

The electromagnetic torque in this synchronverter implementation is calculated from measured voltages and currents as the electric power flowing out of the front-end converter, neglecting the synchronverter speed's deviations from 1 p.u. Therefore, $\Delta\bar{T}_e(t) = \Delta\bar{p}_{fe}(t)$, given by equation (3.37).

$$\begin{aligned}\Delta\bar{p}_{fe}(t) = \frac{1}{\bar{Z}}\Big\{&\bar{\psi}_f(0)\bar{v}_{dc}(0)\bar{E}_{TH}\sin\left(\theta + \delta(0)\right)\Delta\delta(t) + \\ &k\bar{\psi}_f(0)\Delta\bar{v}_{dc}(t) + k\bar{v}_{dc}(0)\Delta\bar{\psi}(t)\Big\}\end{aligned} \tag{3.37}$$

If $\omega(0) = \omega_{base}$, then the damping or droop torque and its expression in terms of small signals are given by equation (3.38), where $R_d$ is the permanent droop setting.

$$\bar{T}_d(t) = \frac{1}{R_d}(\bar{\omega}(t) - \bar{\omega}_{base}) \therefore \Delta\bar{T}_d(t) = \frac{\Delta\bar{\omega}(t)}{R_d} \tag{3.38}$$

Equations (3.37) and (3.38) can now be used to write the virtual machine's linearized differential equation, equation (3.39), where $\Delta\bar{T}_m(t)$ is still an input.

$$\frac{d\Delta\bar{\omega}(t)}{dt} = \frac{1}{2H_V}\left[\Delta\bar{T}_m(t) - \Delta\bar{T}_e(t) - \Delta\bar{T}_d(t)\right] \tag{3.39}$$

The last synchronverter differential equation is the load angle's. The load angle grows with the difference between the voltages' frequencies $\omega_{slip}(t) = \omega(t) - \omega_g(t)$, where $\omega_g(t)$ is the variable frequency for the three phase voltage source to which the synchronverter is connected, according to equation (3.40).

$$\delta\left(t\right) = \delta\left(0\right) + \int_0^t \omega_{slip}(t')dt' = \delta\left(0\right) + \omega_{base}\int_0^t \bar{\omega}_{slip}(t')dt' \tag{3.40}$$

If it is assumed that both frequencies are initially equal, then $\omega_{slip}(0) = 0 \therefore \Delta\omega_{slip}(t) = \omega_{slip}(t)$ and $\Delta\omega(t) - \Delta\omega_g(t) = \omega(t) - \omega(0) - \omega_g(t) + \omega_g(0) = \omega(t) - \omega_g(t)$. Therefore, equation (3.40) may be rewritten as equation (3.41).

$$\Delta\delta\left(t\right) = \omega_{base}\int_0^t \Delta\bar{\omega}_{slip}(t')dt' = \omega_{base}\int_0^t \left[\Delta\bar{\omega}(t') - \Delta\bar{\omega}_g(t')\right]dt' \tag{3.41}$$

The derivative of equation (3.41) gives the last differential equation, equation (3.42).

$$\frac{d\Delta\delta\left(t\right)}{dt} = \omega_{base}\left[\Delta\bar{\omega}(t) - \Delta\bar{\omega}_g(t)\right] \tag{3.42}$$

The initial conditions will be determined assuming the initial DC link voltage $\bar{v}_{dc}(0) = 1$, the initial power from the back end converter $\bar{p}_{be}(0)$, the initial amplitude modulation ratio $\bar{\psi}_f(0) = 1$ and the initial grid frequency is $\omega_g(0) = \omega_{base}$ or $\bar{\omega}_g(0) = 1$. The remaining variables' initial values will be determined from the condition that the system is at an equilibrium at $t = 0$, as stated by (3.43).

$$\begin{aligned}
\frac{d\bar{\omega}(t)}{dt}|_{t=0} &= 0 \therefore \bar{T}_m(0) - \bar{T}_e(0) - \bar{T}_d(0) = 0 \\
\frac{d\delta\left(t\right)}{dt}|_{t=0} &= 0 \therefore \bar{\omega}(0) = \bar{\omega}_g(0) = \bar{\omega}_{base} = 1 \\
\frac{d\bar{v}_{dc}\left(t\right)}{dt}|_{t=0} &= 0 \therefore \bar{i}_{be}\left(0\right) = \bar{i}_{fe}\left(0\right) + \bar{i}_R\left(0\right)
\end{aligned} \tag{3.43}$$

The equilibrium condition for $\bar{v}_{dc}(t)$, leads to equation (3.44), defining the initial current to the front-end converter.

$$\bar{i}_{fe}(0) = \frac{\bar{p}_{be}(0)}{\bar{v}_{dc}(0)} - \frac{\bar{v}_{dc}(0)}{\bar{R}_{dc}} \tag{3.44}$$

The condition for load angle equilibrium leads to $\bar{T}_d(0) = \frac{1}{R_d}(\bar{\omega}(0) - \bar{\omega}_{base}) = 0$. Therefore, from the equilibrium condition for $\bar{\omega}(t)$, equation (3.45) follows.

$$\bar{T}_m(0) = \bar{T}_e(0) = \bar{p}_{fe}(0) \tag{3.45}$$

The initial value for the load angle $\delta(0)$ may be found by substituting the value found for the initial current to the front-end converter into equation (3.34) and rearranging it, as in equation (3.46).

$$\cos\left(\theta + \delta(0)\right) = \frac{1}{\bar{E}_{TH}}\left[\bar{\psi}_f(0)\bar{v}_{dc}(0)\cos\theta - \frac{\bar{Z}\bar{i}_{fe}(0)}{\bar{\psi}_f(0)}\right] \tag{3.46}$$

Let us now consider the DC link voltage regulation by a PI controller. If we consider the diagram in figure 3.4, then equation (3.47) follows, where $\bar{v}_{dcref}$ is the initial value, $\bar{v}_{dc}(0) = \bar{v}_{dcref}$, and the reference value for the DC link voltage

regulation.

$$\bar{T}_m(t) = \bar{T}_m(0) + k_p(\bar{v}_{dc}(t) - \bar{v}_{dcref}) + k_i \int_0^t \bar{v}_{dc}(\tau) - \bar{v}_{dcref} d\tau \tag{3.47}$$

Equation (3.47) may be written as (3.48).

$$\Delta\bar{T}_m(t) = k_p \Delta\bar{v}_{dc}(t) + k_i \int_0^t \Delta\bar{v}_{dc}(\tau) d\tau \tag{3.48}$$

Differentiating equation (3.48) leads to equation (3.49). A new state variable may be defined as $\Delta\bar{T}_m(t)$.

$$\frac{d\Delta\bar{T}_m(t)}{dt} = k_p \frac{d\Delta\bar{v}_{dc}(t)}{dt} + k_i \Delta\bar{v}_{dc}(t) \tag{3.49}$$

Substituting expression (3.36) into (3.49) leads to the last differential equation, equation (3.50).

$$\frac{d\Delta\bar{T}_m(t)}{dt} = \frac{k_p}{2H_C} \left[\Delta\bar{i}_{be}(t) - \Delta\bar{i}_{fe}(t) - \Delta\bar{i}_R(t)\right] + k_i \Delta\bar{v}_{dc}(t) \tag{3.50}$$

Finally, the electrical power after the coupling impedance $\Delta\bar{p}_{feg}(t)$, which is absorbed by voltage source $\bar{E}_{TH}$, can be written as equation (3.51).

$$\bar{p}_{feg}(t) = \frac{\bar{E}_{TH}}{\bar{Z}} \left[\bar{e}_{synch}(t) \cos(\theta - \delta(t)) - \bar{E}_{TH} \cos\theta\right] \tag{3.51}$$

Substituting equation (3.33) into (3.51) gives equation (3.52).

$$\bar{p}_{feg}(t) = \frac{\bar{E}_{TH}}{\bar{Z}} \left[\bar{v}_{dc}(t)\bar{\psi}(t) \cos(\theta - \delta(t)) - \bar{E}_{TH} \cos\theta\right] \tag{3.52}$$

The electrical power $\Delta\bar{p}_{feg}(t)$ can then be written as a function of state variables and input variables, as in equation (3.53).

$$\begin{aligned} \Delta\bar{p}_{feg}(t) = \frac{\bar{E}_{TH}}{\bar{Z}} \big[&\bar{v}_{dc}(0)\bar{\psi}(0) \sin(\theta - \delta(0))\Delta\delta(t) + \\ &\bar{\psi}(0) \cos(\theta - \delta(0))\Delta\bar{v}_{dc}(t) + \\ &\bar{v}_{dc}(0) \cos(\theta - \delta(0))\Delta\bar{\psi}(t)\big] \end{aligned} \tag{3.53}$$

After developing these expressions, we may write the state space equation (3.54).

$$\begin{aligned} \dot{\vec{x}}(t) &= A\vec{x}(t) + B\vec{u}(t) \\ \vec{y}(t) &= C\vec{x}(t) + D\vec{u}(t) \end{aligned} \tag{3.54}$$

The state variables vector $\vec{x}(t)$ is given by equation (3.55).

$$\vec{x}(t) = \begin{bmatrix} \Delta\bar{\omega}(t) \\ \Delta\delta(t) \\ \Delta\bar{v}_{dc}(t) \\ \Delta\bar{T}_m(t) \end{bmatrix} \tag{3.55}$$

The input variables vector $\vec{u}(t)$ is given by equation (3.56).

$$\vec{u}(t) = \begin{bmatrix} \Delta\bar{p}_{be}(t) \\ \Delta\bar{\omega}_g(t) \\ \Delta\bar{\psi}_f(t) \end{bmatrix} \tag{3.56}$$

The output variables vector $\vec{y}(t)$ is given by equation (3.57).

$$\vec{y}(t) = \begin{bmatrix} \Delta\bar{\omega}(t) \\ \Delta\delta(t) \\ \Delta\bar{v}_{dc}(t) \\ \Delta\bar{p}_{feg}(t) \end{bmatrix} \tag{3.57}$$

### 3.2.2 Large signals validation

A large signals synchronverter model was constructed in PSCAD™/EMTDC™to validate the small signals model. Here, the synchronverter is modelled as an ideal, symmetrical, three-phase voltage source with a coupling series impedance, as shown in figure 3.7. This voltage source's amplitude is made directly proportional to the DC link voltage, as is the case in two-level, PWM-based VSC [61, 62]. The synchronverter voltage source's peak phase amplitude is given by $V_{phase,peak} =$

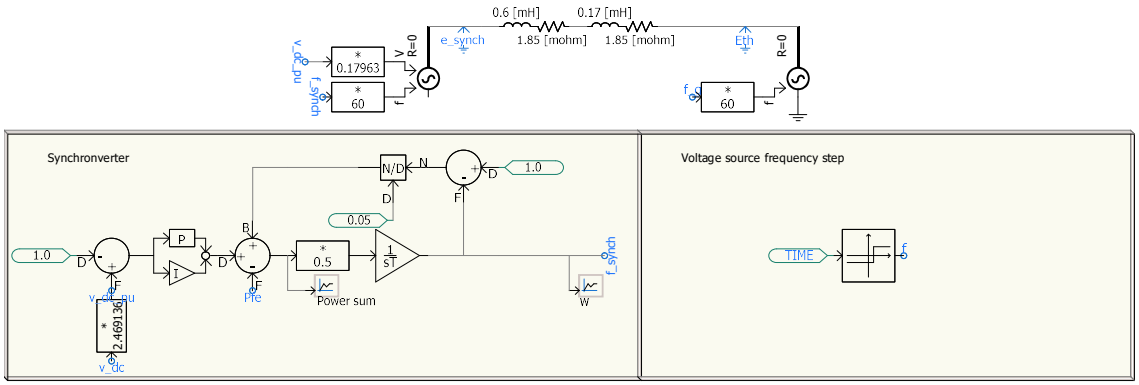


Figure 3.7: Circuit built in PSCAD to validate the small-signals model through the response to a step in grid frequency. The time constant in the synchronverter integrator is given by $T = 2H_V$.

$\sqrt{2}V_{phase,base,rms}\bar{v}_{dc}(t) = \sqrt{2/3}V_{line,base,rms}\bar{v}_{dc}(t) \approx 0.17963\bar{v}_{dc}(t)$ kV, for a 220 V base *rms* line voltage.

DC link voltage is modelled according to the nonlinear equation (3.18) and assumes a constant back-end power input, as shown in figure 3.8. The capacitor current is computed and fed into an integrator with the capacitance as its time constant. A switch is used to avoid invalid current values that occur during the first simulation step, when the signal $v\_dc\_V$, the DC link voltage in volts, is still zero, causing divisions by zero.

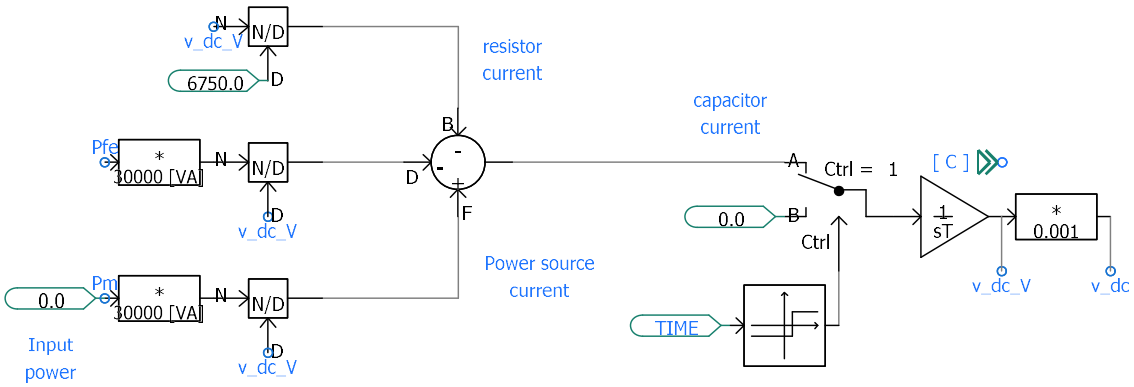


Figure 3.8: DC link capacitor model considering currents from back-end and front-end converters and into a shunt resistance.

The simulation is allowed to settle in an equilibrium point, then a step is applied to the grid's frequency from 60 Hz to 59.9 Hz. The state and output variables' deviations from the initial conditions are computed during the simulation for comparison against the small signals model.

Three signals of interest show good agreement between the developed small-signal model and the system modelled in PSCAD$^{\text{TM}}$. These are the deviations for power into the grid $\Delta p_{feg}(t)$, front-end power $\Delta p_{fe}(t)$ and DC link voltage $\Delta v_{dc}(t)$, shown in figures 3.9, 3.10 and 3.11, respectively.

### 3.2.3 External DC link regulation

It shall be considered additionally the case that the front-end converter does not need to control its DC link voltage, because a back-end converter is performing this task. Then, the DC link controller equation (3.49) will actually give a reference active power for the back-end converter, as per equation (3.58), and the mechanical torque signal $\Delta T_m(t)$ will be a reference active power input for the synchronverter.

$$\frac{d\Delta\bar{p}_{be,ref}(t)}{dt} = k_p\frac{d\Delta\bar{v}_{dc}(t)}{dt} + k_i\Delta\bar{v}_{dc}(t) \tag{3.58}$$

The actual back-end converter power input into the DC link will depend on an

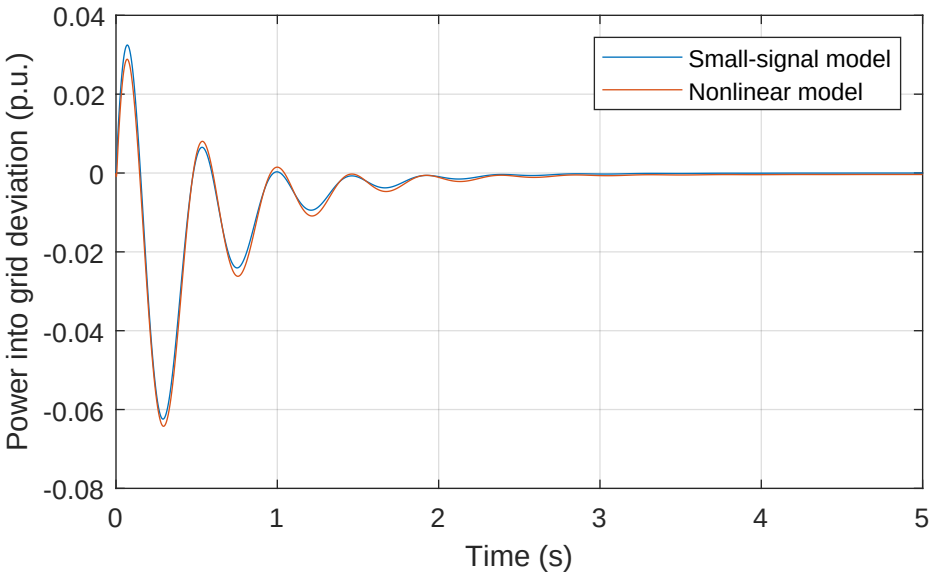


Figure 3.9: Effect of a 0.1 Hz grid frequency step on the power that goes into the grid, from a synchronverter that regulates its own DC link. Comparison between small-signal and PSCAD models.

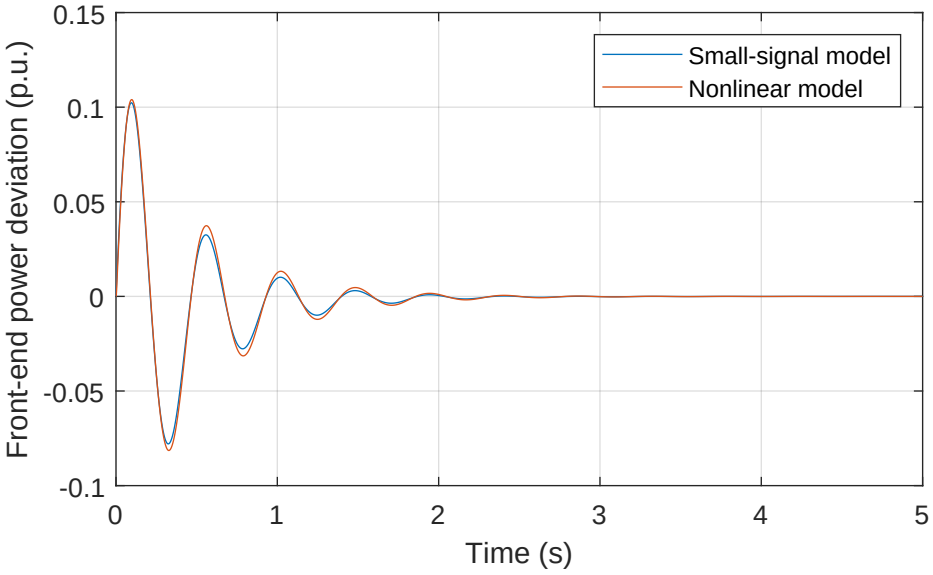


Figure 3.10: Effect of a 0.1 Hz grid frequency step on the front-end (before coupling impedance) of a synchronverter that regulates its own DC link. Comparison between small-signal and PSCAD models.

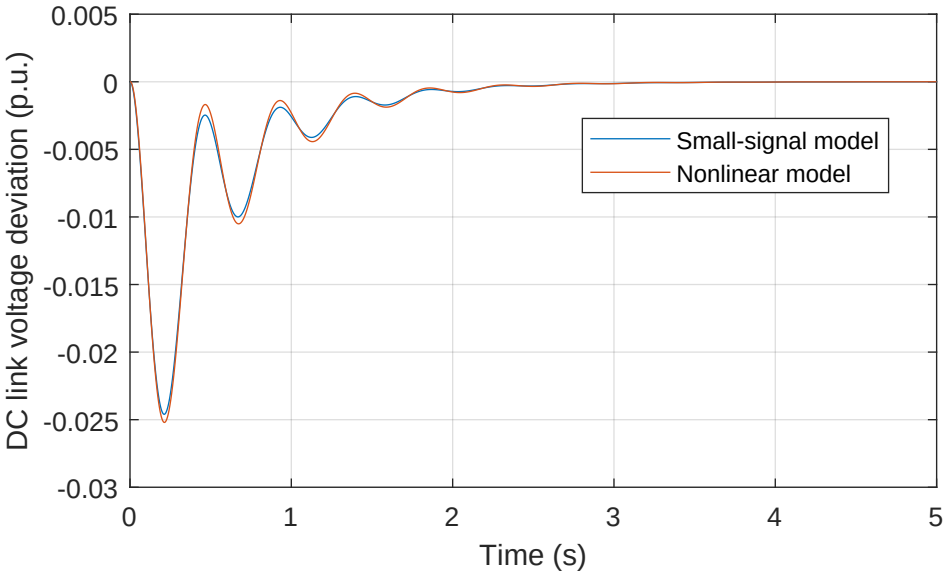


Figure 3.11: Effect of a 0.1 Hz grid frequency step on the DC link voltage of a synchronverter that regulates its own DC link. Comparison between small-signal and PSCAD models.

actuator transfer function $G_{be}(s)$, as in equation (3.59), which will depend on the back-end converter control and the power source to which it is connected.

$$\Delta\bar{P}_{be}(s) = G_{be}(s)\Delta\bar{P}_{be,ref}(s) \tag{3.59}$$

## 3.3 Static synchronous machine

Another control concept has been proposed, developed and tested with the experimental setup presented in chapter 5, and it has been called a Static Synchronous Machine (SSM). The term *static* was used instead of *virtual*, as there are no virtual parameters in the sense used by other control topologies. The term *synchronous machine* was used instead of *generator*, as there is nothing in this control topology that implies it is supposed to function as a generator.

I propose that the converter's AC voltage angular speed be equal to its DC link voltage, in a per-unit system, i.e. $\bar{\omega} = \bar{v}_{dc}$. The synchronverter's active power loop can be performed by the converter's own power circuit. A converter's energy is stored in its DC link capacitor, as an electrical machine's energy is stored in its rotor. The former, as electrostatic energy and the latter, as kinetic energy. Table 3.2 summarizes the mathematical relationships for a capacitor or a rotor's dynamics, making explicit the analogy between both forms of energy storage.

Table 3.2: Relationships between machine rotor and DC link capacitor

| **Capacitor** | **Rotor** |
|---|---|
| $E = \frac{1}{2}Cv_{dc}^2$ | $E = \frac{1}{2}J\omega^2$ |
| $P = v_{dc}i$ | $P = \omega T$ |
| $Cv_{dc}^{\cdot} = i$ | $J\dot{\omega} = T$ |
| $H = \frac{1}{2}\frac{Cv_{dcbase}^2}{P_{base}}$ | $H = \frac{1}{2}\frac{J\omega_{base}^2}{P_{base}}$ |

As is the case with synchronous machines, the basic synchronization mechanism consists of the fact that, given a DC link voltage higher than the grid frequency, in per-unit, the SSM's output voltage load angle will increase, leading to an increase of power output into the grid, consequently decreasing DC link voltage. Similarly, a low DC link voltage with respect to the grid frequency will decrease load angle (or increase a negative load angle's absolute value) and cause output power to decrease (or increase power consumption), lifting DC link voltage. An SSM implementation could be represented by the diagram in figure 3.12, which can be compared with the synchronverter's in figure 3.4.

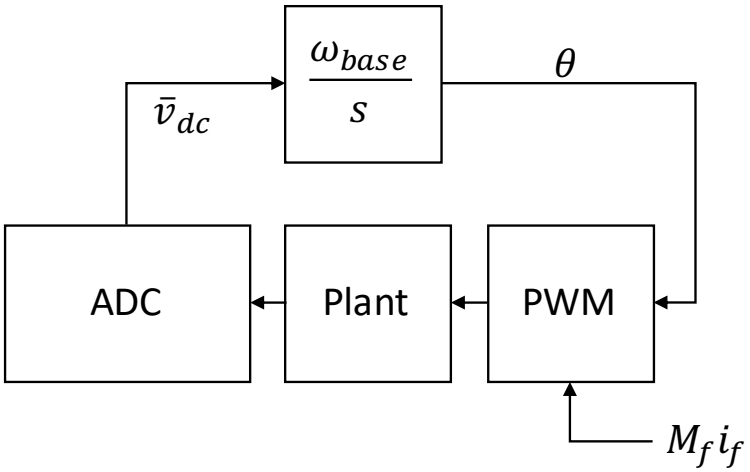


Figure 3.12: Block diagram of an SSM.

For a typical VSC DC link, this system would be quite underdamped. This had previously been noted by [53], which highlights the possible equivalence between a machine's rotor speed and a voltage source converter's DC link voltage and proposes output voltage frequency to be determined from DC link voltage, but through a transfer function, for additional damping.

I do not propose dynamics to be added to the relationship between DC link voltage and AC voltage angular speed. Similarly to generating units based on synchronous machines, I propose that DC link regulation be performed by the back-end converter, which is connected to the primary power source. That converter will be responsible for implementation of the front-end converter's droop behavior and

extend to the DC link voltage the information implicitly transmitted through the system frequency. I.e., the back-end converter will implement the same, system-wide droop characteristic where 5% grid frequency (or DC link voltage) deviation causes a 100% active power deviation. Amidst growing interest on AC and DC microgrids interacting with the main EPS, this is a worthwhile feature to study.

With this configuration, power electronics based generation becomes more similar to traditional generation, with a correspondence between system elements as presented in figure 3.13. A similar comparison was presented by [57]. Some advan-

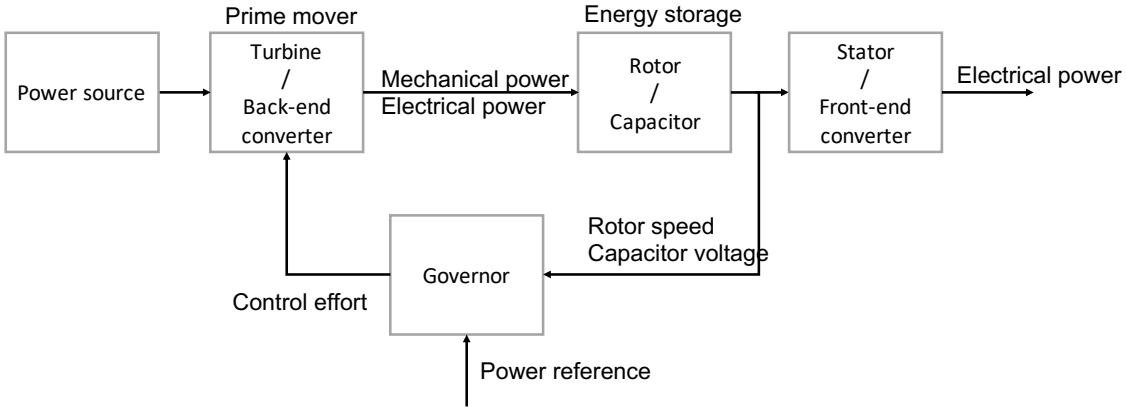


Figure 3.13: Relationship between SSM and SM generating units.

tages of this concept may be pointed out:

- does not need to calculate powers acting upon a virtual rotor (electromagnetic, damping, or governor). Its frequency is calculated by an analog PLL, the converter's DC link capacitor and three-phase power circuit;
- therefore, it presents low computational burden;
- makes DC link energy part of the total system energy in a simple, less convoluted way. This is interesting as it maintains the existing interpretation of inertia's role in power system stability;
- for synchronverters and similar control strategies, the DC link's dynamics are not clearly integrated into the synchronous machine equivalent model that they intend to be, although they may have a significant impact on it;
- allows for DC droop mechanisms as multiple converters feed a DC link, without communications, with each converter's power being proportional to voltage deviation (they don't need to measure AC grid frequency, because it is "synchronized" with the DC link voltage).

Additionally, although this is not necessarily an advantage, this model automatically includes a direct proportionality dependence of AC voltage amplitude on the DC

link voltage, analogous to the relationship between AC voltage amplitude and rotor speed in synchronous machines.

It should also be pointed out that it does not possess a programmable inertia-related parameter, such as a virtual inertia. Another disadvantage is its dependence on another system for DC link voltage damping. This other system may be a back-end power source able to modulate output power or a controllable DC load.

## 3.4 Model sampling

The main chosen method of analyzing different generating units' frequency support capabilities was model sampling. Model sampling means simply substituting model parameters for different values, creating different samples of a base model.

This can be done for multiple parameters in a model. If parameter $a$ in a model is sampled at $N$ different values, and parameter $b$ is sampled at $M$ different values, one obtains $N \times M$ different versions, possible instances of such a model. Parameters can also be jointly sampled, as a sampling set. For example, parameters $a$ and $b$ might be sampled for $N$ different values of each, without combining every $a$ and $b$ value, but sampling as $N$ pairs $(a_i, b_i)$ and obtaining $N$ different model samples.

MATLAB®, a computer program with tools for problem solving in several fields in science and engineering, offers a Control System Toolbox™, which is equipped with the capability of quickly analyzing a number of different versions of a linear system through a framework for parameter variation studies. This includes classes such as *realp*, used for specifying real-valued, tunable model parameters, *genmat*, *genss*, and functions such as *sampleBlock*, *rsampleBlock*. *Genss* builds generalized state-space models, state-space models dependent on tunable parameters. Functions such as *step*, for simulating a model's step response, *pole*, for calculating a model's poles, *connect*, for connecting multiple models together, *bode*, for calculating a model's Bode plot, and *nyquist*, for calculating a model's Nyquist plot, are ready to work with *genss* objects. Functions *sampleBlock* and *rsampleBlock* create sets of models, or model arrays, through sampling of a *genss* either for user provided parameter values (*sampleBlock*) or for randomly generated values (*rsampleBlock*).

Model sampling can quickly lead to a large number of samples as the number of sampled parameters grows. Interpreting the resulting data can therefore become a challenge. Functions were developed to plot correlations between sampled models' outputs under different conditions, one and two-dimensional Partial Dependence Plots (PDP), Individual Conditional Expectation (ICE) plots and for color mapping of sampled models' time response and pole-zero plots.

### 3.4.1 Single parameter sampling results

The models developed in sections 3.1 and 3.2 were used to evaluate the effect of the presented synchronverter controller and variations on its parameters on an EPS's frequency following a load-generation unbalance. A synchronous machine swing equation model is used for comparison. These show that the virtual inertia of synchronous generator mimicking controllers is not the same as an actual synchronous generator's inertia if DC link voltage regulation by the front end converter is required. If DC link regulation by the front end converter is not required, then the primary power source (from the back end converter) will be required to modulate its output in response to DC link voltage deviations, which in turn are coupled with grid frequency deviations. In the end, if converters need to mimic a synchronous machine's response, primary power source will be required to respond to grid frequency deviations.

The two models are connected through the synchronverter's output power after its coupling impedance, $\Delta p_{feg}(t)$, which adds to the LFC model's power sum, accelerating the equivalent machine rotor, and the LFC model's frequency $\omega_g(t)$, which dictates the frequency of the voltage source to which the synchronverter is connected. The synchronverter output power is multiplied by a gain which corrects for the difference in base powers, changing from the synchronverter's base power $P_{base}$ to the equivalent system's base power $P_{systemBase}$, as shown in figure (3.14). The ratio $P_{base}/P_{systemBase}$ can be adjusted for different power level ratios between the generation unit controlled by a synchronverter and the equivalent system. This way of connecting the LFC and the synchronverter models is equivalent to how two LFC models are connected in a two area LFC model.

Comparison with a synchronous machine is made through the model shown in figure 3.15. It is a slight modification from the synchronous machine's classical swing equation that considers a variable frequency for the bus to which the machine is connected. The damping torque here is a component of the electromagnetic torque proportional to slip speed $\omega_{slip}$, the difference between the machine angular speed and the grid's, a simple way of accounting for the machine's damping windings [63, 64]. After connecting both systems' signals, from figures 3.14 and 3.15 the resulting system can be represented by the block diagram shown in figure 3.16.

The parameters used for the LFC model were typical values for an isolated hydroelectric system according to [58] and they are summarized in table 3.3. The governor permanent droop parameter is also the same value as the one set by ONS. The synchronverter parameters were taken from a 30 kVA experimental setup built in our laboratory and they're summarized in table 3.4. For the synchronous machine model, shown in figure 3.15, $K_D = 1/R_d$ and $K_s$ is the same coupling coefficient

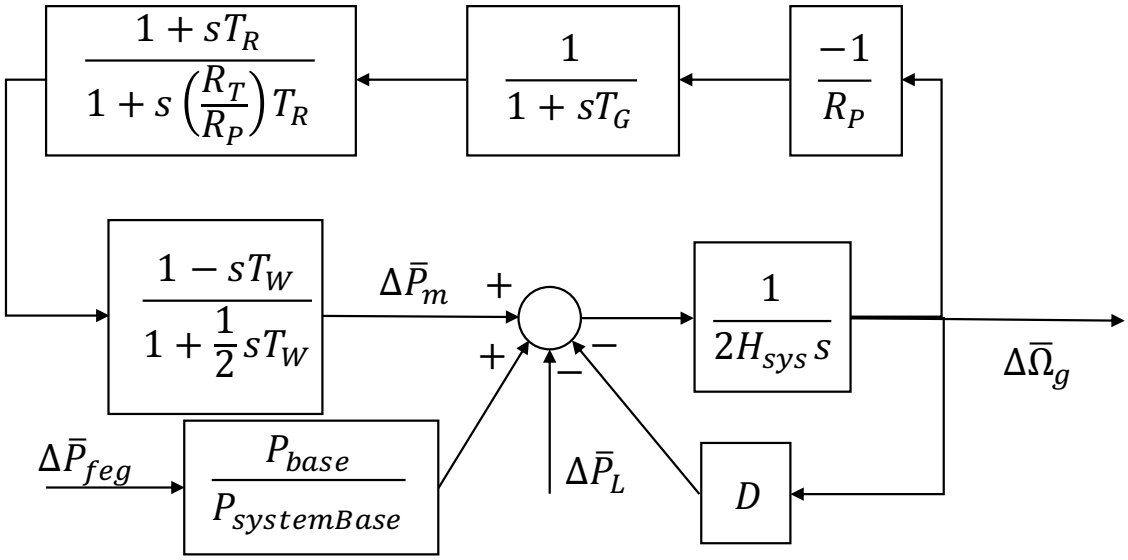


Figure 3.14: LFC model diagram showing signals that connect it to the synchronverter model.

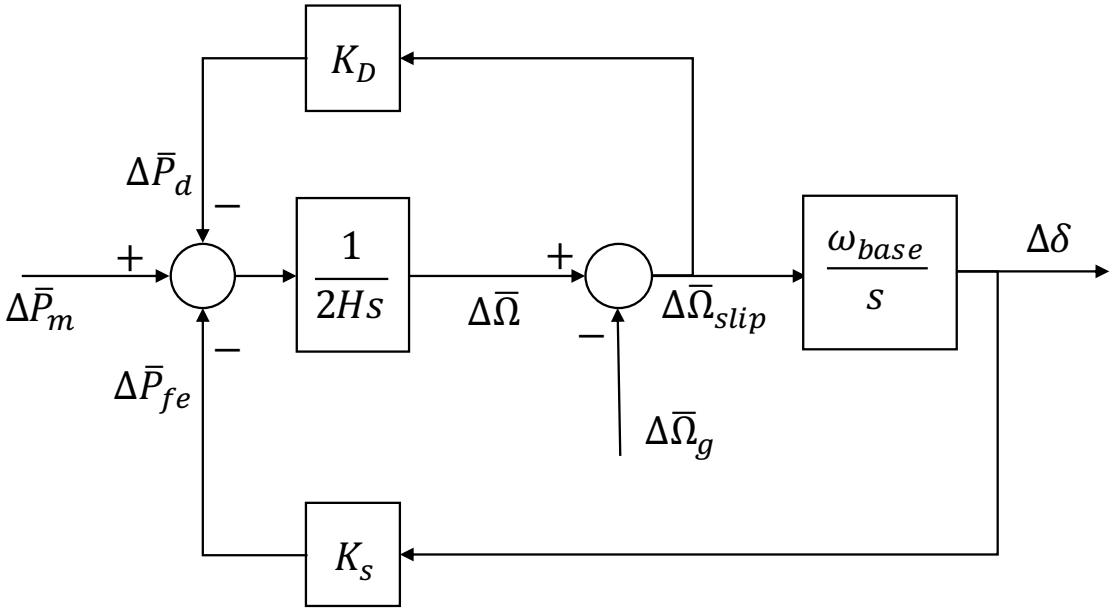


Figure 3.15: Diagram representing a synchronous machine's swing equation when considering a varying grid frequency.

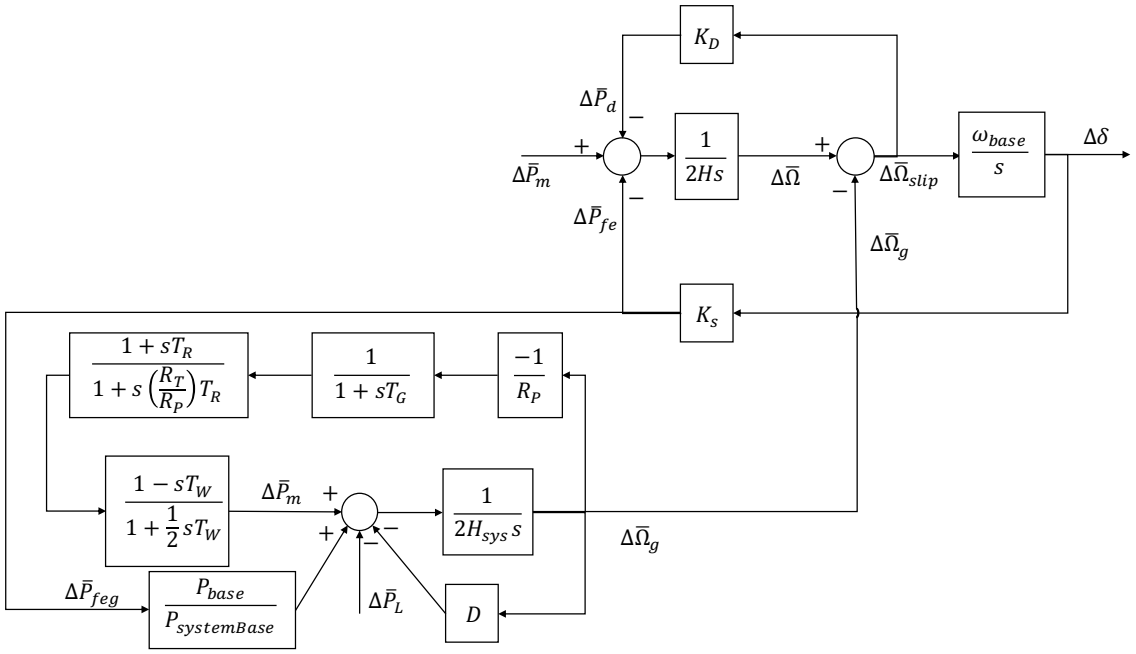


Figure 3.16: Block diagram showing the interconnection of the hydropower plant and the machine models.

between $\Delta\delta$ and $\Delta p_{fe}$ determined in the synchronverter model. The same initial conditions, base values and coupling impedance are used as with the synchronverter model. Coupling impedance losses were neglected for the synchronous machine model, so that $\Delta p_{fe} = \Delta p_{feg}$.

Table 3.3: Typical parameters for a hydroelectric plant model with governor and turbine dynamics.

| Parameter Name | Parameter Symbol | Value |
|---|---|---|
| Governor permanent droop | $R_P$ | 0.05 p.u./p.u. |
| Governor transient droop | $R_T$ | 0.38 p.u./p.u. |
| Governor transient reset time | $T_R$ | 5.0 s |
| Water starting time | $T_W$ | 1.0 s |
| Gate servomotor time constant | $T_G$ | 0.2 s |
| Inertia constant | $H_{sys}$ | 3.0 s |
| Load damping constant | $D$ | 1.0 p.u./p.u. |

Different model samples are generated through variation of a parameter in the linear system, as explained in section 3.4. The following results have been obtained through such a method to show the influence of different parameters in a generating unit's ability to provide grid frequency support. The graphs based on color maps should be interpreted as time responses for multiple versions of one linear system, each version with a different value for a given parameter and each value associated with a color.

Table 3.4: Parameters considered for the synchronverter model.

| Parameter Name | Parameter Symbol | Value |
|---|---|---|
| Synchronverter permanent droop | $R_d$ | 0.05 p.u./p.u. |
| Virtual inertia constant | $H_V$ | 51.4 ms |
| DC link regulator proportional gain | $k_p$ | 0.496 |
| DC link regulator integral gain | $k_i$ | 0.551 $s^{-1}$ |
| DC link capacitance | $C$ | 18.8 mF |
| DC link capacitance inertia constant | $H_C$ | 51.4 ms |
| DC link resistance | $\bar{R}_{dc}$ | 1230 p.u. |
| Initial back end power | $p_{be}(0)$ | 1.0 p.u. |
| Coupling impedance | $\vec{Z}$ | $0.180\angle 89.3°$ p.u. |
| Base power | $P_{base}$ | 30 kVA |
| Base RMS phase-to-phase voltage | $V_{base}$ | 220 V |
| Base DC link voltage | $v_{dcbase}$ | 405 V |
| Base angular frequency | $\omega_{base}$ | 376.99 rad/s |

**Synchronous machine model**

Analysis of the results obtained from the synchronous machine model confirms the general consensus that higher inertia constants provide greater grid frequency support. A 19.7% load step, which may be regarded also as a 19.7% loss in generation capacity, is applied through the input signal $\Delta p_L(t)$ for inertia constant values from 0.1 s to 10 s. Figure 3.17 shows the effects such an input has on deviations around the pre-disturbance grid frequency $\Delta\omega_g(t)$ and machine output power $\bar{p}_{fe}(t) = \bar{p}_e(t) + \bar{p}_d(t)$ and on the extra energy injected due to the disturbance $E_{dist}(t)$ for different inertia constants $H$. Assuming a unit is connected to a grid, in steady state, and a disturbance happens at $t = 0$, the unit's front end converter power into the grid $\bar{p}_{feg}(t)$ (in per unit system) may deviate from its steady state value $\bar{p}_{feg}(0)$ by $\Delta\bar{p}_{feg}(t) = \bar{p}_{feg}(t) - \bar{p}_{feg}(0)$. The energy injected due to this disturbance is $E_{dist}(t)$, given by equation (3.60). It is measured in time units, like the inertia constant.

$$E_{dist}(t) = \frac{1}{P_{base}} \int_0^t \Delta p_{feg}(\tau) d\tau = \int_0^t \Delta \bar{p}_{feg}(\tau) d\tau \tag{3.60}$$

Damping power $\bar{p}_d(t)$ was neglected in the power that goes into the grid, $\Delta p_{feg}$.

This simulation considers that the machine's rated power is half the system's, with $P_{baseSystem}/P_{base} = 2$. This may be the case if we have a small, isolated EPS, like a microgrid, or if we wish to lump together a large number of similar generating units and study the effects on an EPS. These results clearly show the effects of higher inertia constants on frequency nadir. The correlation between inertia constant and frequency nadir is shown in figure 3.18. The fitted curve indicates a relationship of approximately between frequency nadir and inertia constant of 0.33 Hz/s.

The energy injected due to the disturbance is positive all across the event, for

every value of inertia constant. Its peak value increases with inertia constant.

### 3.4.2 Synchronverter with DC link regulation model

The results from the synchronverter with DC link regulation model show that the virtual inertia chosen to be emulated has a negligible effect on frequency support capability compared with the actual inertia on a synchronous machine. Additionally, they show that DC link regulation parameters have a large impact on frequency support capability, specially the integral gain $k_i$.

Choosing low values for the integral gain in the DC link PI regulator $k_i$ can significantly improve a unit's response to frequency deviation, as measured by $\Delta\omega_g(t)$. Simulations show, through figure 3.19, time responses for $0.0184\ s^{-1} < k_i < 18.4\ s^{-1}$ given the same load-generation disturbance as for the synchronous machine model analysis. For the synchronverter model, another variable is added to the graphs, the DC link voltage variation $\Delta\bar{v}_{dc}(t)$. Lower $k_i$ values allow the DC link voltage to reach lower levels, and extend the time for it to be restored, at the expense of requiring a wider operating band for DC link voltage. That is, injected power is positive for a longer time and the synchronverter apparently gives better support to the grid frequency.

This trend is not true for all the integral gain range shown here. The case with the worst frequency nadir does not correspond to the one with highest integral gain. Injected energy due to disturbance $E_{dist}(t)$ is slightly more complex, as curves for different integral gains cross each other at some points.

It should be noted this is a linear model, that is why it is possible for the DC link voltage to reach values such as $-2$ p.u. This means the real converter, for some of the integral gain values shown, would not tolerate such a disturbance. The lowest integral gains shown would tolerate disturbances approximately 10 times smaller, taking the maximum DC link voltage deviation to approximately 0.2 p.u.

Taking the same disturbance into account, figure 3.20 shows the effects of a varying DC link regulator proportional gain $k_p$ between the values 0.184 and 1.84. Dependence on $k_p$, for the set of parameters being considered, is more complex than that observed for $k_i$. Power oscillations grow larger as $k_p$ decreases. The results in figure 3.20 show that the lowest $k_p$ value does not render the best frequency nadir, but more likely the worst. Peak $E_{dist}$ is the highest for the low values of $k_p$, but its value across the time is important in determining frequency nadir. The more intense power oscillations that happen with lower $k_p$ have their negative peak close to the moment of minimum frequency, extracting power from the grid at the most critical moment.

The former results considered a synchronverter with a virtual inertia constant

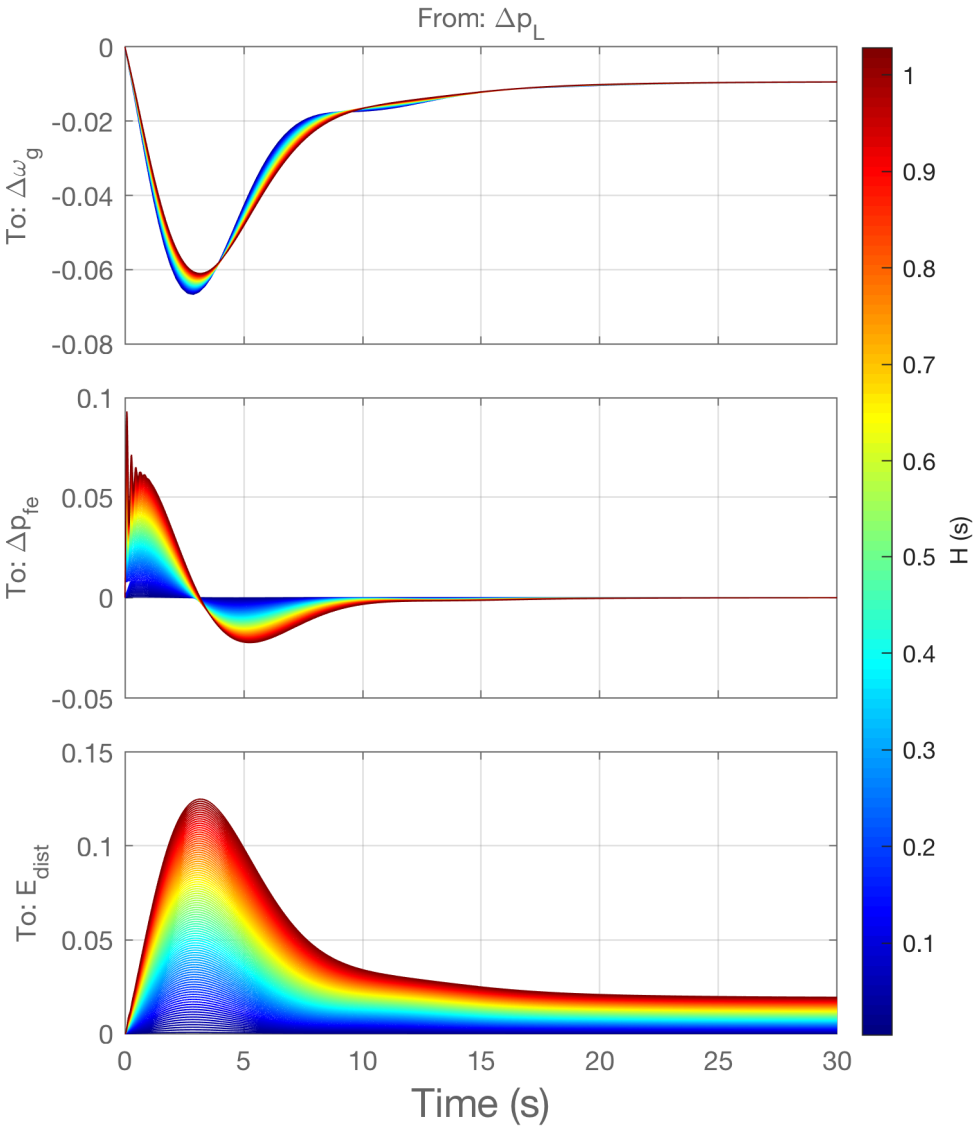


Figure 3.17: Effects of a 19.7% load step on grid frequency $\bar{\omega}_g(t)$, machine output power $\bar{p}_{fe}(t) = \bar{p}_e(t) + \bar{p}_d(t)$, and energy injected due to disturbance $E_{dist}(t)$ considering 100 different values for the inertia constant $H$. The machine's base power is half the EPS's. All variables are in per unit, except for $E_{dist}$ which is measured in seconds.

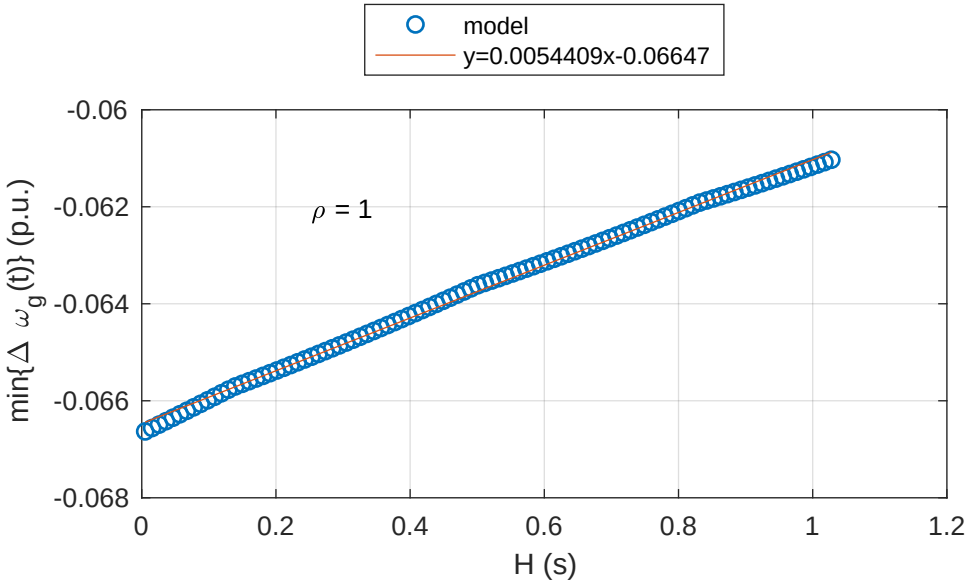


Figure 3.18: Relationship between frequency nadir and a machine's inertia constant $H$.

$H_V$ equal to its DC link inertia $H_C = 51.4$ ms. We may now consider different virtual inertia constants to take advantage of a converter's capacity of emulating a synchronous generator's inertia.

Results show that the virtual inertia chosen for a synchronverter controlling its own DC link has very little effect over its capacity to provide grid frequency support, as measured by $E_{dist}(t)$ and by frequency nadir. It does allow, however, for a larger DC link voltage swing. One may compare figure 3.21 for the synchronverter model with figure 3.17 for the synchronous machine model.

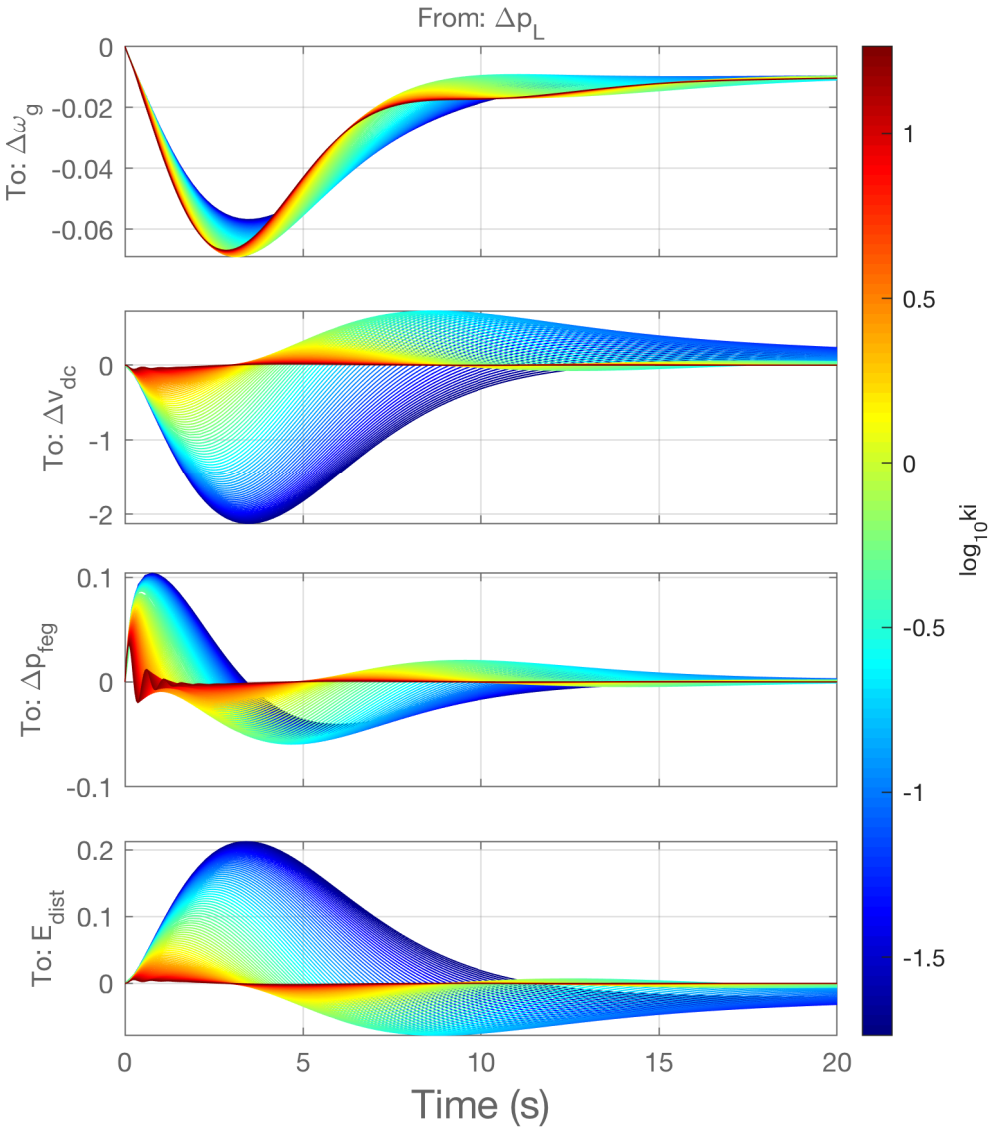


Figure 3.19: Effects of a 19.7% load step on grid frequency $\bar{\omega}_g(t)$, DC link voltage $\bar{v}_{dc}(t)$, synchronverter output power $\bar{p}_{feg}(t)$, and energy injected due to disturbance $E_{dist}(t)$ considering 100 different integral gains $k_i$ for the DC link voltage PI controller. Synchronverter's virtual inertia constant is 51.4 ms and its base power is half the EPS's. All variables are in per unit, except for $E_{dist}$ which is measured in seconds.

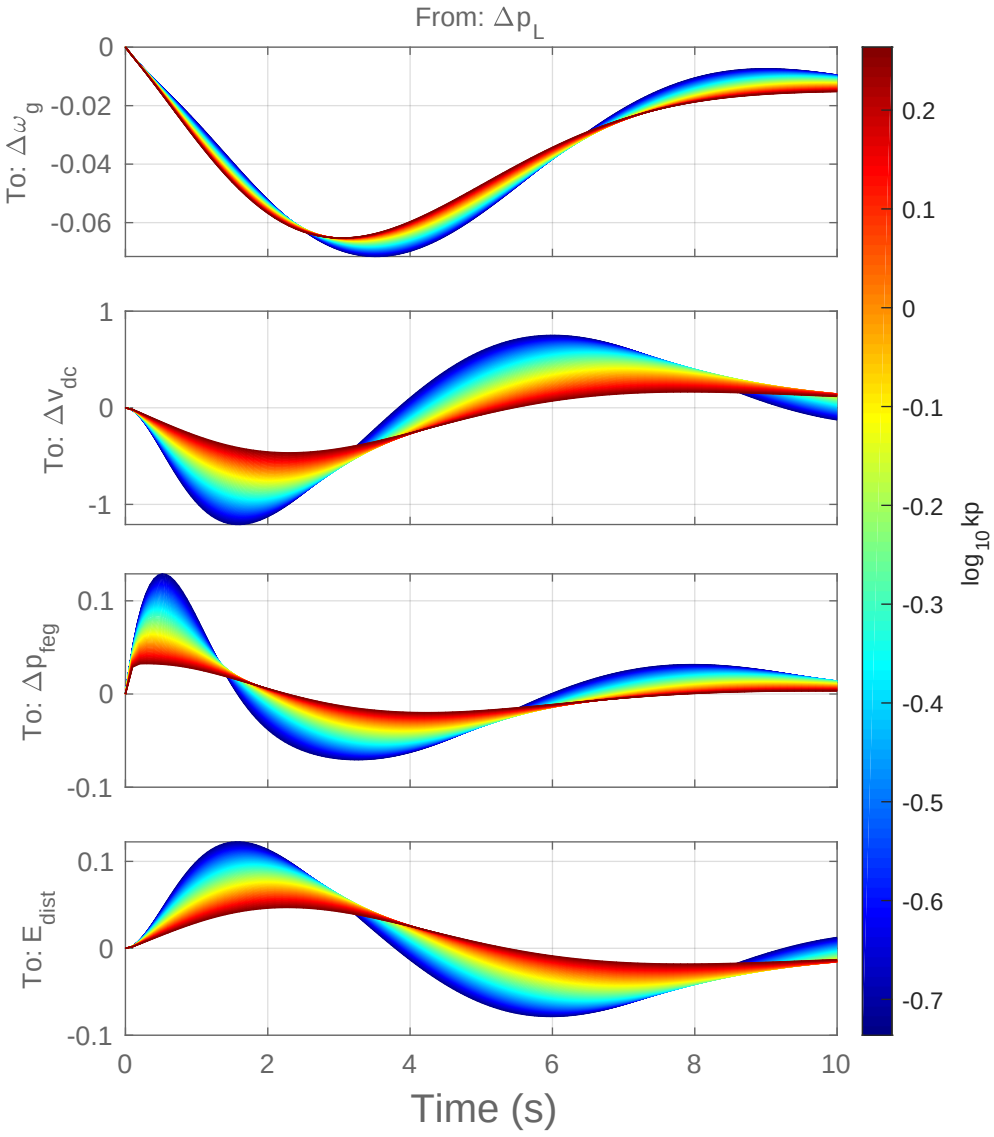


Figure 3.20: Effects of a 19.7% load step on grid frequency $\bar{\omega}_g(t)$, DC link voltage $\bar{v}_{dc}(t)$, synchronverter output power $\bar{p}_{feg}(t)$, and energy injected due to disturbance $E_{dist}(t)$ considering 100 different proportional gains $k_p$ for the DC link voltage PI controller. Synchronverter's virtual inertia constant is 51.4 ms and its base power is half the EPS's. All variables are in per unit, except for $E_{dist}$ which is measured in seconds.

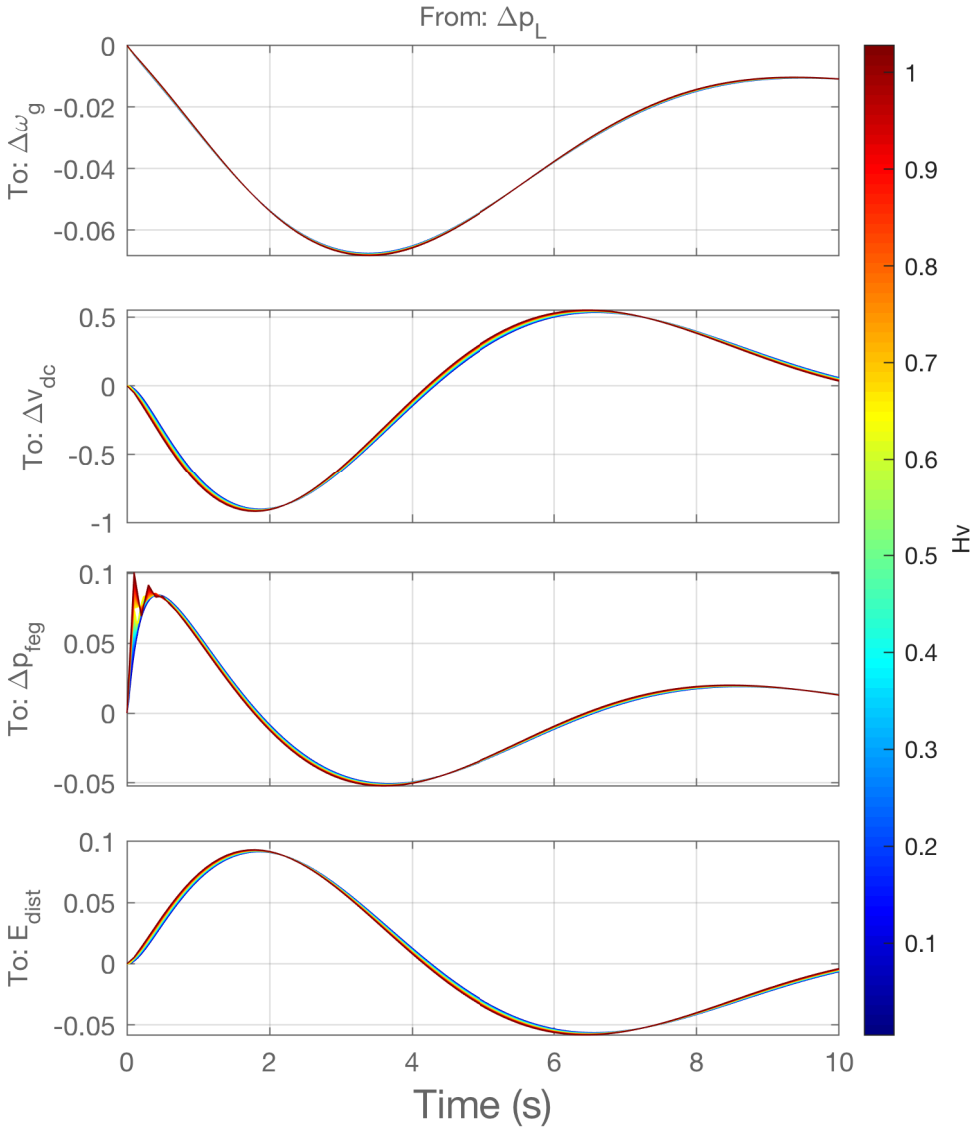


Figure 3.21: Effects of a 19.7% load step on grid frequency $\bar{\omega}_g(t)$, DC link voltage $\bar{v}_{dc}(t)$, synchronverter output power $\bar{p}_{feg}(t)$, and energy injected due to disturbance $E_{dist}(t)$ considering 100 virtual inertia constants $0.1H_C < H_V < 20H_C$. Synchronverter's base power is half the EPS's. All variables are in per unit, except for $E_{dist}$ which is measured in seconds.

# Chapter 4

# Small-signals turbine and governor model response as a metric

One possible measurement of a generating unit's contribution to the system is through simulation of each generating unit connected to a power system and observation of the nadir frequency after a power unbalance. However, is it possible to extend the results found in this way to other power systems? Would we be measuring the response of a particular system and generating unit combination or an intrinsic characteristic of this generating unit, which is what we want? And how would these results depend on the choice for the size of the power system, with respect to the generating unit's power rating? Therefore, we wish to find independence from

- power rating ratio,
- power system model.

Furthermore, how would we measure this response if we didn't have a model for the generating unit, e.g., if one wishes to independently evaluate a generating unit's contribution to frequency stability? In the context of growing use of RES and distributed generation, this is an interesting capability.

An LFC model embedded in a converter's controller might be the answer to these questions. If a back-to-back converter is connected between a generating unit and the grid, it can act as a proxy for a power system, generating, on the generating unit side, three-phase voltages whose frequency is given by the LFC model. The power provided by the generating unit will be fed into the LFC model's power sum, after being multiplied by a gain which will correct for the different base powers. Of course, this approach would limit target generating units with respect to their power ratings. The development and testing of this measurement methodology will be addressed in chapter 5.

## 4.1 Generating unit and turbine and governor model sampling

The model sampling framework was extended through the addition of features that serve the purposes of this study. Figure 4.1 contains a detailed class diagram that shows the framework developed for the analysis of frequency stability contribution. The framework was based on an Object-Oriented Programming philosophy, which makes easier the inclusion of other models in a structured, organized manner.

A class *GeneratingUnitConnectedToTurbineAndGovernor* has two main attributes, a *TurbineAndGovernor* object and a *GeneratingUnit* object. Each of those has its own state-space model. When the model in a *GeneratingUnitConnectedToTurbineAndGovernor* object is sampled, a model array is created with all samples, along with the Boolean matrix that identifies stable samples. The model in either the *TurbineAndGovernor* or the *GeneratingUnit* object is also sampled, depending on which model depends on the parameter being sampled, and has its own stable samples Boolean matrix.

The matrix for stable samples identification, *stableSamplesLogicalIndexingMatrix*, allows for other parts of the analysis to be restricted to stable samples and ignore unstable samples. I.e., for each model generated from a given set of parameters, the resulting closed loop poles are computed and the sample is flagged as unstable if any poles lie in the right-hand side of the complex plane (if $\Re\{p\} > 0$). Each position of this matrix corresponds to a sample, a specific combination of parameter values, and the value in this position will be *true* for a stable sample, and *false* otherwise. This Boolean matrix, which will have as many dimensions as independently sampled variables, is used to perform MATLAB®'s logical indexing, as it selects in matrix $A$ the elements in the positions that are *true*-valued in an indexing matrix $B$. This avoids calculating every model sample's poles for every step of the analysis, storing this information in memory instead, crucial for the feasibility of the proposed analysis, as the number of models rise quickly with the number of parameters analyzed.

An option to disconnect the signal $\Delta p_{feg}(t)$ from the generating unit model to the turbine and governor model was built into *GeneratingUnitConnectedToTurbineAndGovernor*. This is equivalent to having the turbine and governor model's base power be many times larger than the generating unit's, therefore making the ratio $P_{systemBase}/P_{base}$ approach zero. This allows one to analyze a generating unit's response to a grid frequency disturbance when that generating unit's power output has virtually no influence over the grid.


Figure 4.1: Class diagram of the framework developed for analysis of generating unit models' frequency stability contribution.

### 4.1.1 Synchronverter sampling

The base model is the Synchronverter with DC link regulation model developed in section 3.2, using parameters for the experimental setup that will be used in chapter 5, already presented in table 3.4. Sampling this model generates an array of models, each with a different set of parameters.

Within the framework shown in figure 4.1, the synchronverter is a *GeneratingUnit* object, specifically a *SynchronverterWithDcLinkRegulation*, and it is connected to the hydraulic turbine and governor LFC model presented in section 3.1.1, a *TurbineAndGovernor* object, specifically a *HydraulicTurbineAndGovernor*. For the following discussions, a 19.7% load disturbance is considered, for it is the disturbance that causes, in the isolated LFC model considered, a 4 Hz frequency drop, to a 56 Hz frequency nadir, the maximum frequency drop that wind and PV units are required by ONS [36] to not cause a frequency relay trip (for at least 10 s), as shown in figure 2.2.

In an effort to characterize the whole Synchronverter with DC link regulation base model, simultaneous sampling was performed on multiple parameters. The parameters that were chosen to change from one sample to another are:

- capacitor inertia constant $H_C$;
- the virtual inertia constant $H_V$;
- DC link regulator proportional gain $k_p$;
- DC link regulator integral gain $k_i$.

#### Sampling range

This methods begs the question of what sampling range is used for each parameter. How do we determine whether the sampling range is wide enough for our purposes?

For the capacitor inertia constant and the virtual inertia constant, there is some reasoning to apply to the range definition. The virtual inertia constant tries to mimic real machines' inertia constants, so we should use their typical values as a reference. Capacitor inertia constants may be taken from their typical values around $[10^{-2}, 10^{-1}]$ seconds, up to the virtual inertia constant range, in order to compare their effects. Similarly, the virtual inertia constant range may be expanded downwards towards the capacitor inertia constant range.

For parameters that don't offer a clear reference range, one objective method to define it is to determine the region that provides parameter sets which lead to a stable system. A reasonable assumption is that any set of parameters of practical interest will lie within a continuous region of stability in the space of parameter

sets. Additionally, this set of parameters must be able to withstand frequency disturbances without having the DC link voltage be driven outside its operational range.

Figure 4.2 shows a way of mapping this information. The four parameters were sampled at various values:

- capacitor inertia constant $H_C$: 12 values logarithmically spaced in the interval $[0.01, 10]$;
- the virtual inertia constant $H_V$: 12 values logarithmically spaced in the interval $[0.01, 10]$;
- DC link regulator proportional gain $k_p$: 12 values logarithmically spaced in the interval $[0.0316, 100]$;
- DC link regulator integral gain $k_i$: 12 values logarithmically spaced in the interval $[0.01, 316]$.

The combination of those parameter values leads to a total of 20,736 model samples. If one picks all model samples with capacitor inertia constant equal to 0.01 s and counts how many of those comply with chosen requirements, in this case:

- the model sample is stable (has no poles with positive real parts);
- the model sample's DC link voltage does not go outside a predetermined range of $1 \pm 0.2$ p.u. after a reference disturbance;

then one can divide this number by the total number of samples. The result will be the proportion of valid model samples with respect to the total, when $H_C = 0.01$ s. This is the first point for the capacitor inertia constant curve in figure 4.2. It is an approximation to the likelihood of finding a stable set of parameters for a synchronverter that regulates its own DC link, when its capacitor inertia constant equals 0.1 s, that can withstand the proposed grid frequency disturbance. A smaller number of valid parameter sets also mean more difficulty in online controller tuning and higher susceptibility to changes in plant parameters. DC link voltage deviation is evaluated with the signal $\Delta p_{feg}$ disconnected from the LFC model, emulating the generating unit being connected to a much larger system, so that it has virtually no effect over grid frequency.

Plots such as the one in figure 4.2 are known in Machine Learning as Partial Dependence Plots (PDP) [65, 66]. They are used to visually extract information from developed models, which may depend on several variables. PDPs show the mean effect a variable has on a model, a way of isolating this effect from other variables'. Appendix A shows explains, through a simple example, PDP and Individual Conditional Expectation (ICE) plots.

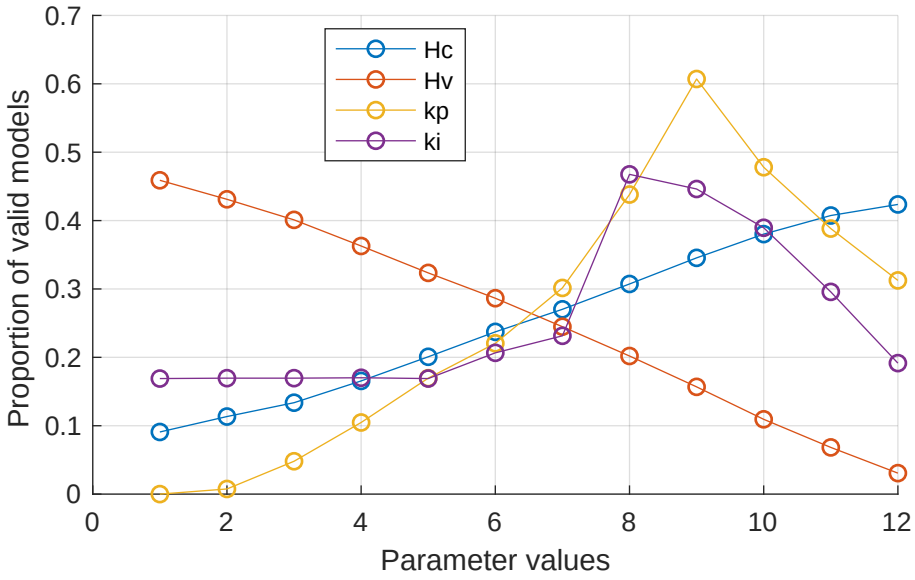


Figure 4.2: Partial dependence of model validity with respect to sampled parameters. Valid samples must be stable and have its DC link voltage deviation be within $\pm 0.2$ p.u. after a disturbance. The horizontal axis is an identifier for the sampled parameter value and may be regarded as a logarithmic scale.

The proportional gain curve in figure 4.2 tells us it is likely not worth it to expand its range downwards. Part of this sharp decline, and much of the integral gain curve's decline towards lower values as well, is due to the increasing likelihood of failing to keep the DC link voltage within bounds for lower proportional and integral gains. Another part is due simply to the proportional gain increasing the number of stable systems, as can be noticed in figure 4.3, which only takes into account the stable model sample restriction.

More information comes from analyzing parameter pairs' joint effect on valid samples. This is done in the form of a plot matrix, with redundant plots omitted, in figure 4.4. The plot that relates virtual and capacitor inertia constants has a clear, interesting feature. For virtual inertia constants lower than the capacitor's, the model's validity is, on average, independent of the relationship between virtual and capacitor inertia constants. However, there's a sharp drop in valid samples above the $H_V = H_C$ line, when virtual inertia constant is larger than capacitor inertia constant.

The plots involving either one of DC link controller gains show other sharp features, lines related to minimum values for fulfilment of the DC link voltage deviation requirement. The plot relating both DC link controller gains clearly shows the region of low values that do not fulfill this requirement and an upper line which marks

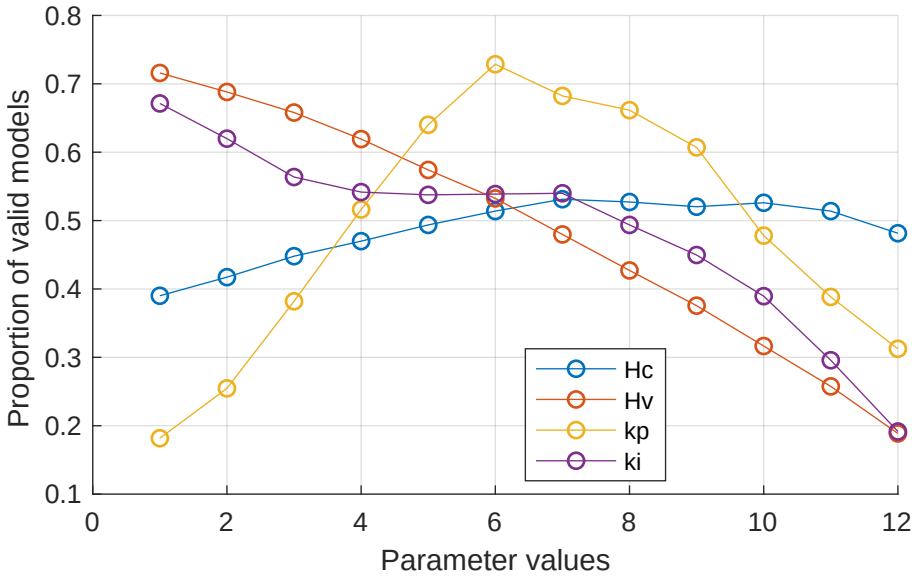


Figure 4.3: Partial dependence of model validity with respect to sampled parameters. Valid samples are only required to be stable. The horizontal axis is an identifier for the sampled parameter value and may be regarded as a logarithmic scale.

the region for which the integral gain is too high and leads to instability. The ranges for DC link controller gains were deemed adequate for this analysis given that both figures 4.2 and 4.4 indicate shrinking valid samples parameter regions for higher integral and proportional gains.

### 4.1.2 Model sampling limitations

These data were obtained through regular sampling of controller parameters and combining sampled values, forming a collection of parameter sets, the model samples. Each parameter set has a different likelihood of occurring in real world controllers. In controller design, parameter sets are not taken at random, but are tailored to fulfill design criteria. Therefore, a better understanding of the characteristics these controllers possess in real world applications might come from restricting or weighing model samples according to the likelihood with which it might be found in real world applications.

## 4.2 Dependence on turbine and governor model

A grid frequency stability contribution metric is ideally independent from the system to which the generating unit being inspected is connected. That is, when one speaks

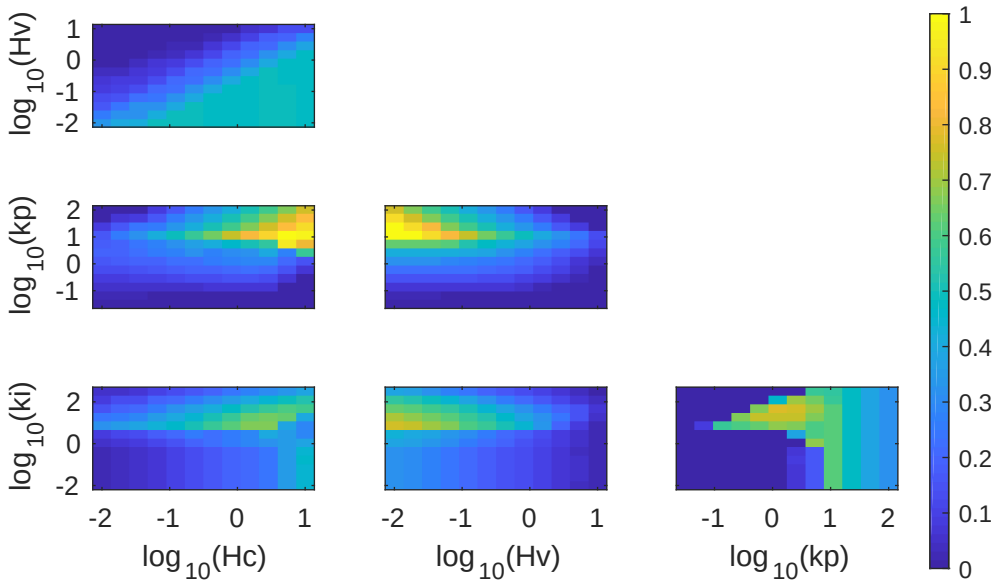


Figure 4.4: Proportion of valid DC link regulating synchronverter model samples for given pair combinations of sampled parameters. Valid samples must be stable and have its DC link voltage be within bounds after a disturbance.

about a synchronous machine with a higher inertia constant having a greater contribution to the system's frequency stability, one does not specify to which type of system (e.g.: hydraulic plants based, with which parameters, etc.) this synchronous machine is connected. There's a hidden assumption in this reasoning that the generating unit's contribution to frequency stability is the same for every system to which it is connected. The proposed metrics must be tested for such independence.

One could go even further and ask whether the contribution to frequency stability itself is system independent. If it is, then generating units which fare well when connected to one system will do so for every system.

### 4.2.1 Generation kind

This assumption was tested under the models developed for a generating unit connected to a power system with primary speed control through turbine and governor models and load damping. Three reference turbine and governor models were used, one for a hydraulic plant, shown in section 3.1.1, one for a steam plant with reheat and another for a steam plant without reheat, presented in section 3.1.2, with the presented typical parameters.

Figure 4.6 shows that the same generating unit might present different frequency stability support depending on the system to which it is connected. It plots frequency

nadir difference for a given step load increase for several sample generating units connected either to the Hydraulic, Steam, or the Steam with no Reheat turbine and governor models on one axis and frequency nadir difference for that generating unit connected to another turbine and governor model on the other axis. I.e., each point in the graph corresponds to one generating unit sample, and that point's coordinates are given by the frequency nadir differences obtained for a reference load step applied to two LFC models when connected to that generating unit sample.

Frequency nadir difference is the difference between the frequency nadir of each case and the frequency nadir obtained if no generating unit is connected to the turbine and governor model (or if the turbine and governor model's base power is many times greater than the generating unit's), as shown in figure 4.5. I.e., a positive frequency nadir difference means a contribution towards a better frequency stability, and a negative frequency nadir difference means a degradation in frequency stability. A normalized frequency nadir difference may also be calculated dividing the frequency nadir difference by the isolated system's frequency nadir.

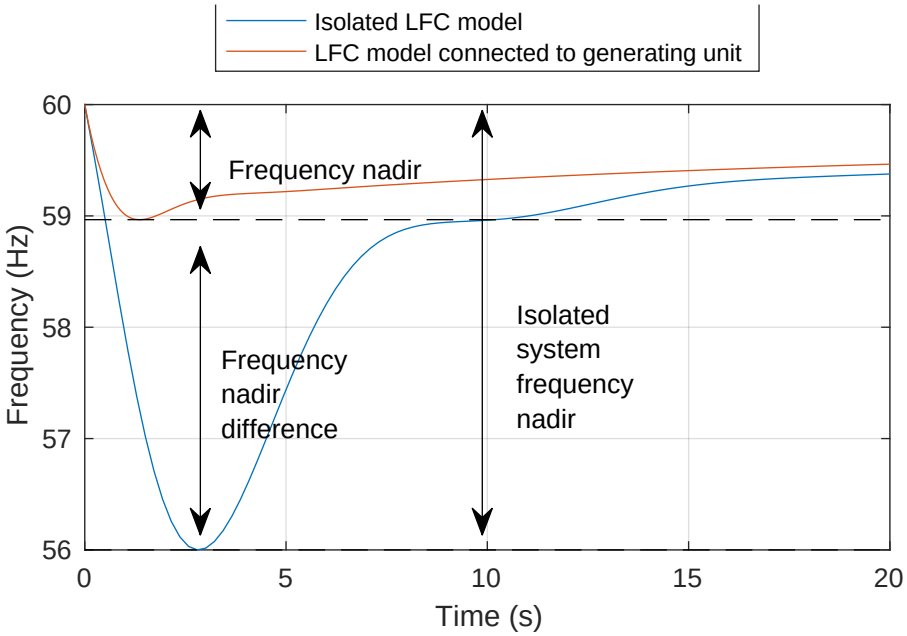


Figure 4.5: Quantification of a generating unit's contribution to frequency stability through comparison with isolated LFC model's response to a load step.

These plots show that, although there is variability in the generating units' performance, there is high correlation between the performance measured when connected to different turbine and governor models. The number $\rho$ presented in each plot is Pearson's correlation coefficient for the points defined by each pair of models, rounded off to two significant figures. It may be regarded as the quality of a least-squares fit by a straight line, a proportional relationship between the two

variables, with possible values in the range $[-1, 1]$, where its sign indicates the sign of the fitted line's slope. Therefore, the response of the generating unit when connected to one of these models is a good approximation to its behavior when connected to other turbine and governor models.

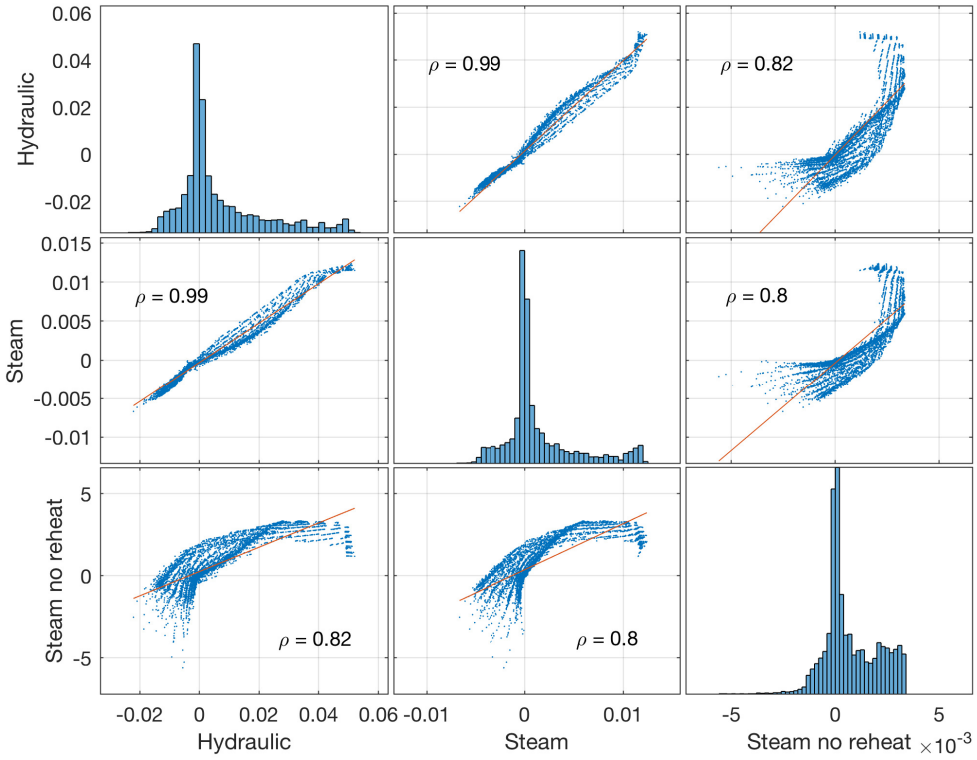


Figure 4.6: Frequency nadir difference for samples of a synchronverter generating unit with DC link regulation, when connected to different turbine and governor models. Each axis represents frequency nadir when a sample is connected to a given turbine and governor model. The red line is a linear fit with correlation coefficient $\rho$.

Another test for the dependence of frequency stability support on the turbine and governor model is to investigate whether generating unit samples fare differently relative to each other when connected to different turbine and governor models. If frequency stability support is exclusively a generating unit characteristic, rather than dependent on the system to which it is connected, then they must rank equally when its frequency stability support is measured against different LFC models.

For each pair of turbine and governor LFC model, the following procedure is performed:

- calculate frequency nadir for every generating unit sample when connected to one LFC model, sort them according to frequency nadir and label them by their ranking position;

- repeat calculation for a second LFC model, sort generating unit samples according to frequency nadir and identify each sample using the label from the first step.

This will provide with two vectors for each pair of LFC models. The first vector will simply be a sequence from 1 through $N$, the number of generating unit samples considered. The numbers in this vector will be identifiers for each generating unit sample. I.e., the sample which has the best frequency nadir when connected to the hydropower plant model will be sample 1, the worst will be sample $N$. The second vector will be associated with the steam model. It will also be ordered according to how well each generating unit sample supported the system frequency, each generating unit sample identified by the reference numbers set by the first vector.

After following this procedure, if one plots one vector against the other, then one finds as presented in figure 4.7. The dashed, black line is the line $y = x$. It indicates where the points were expected to fall if every generating unit sample performed equally with respect to the others, no matter to which turbine and governor model it was connected. The red line is a linear fit to the data, with correlation coefficient $\rho$ indicated inside each plot.

When comparing Hydraulic and Steam plants, 80% of generating unit samples changed ranking positions by a number smaller than 2.2% of the total number of samples. For the Steam no Reheat×Hydraulic comparison, 80% of generating unit samples stayed within 12.7% of its original ranking position. For the Steam no Reheat×Steam comparison, that number was of 13.5%.

### 4.2.2 Turbine and governor size relative to the generating unit

The second aspect we may analyze about the results' dependence on the LFC model is the system's size, in terms of base power, relative to the generating unit's base power. The same arguments and plots from section 4.2.1 are repeated here comparing model samples' frequency nadir performance when connected to hydropower plant LFCs of base powers 2, 10 and 50 times larger than their own.

Figure 4.8 plots frequency nadir values under one system against frequency nadir values under the other. This is an indication that the performance of a generating unit, measured as contribution to alleviate frequency nadir, may be measured or calculated considering a relatively small power system and extrapolated to its contribution to a larger system's frequency stability. This is interesting to note for the development of the measurement methodology. Smaller base power ratios increase the potential impact the generating unit may have in frequency nadir, as is expected

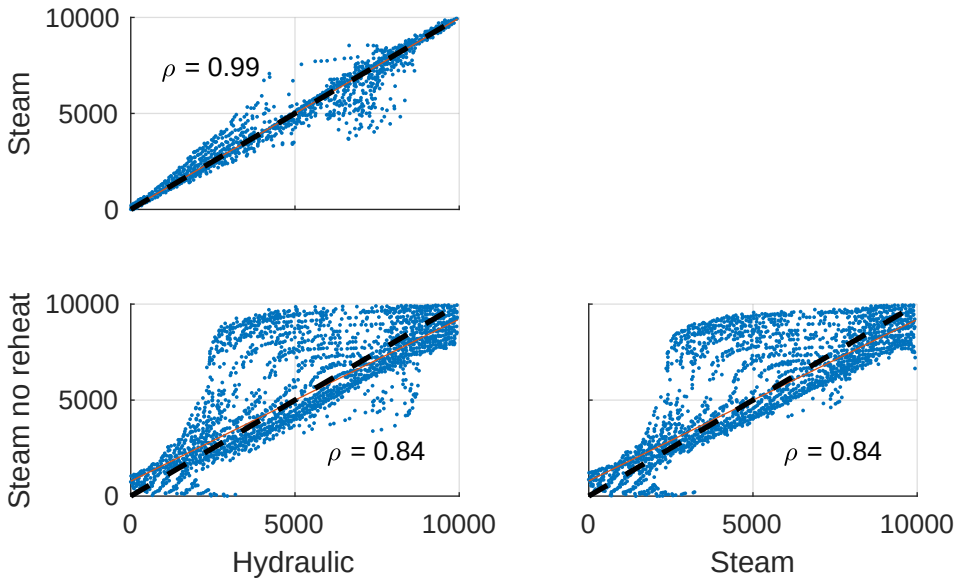


Figure 4.7: Frequency support capability ranking relationship between different turbine and governor models for a ratio between generating unit and turbine base powers of 2.

and may be observed in frequency nadir values in figure 4.8. This makes differences between generating units' contribution to frequency stability easier to measure when testing real converters.

Figure 4.9 compares model samples rankings for different system sizes. The majority of samples is very close to the identity line $y = x$. When comparing systems of base powers 10 and 2 times larger than the generating unit's, 80% of generating unit samples changed ranking positions by a number smaller than 3.7% of the total number of samples. For the $50 \times 2$ base power ratio comparison, 80% of generating unit samples stayed within 6.1% of its original ranking position. For the $50 \times 10$ base power ratio comparison, that number was of 2.9%.

## 4.3 Parameter dependence

Through model sampling it is possible to study the contribution to frequency stability's dependence on controller parameters. Such contribution is a function of the controller's parameters in ways not always tractable analytically. Model sampling becomes computationally demanding as the number of parameters increases, but it can provide useful insights and information.

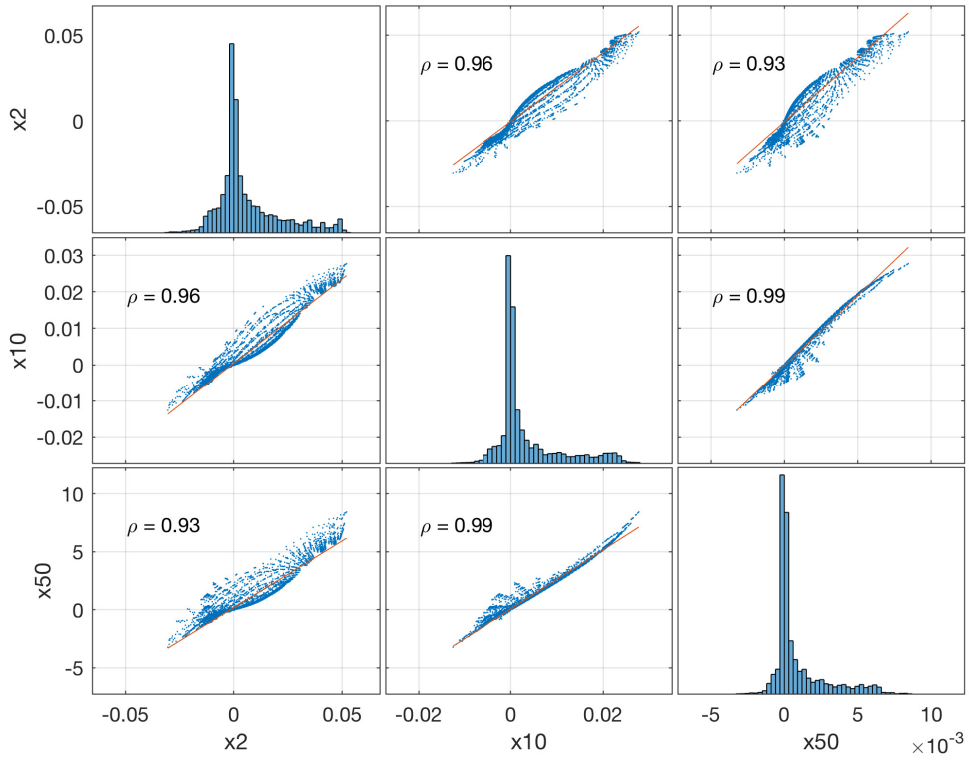


Figure 4.8: Frequency nadir difference for samples of a synchronverter generating unit with DC link regulation, when connected to turbine and governor models of power bases 2, 10 and 50 times that of the synchronverter. Each axis represents frequency nadir difference when a sample is connected to a given turbine and governor model. The red line is a linear fit with correlation coefficient $\rho$.

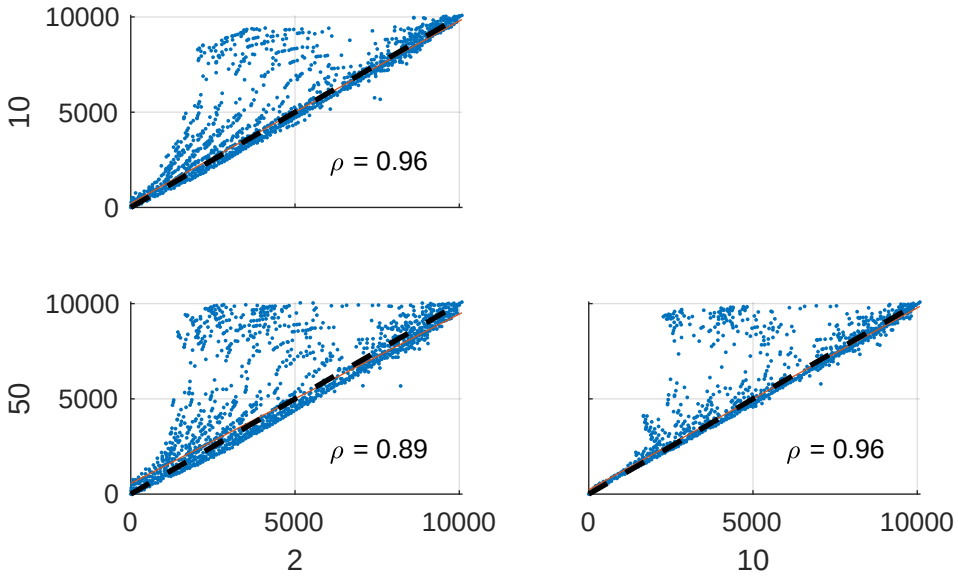


Figure 4.9: Frequency support capability ranking relationship between hydropower plant LFC models with different base power ratios with respect to the generating unit's base power.

### 4.3.1 Synchronverter with DC link regulation

In the following plots, frequency nadir difference with respect to the isolated system will be used to compare performance. For a given sampled value of one parameter, frequency nadir difference after a power disturbance test is averaged across all stable samples with that value for that parameter. E.g., to plot the point for the first sampled capacitor inertia constant in figure 4.10, $H_C = 0.1$ s, all stable samples with $H_C = 0.1$ s were simulated for a step on system load and the y-axis value for that point is the average of the frequency nadir observed in all those simulations. These are PDPs for frequency nadir difference, with respect to generating unit parameters. PDPs are exemplified in Appendix A.

Two-dimensional versions of this plot were made to analyze the joint effect pairs of variables have on frequency nadir. One aspect that is lost on the one-dimensional plots like the one in figure 4.10 is what happens in the lower end of the proportional gain range, for high values of capacitor inertia constant, as show in figure 4.11, where white regions mean no stable samples existed for those parameter values combinations. Virtual inertia constant increased, for this sampled parameters, on average, frequency nadir difference, as shown in figure 4.10. However, figure 4.11 shows a combined increase in integral gain has the opposite effect, leading to negative contributions to frequency nadir. A combination of low integral gain and high capacitor inertia leads to higher contributions to frequency nadir. As mentioned

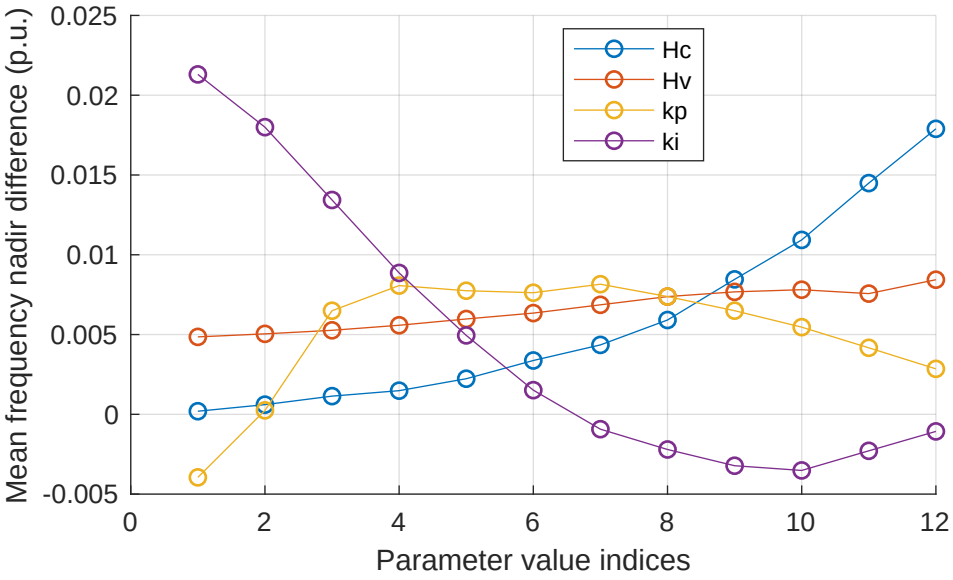


Figure 4.10: Mean frequency nadir difference for the synchronverter that regulates its DC link voltage. The horizontal axis is an identifier for the sampled parameter value and may be regarded as a logarithmic scale.

before, there is a line in the $\log_{10} k_i \times \log_{10} k_p$ relationship above which all samples are unstable.

PDPs capture the average effect of one parameter for a range of combinations of the remaining parameters. Being an average, it may obfuscate differences in trends for different sets of the remaining parameters. For example, one might ask whether higher virtual inertia leads to better frequency support for some combination of the remaining parameters.

Figure 4.12 provides greater detail to the relationship between a DC link regulating synchronverter's parameters and frequency support during a power imbalance. A box plot graphically represents a population of values through its quartiles, values that split the sorted population in four partitions with equal numbers of elements, and extreme values. The red lines represent medians, the box edges represent $25^{th}$ and $75^{th}$ percentiles and the extreme lines represent maximum and minimum values. Each graph is a box plot of the samples' frequency nadir differences for each parameter's set of sampled values.

These plots provide more information than PDPs, showing the complete range of possible frequency nadir difference, given the sampled parameter values, for each value considered for the parameter under study. It enables one to answer the question above: there are indeed sets of parameters for which a synchronverter with DC link regulation with high virtual inertia constant presents relatively high contribu-

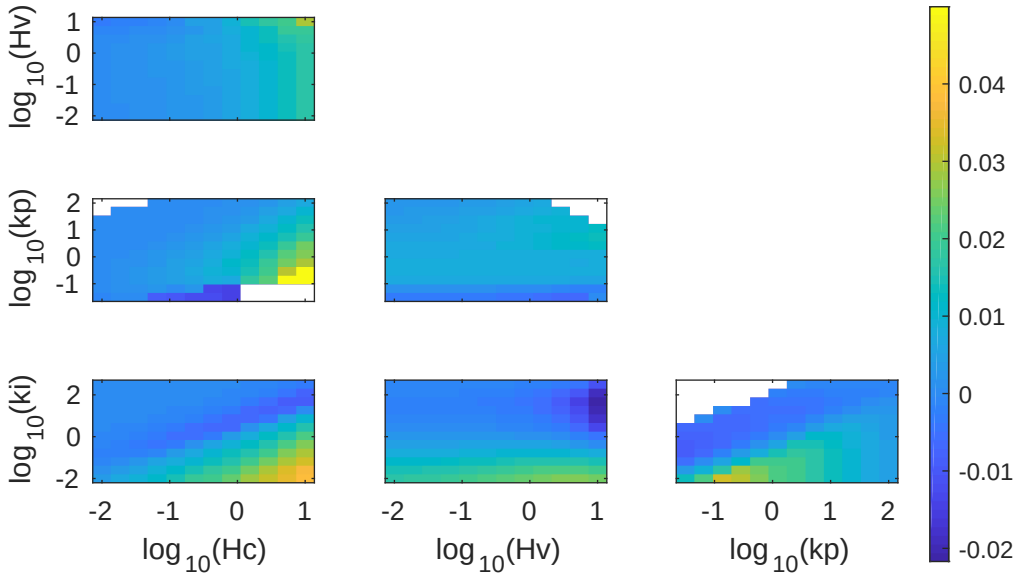


Figure 4.11: Plot matrix showing averaged effect of parameter pairs on frequency nadir difference (p.u.). Regions in white presented no stable samples.

tion to frequency nadir.

Increasing capacitor inertia constant leads to higher upper limits of possible frequency nadir differences, with little change to lower limit, but with an overall shift in the distribution to higher values, as observed from the median and $75^{th}$ percentile. Proportional gain seems to have a positive effect on frequency nadir in its lower range, but a negative effect for the upper part of its range of values. Possible frequency nadir differences' upper limit is nearly unchanged by virtual inertia constant, across the considered range of values. Their lower limit decreases with increasing virtual inertia constant and the distribution seems to widen, as the $75^{th}$ percentile increases and the $25^{th}$ percentile decreases. For an increasing integral gain, both upper and lower limits tend to decrease, as well as the quartiles, with saturation occurring around the logarithmic middle of the considered integral gain range. Frequency nadir difference values concentrate around zero for high proportional and integral gains. This is expected, as higher gains for the DC link controller mean smaller DC link voltage excursions will be possible, meaning there will be smaller power flow variations through the front-end converter and, therefore, smaller contributions to frequency stability.

There is still information that may be lost in the plots shown in figure 4.12, which represent sets of values through five of the population percentiles: 0%, 25%, 50%, 75% and 100%. A slight variation of the previous question would remain unanswered: are there sets of parameters for which increasing virtual inertia leads

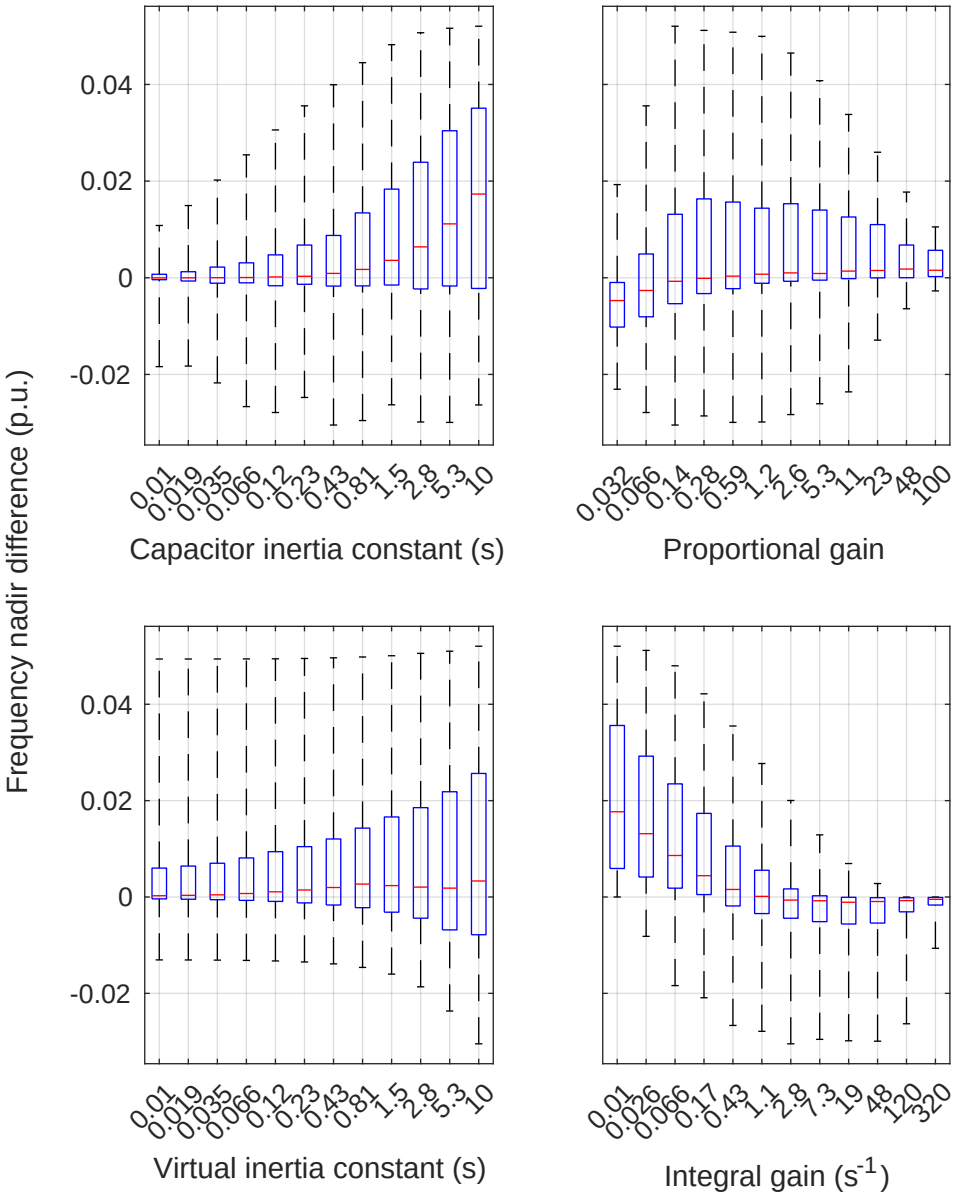


Figure 4.12: Frequency nadir differences (with respect to the isolated system) obtained for all stable parameter sets evaluated for the synchronverter that regulates its DC link.

to better frequency nadir?

ICE plots break down PDPs into several curves, revealing more information [67]. In ICE plots, an individual curve exists for every set of parameters, not counting the parameter under study. I.e., given a function $f(x, \vec{y})$, where $x$ is the parameter under study and $\vec{y}$ is a vector containing the remaining parameters, each curve in an ICE plot is $f(x, \vec{y}_i)$, for $i = 1, 2, 3, ..., N$, where $N$ is the number of considered combinations of the remaining parameters. Appendix A gives a simple example of an ICE plot and its relationship to PDPs.

ICE plots for the considered parameters for a synchronverter with DC link regulation are shown in figure 4.13 with superimposed PDPs. Loose lines, which don't begin and end at the extremes of the $x$ axis, are associated with sets of parameters which don't result in stable models for all the parameter under study's sampled values.

The proportional gain plot shows the apparent positive correlation between proportional gain and frequency nadir difference in the lower proportional gain range is not an actual sensitivity of frequency nadir with respect to proportional gain. Rather, it is an effect of parameter sets becoming stable due to a higher proportional gain, as may be noted from the curves that begin to the right of the PDP's first point. As these parameter sets with higher frequency nadir difference become stable, they increase average frequency nadir difference, represented by the PDP.

Capacitor inertia constant has a positive correlation with frequency nadir difference for many of the presented curves, driving PDP upwards. There are parameter sets, however, that present a decreasing frequency nadir difference for an increasing capacitor inertia constant. A large capacitor inertia constant is therefore not a guarantee of good contribution to frequency stability.

Increasing integral gain tends to decrease frequency nadir difference, as expected, for the lower part of the considered values range. However, the upper range shows frequency nadir difference increasing with integral gain, showing the expected behavior of negative correlation between frequency nadir difference and integral gain is not necessarily true and depends on parameter set and the integral gain itself.

Virtual inertia constant is shown to have negligible impact on frequency nadir for the lower portion of the sampled range and mostly a negative effect for the upper portion. This plot answers the previous question: for the vast majority of parameter sets, virtual inertia constant has little effect on frequency nadir, with most curves in its ICE plot remaining constant for the better part of the sampled range.

Finally, ICE plots can also be presented after offsetting all curves so they all share a common starting point (other points in the curve may also be chosen as the common point). These centered ICE plots have each curve display the change in output with respect to the output for the first sampled value for the variable

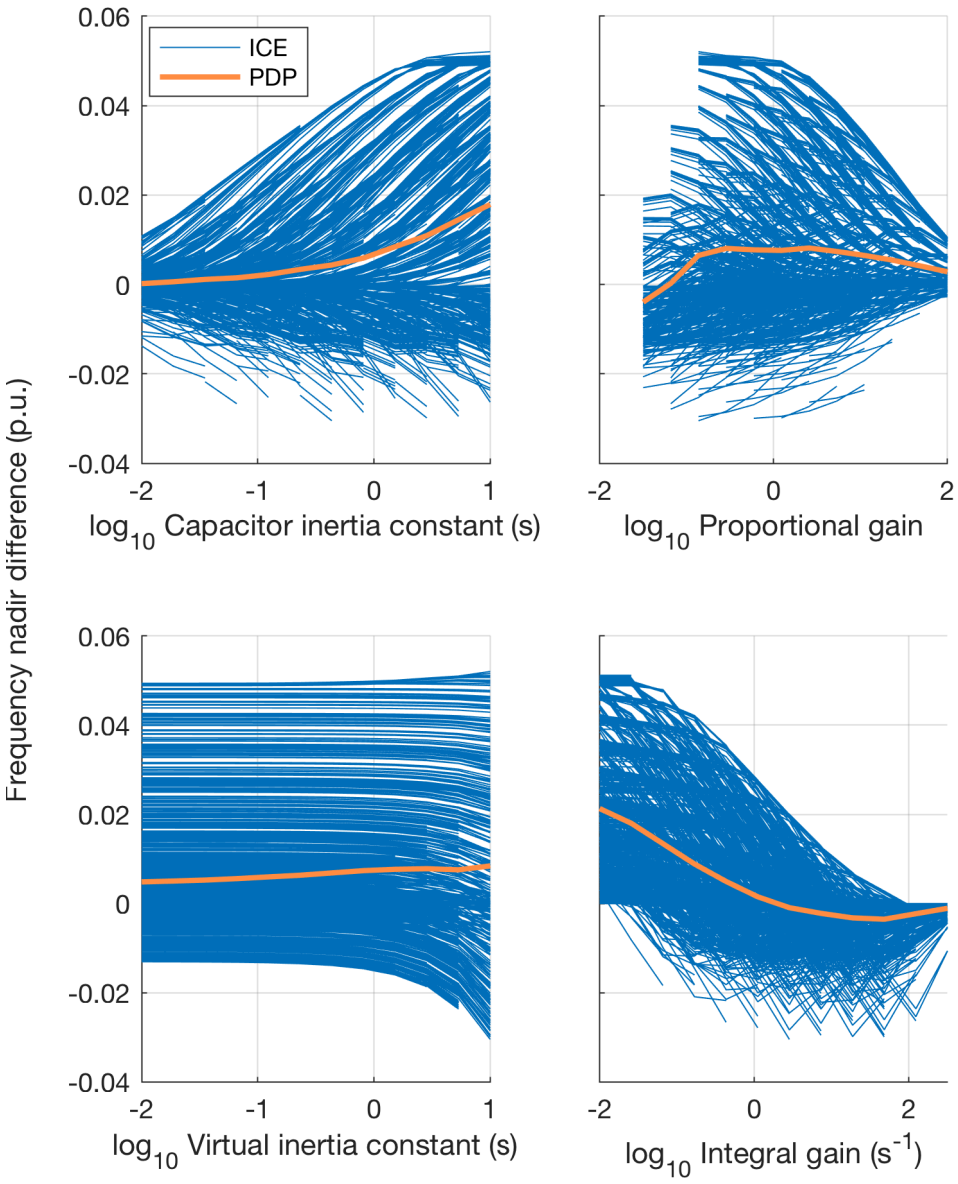


Figure 4.13: Individual Conditional Expectation (ICE) plots for frequency nadir differences (with respect to the isolated system) with superimposed PDP. Results obtained for all stable parameter sets evaluated for the synchronverter that regulates its DC link.

under study. These help highlight the effect the variable under study has on the output, making it easier to compare curves associated with different parameter sets, as shown in figure 4.14.

This effect is notable in the virtual inertia constant centered ICE plot, which shows more clearly that the virtual inertia constant's effect on frequency nadir difference is not as intended for a synchronverter, if it is required to regulate its own DC link voltage. The plots for the remaining variables allow for similar interpretations as the non centered ICE plots, since those tend to converge either on the lower or the upper end of the sampled ranges.

### DC link voltage deviation limit

Observations made so far have considered the developed linear system model for the synchronverter which regulates its own DC link, even though the reference disturbance used caused a 4 Hz deviation from base frequency when no contribution to frequency stability is provided. Some of the parameter sets considered are not be viable if the converter is required to remain connected during such a disturbance, as the resulting disturbance in DC link voltage may be too big. If parameter sets that cause a DC link swing greater than 20% are eliminated from consideration, then its PDPs are as shown in figure 4.15. Distinguishing features from those presented in figure 4.10 include flattening of the integral gain curve in its lower range, the sine-like curve for proportional gain and downwards trend in the virtual inertia constant upper range.

The importance of the capacitor inertia constant is now highlighted through a curve that quickly grows along its upper range of values. Combinations of parameters that allowed for better frequency nadir differences did so compromising DC link voltage, letting it suffer large deviations. If these are no longer allowed, then parameter sets with low capacitor inertia constant are unable to provide frequency support.

This does not mean other parameters no longer have influence over frequency nadir. Indeed, PDPs in figure 4.15 show interesting curves for different parameters. Other plots are more useful, however, to understand their meanings.

Box plots in figure 4.16 support the previous comments on capacitor inertia constant. As capacitor inertia constant decreases, so does the range of possible frequency nadir differences. Other parameters might show wide ranges, reaching high values of frequency nadir difference, but these correspond to parameter sets with high capacitor inertia constant.

The box plot for virtual inertia constant is similar to that shown in figure 4.12, but with a shift in distributions toward lower frequency nadir differences for higher virtual inertia constants.

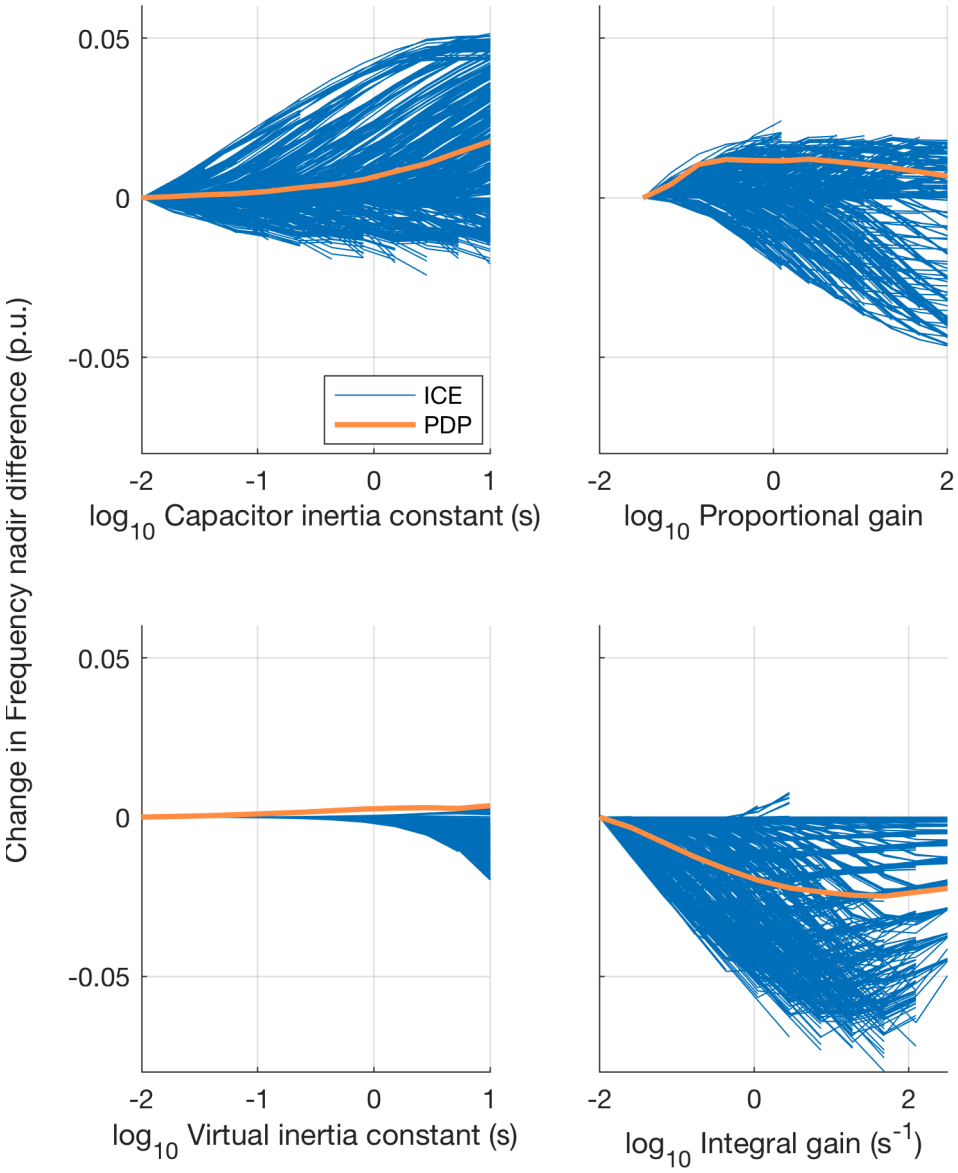


Figure 4.14: Individual Conditional Expectation (ICE) centered plots for frequency nadir differences (with respect to the isolated system) with superimposed PDP. Results obtained for all stable parameter sets evaluated for the synchronverter that regulates its DC link.

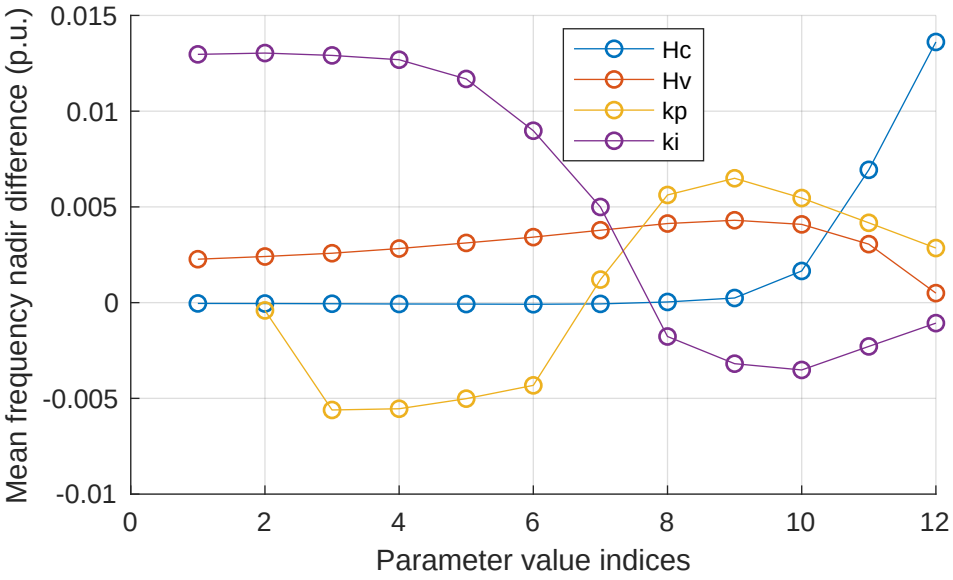


Figure 4.15: Mean frequency nadir difference for the synchronverter that regulates its DC link voltage, considering only parameter sets which were stable and could regulate DC link voltage with ±0.2 p.u. The horizontal axis is an identifier for the sampled parameter value and may be regarded as a logarithmic scale.

Parameter sets with low proportional gain values and high frequency nadir differences were eliminated, as they caused high DC link voltage swings. The only positive frequency nadir difference cases with $k_p < 2.6$ were associated with low integral gains and high DC link voltage deviations.

Parameter sets that caused below zero frequency nadir difference with integral gain in its lower range were mostly eliminated by the DC link voltage restriction. These parameter sets also had low capacitor inertia constant (0.81 s and below) and low proportional gain (below 2.6), leading to large DC link voltage deviations.

Figure 4.17 presents non centered ICE plots after applying the DC link voltage restriction. The proportional gain PDP is again shown to have its most prominent features, a downwards swing in the lower range and an upwards swing in the upper range, be an effect of parameter sets becoming stable as proportional gain varies, rather than sensitivity of frequency nadir difference to proportional gain.

### 4.3.2 Synchronverter without DC link regulation

If instead we consider that the synchronverter does not need to control its DC link voltage, then the synchronverter is allowed to behave as intended, closer to emulating a synchronous machine whose inertia constant equals its virtual inertia constant. Another difference remains on the damping torque loop. On a synchronous

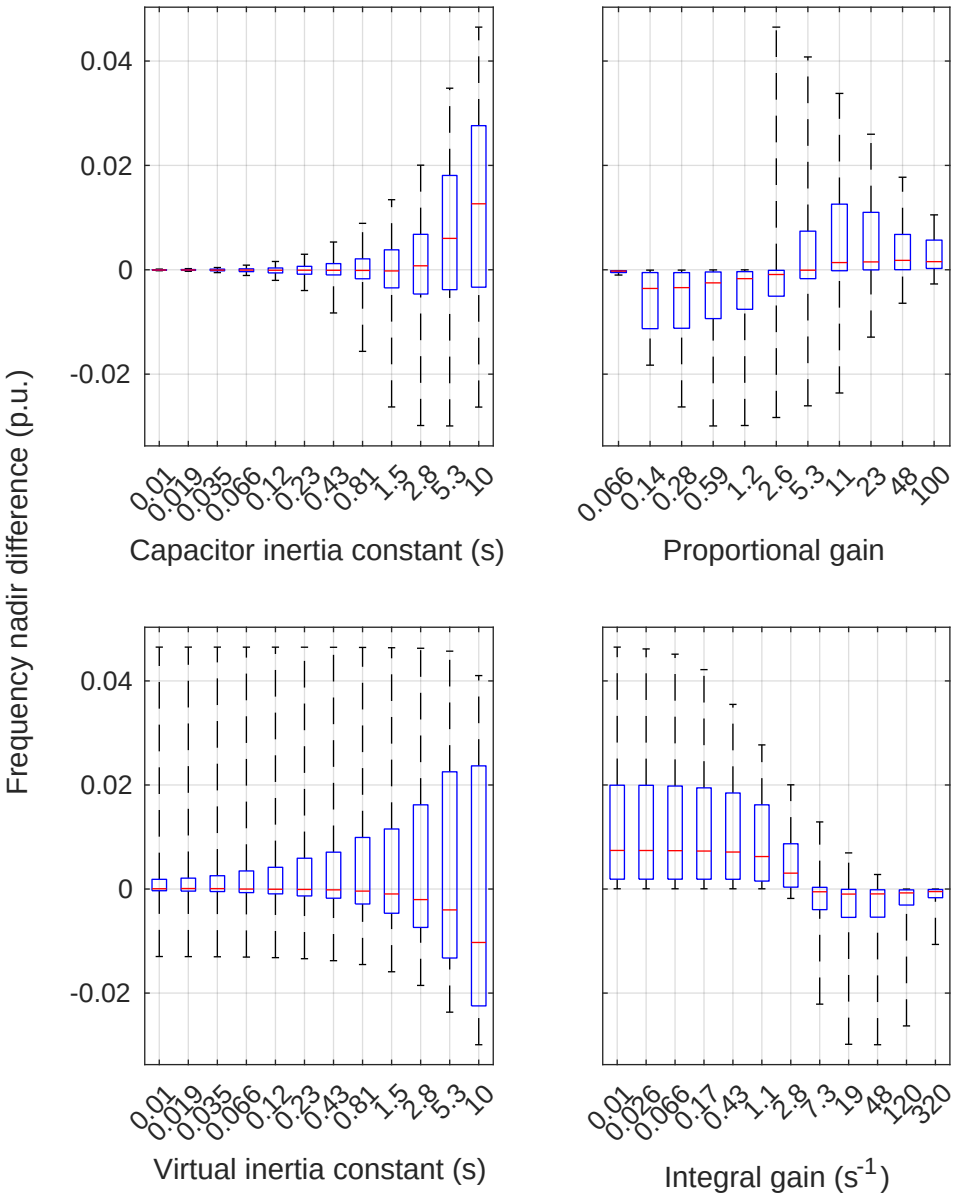


Figure 4.16: Frequency nadir differences (with respect to the isolated system) obtained for all stable parameter sets which could regulate DC link voltage with ±0.2 p.u. evaluated for the synchronverter that regulates its DC link.

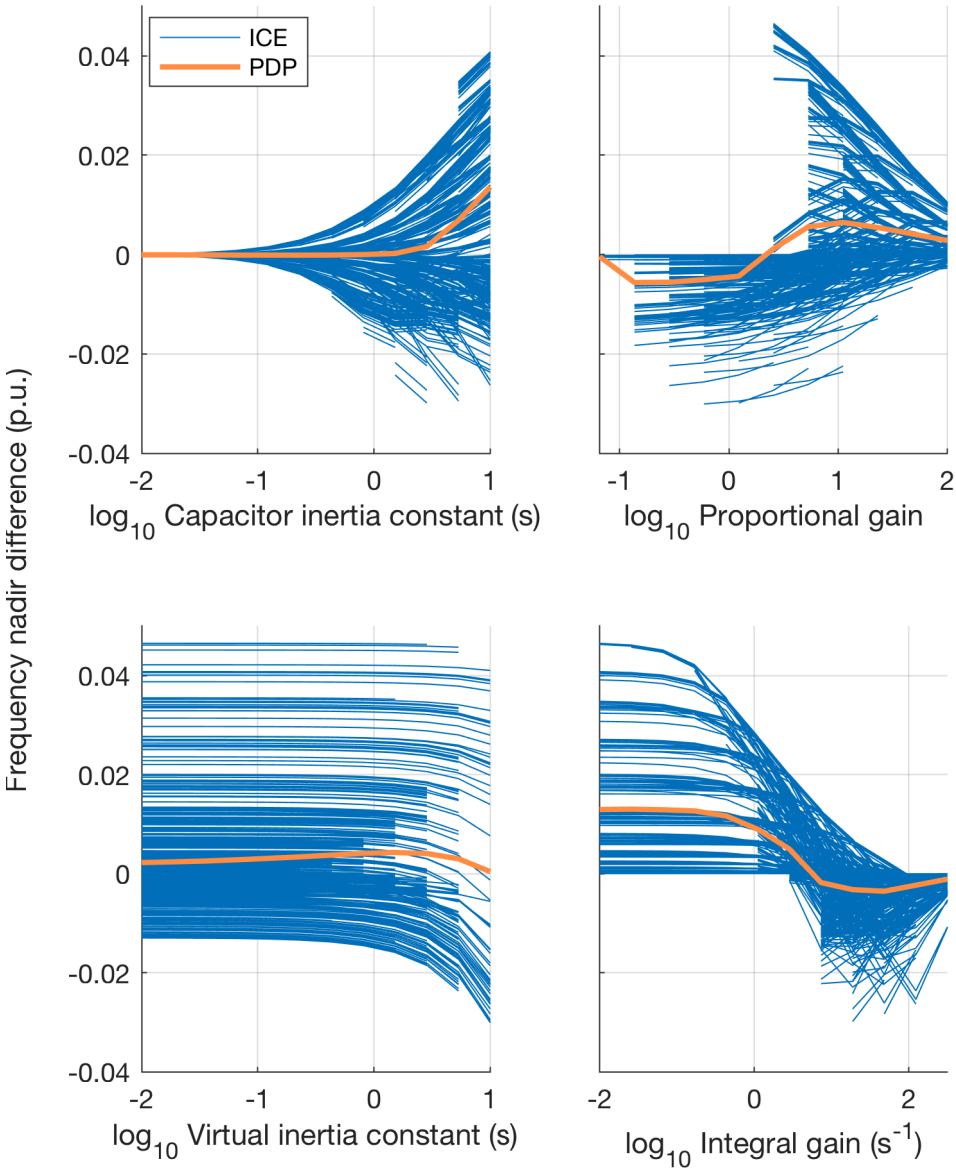


Figure 4.17: Individual Conditional Expectation (ICE) plots for frequency nadir differences (with respect to the isolated system) with superimposed PDP. Results obtained for all stable parameter sets able to keep DC link voltage within bounds, evaluated for the synchronverter that regulates its DC link.

machine, the damping torque is proportional to the rotor speed deviation from the grid frequency, the rotor slip [63, 64], and the torque that is proportional to the rotor speed deviation from a reference speed is the mechanical torque, controlled by a governor. On a synchronverter, there is only a torque proportional to the virtual rotor speed deviation from rated frequency, similar to a governor control action, but with no governor nor any actuator dynamics.

### Back-end power dynamics

If a converter is being controlled as a synchronverter that does not control its own DC link voltage, then there must be another mechanism to regulate it. As mentioned in section 3.2.3, here I'll consider the case that has a back-end converter in charge of DC link voltage regulation, while the front-end is controlled as a synchronverter.

Let's consider sampling on the same parameters as in the case of a synchronverter regulating its own DC link: virtual inertia constant, capacitor inertia constant, and proportional and integral gains for the DC link controller; and on the time constant for the back-end power transfer function $G_{be}(s) = \Delta\bar{P}_{be}/\Delta\bar{P}_{be,ref} = 1/(T_{be}s + 1)$. I.e., the back-end converter's response to the power reference coming from the DC link controller will be approximated by a first-order, low-pass filter of time constant $T_{be}$.

The sampling intervals remain the same, but only 8 sampling points were used for the previous parameters, while 4 sampling points were used for $T_{be}$, logarithmically spaced in the interval $[0.01, 10]$. The lower end of this interval corresponds, for example, to response times of PV MPPT algorithms and actuator [68–70] under good weather conditions. Partially shaded conditions are more challenging for MPPT algorithms and lead to response times in the order of hundreds of milliseconds [71–73]. This time constant is in the order of seconds for steam power plants and may reach tens of seconds for hydropower plants. It is assumed, at first, that the back-end converter is able to modulate its reference power.

The author has not, so far, found reports of PV controlled power modulation below the Maximum Power Point (MPP). If such a control proves to be a technical challenge, a simple alternative is to have a controllable, non essential load connected to the DC link. The power consumed by this load is a power reserve which may be diverted and used, if needed, during a disturbance.

WTG's capacity of responding to frequency change has been studied and implemented through two main techniques [13, 74, 75]. The first technique increases output power through an increase in electromagnetic torque applied to the generator, which can be performed through converter control and has a fast response. It draws from the kinetic energy stored in the turbine rotor, decreasing the turbine's rotating speed, and recovers afterwards, decreasing power output and reestablishing

its previous rotating speed. The second technique is based on the turbine's pitch governor, commanding change in blade pitch to increase power output in response to frequency change, an inherently slower mechanism, with time response comparable to that of hydropower plants [13], and that demands setting aside a power reserve. I.e., it requires cutting back power, not operating on the MPP, so there is room to increase power output when needed.

Increasing the back-end response time through the time constant $T_{be}$ increases the probability of an unstable set of parameters, but can be compensated by increasing the DC link controller's proportional gain or decreasing its integral gain, as shown in figure 4.18.

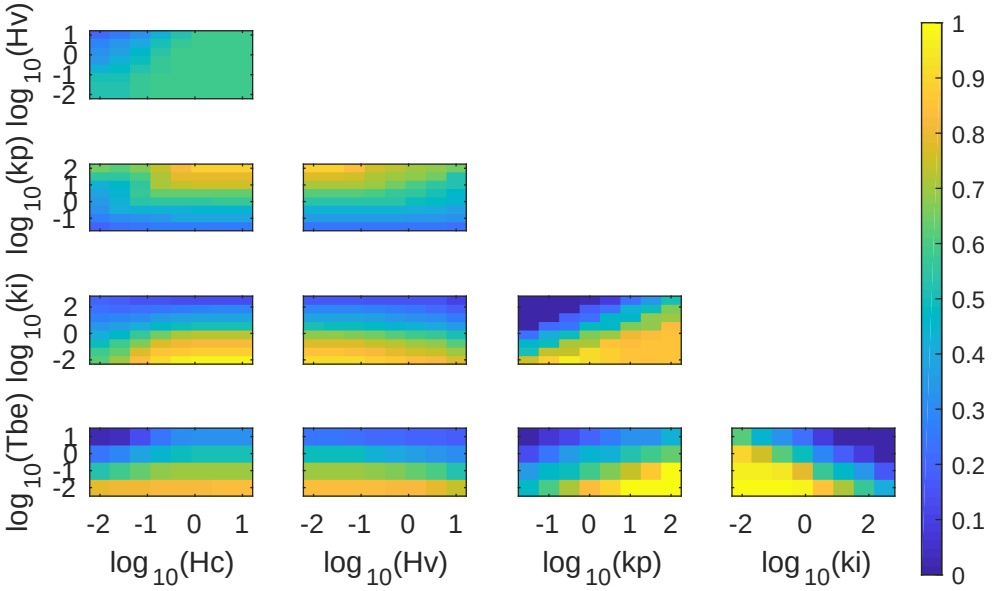


Figure 4.18: Proportion of stable model samples for given pair combinations of sampled parameters for the synchronverter with external DC link regulation.

If the DC link restriction of maximum ±0.2 p.u. deviation after the load disturbance is accounted for, then the valid samples dependence on parameters is as shown in figure 4.19. One may observe that the DC link controller integral gain has conflicting restrictions, as increasing it leads to instability and decreasing it leads to inability to comply with the DC link voltage deviation restriction. Parameter sets with simultaneously low proportional and integral gains were eliminated by this restriction, as can be observed when comparing their joint PDPs in figures 4.18 and 4.19.

Figure 4.20 shows the mean frequency nadir PDP considering stable model samples able to keep DC link voltage within bounds. The role of virtual inertia constant $H_V$ is evident, being the most influential parameter and causing an improvement in

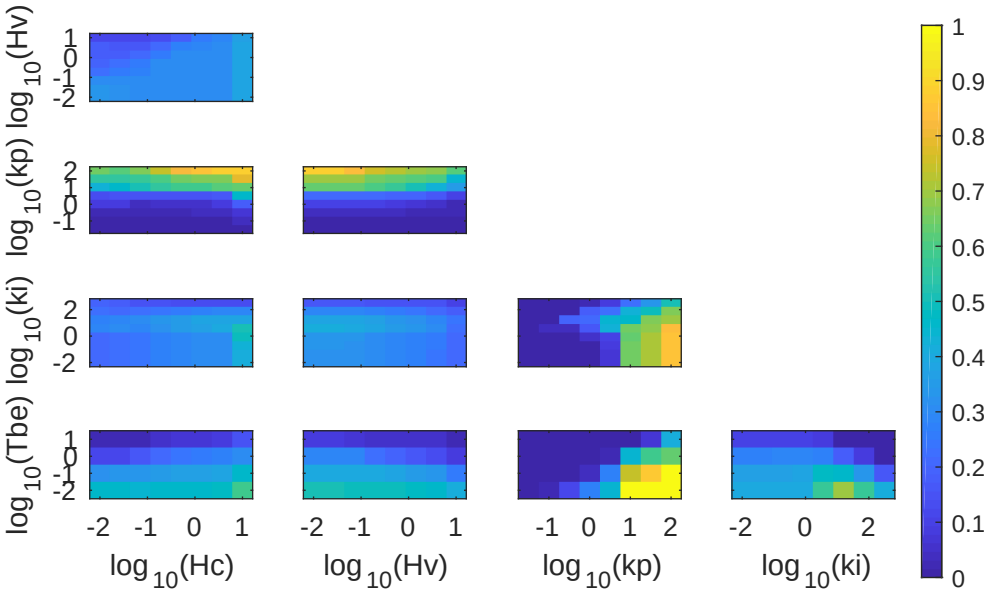


Figure 4.19: Proportion of valid model samples for given pair combinations of sampled parameters for the synchronverter with external DC link regulation. Valid samples must be stable and have its DC link voltage be within bounds after a disturbance.

mean frequency nadir of 0.00234 p.u. or 140 mHz between the lowest and highest sampled virtual inertia constant values. The isolated LFC model's frequency nadir for the load step being used is 56 Hz, meaning a 4 Hz frequency deviation nadir. That means the aforementioned change in virtual inertia constant improved mean frequency nadir in $0.14/4 = 3.5\%$ relative to the isolated LFC model's frequency deviation nadir.

In this condition, it is possible to reach high levels of frequency nadir difference, around 0.05 p.u., independently from capacitor inertia constant, as shown by ICE plots in figure 4.21. A synchronverter with DC link regulation could only reach such levels for the highest sampled capacitor inertia constant, of 10 s. The ICE plots in figure 4.21 show also how this topology has frequency support being determined almost exclusively by virtual inertia constant, as ICE plots for other parameters show little variation along their range of values.

However, this is only possible due to the back-end converter providing the necessary power to keep DC link voltage within bounds while the front-end converter freely modulates its output power, implementing a standard 5% droop. An additional restriction regarding the back-end converter must be considered: its power saturation. Its ability to increase power input into the DC link is limited by the power source behind it. In General Electric's implementation of temporarily increas-

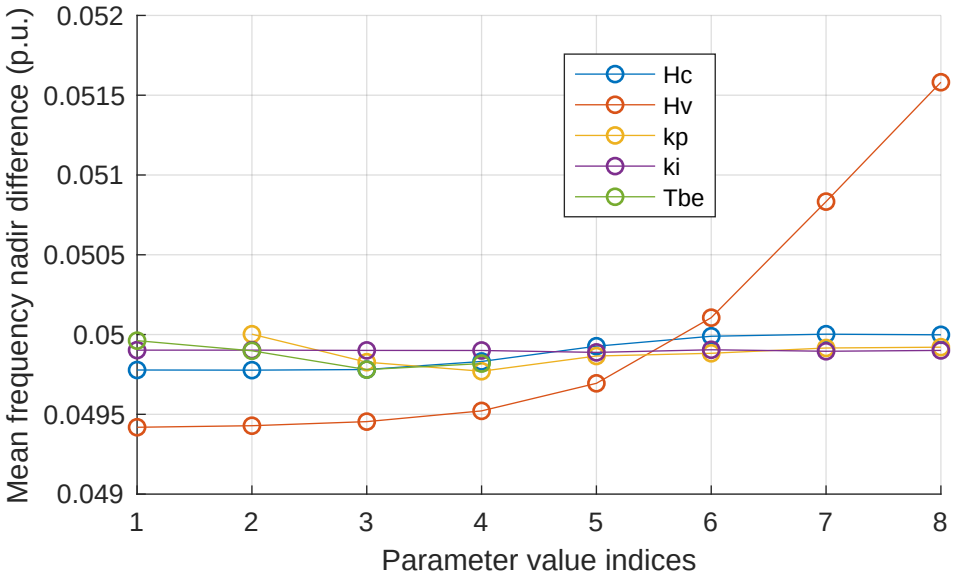


Figure 4.20: Mean frequency nadir difference for the synchronverter with back-end DC link regulation. The horizontal axis is an identifier for the sampled parameter value and may be regarded as a logarithmic scale.

ing electromagnetic torque in WTGs, WindINERTIA$^{TM}$, power output increase is limited to 10% of the turbine's rated power and may last several seconds [76]. Additionally, WindINERTIA$^{TM}$implements a low-pass filter on the measured frequency error signal, with a recommended time constant of 1 s.

If this restriction is applied through exclusion of model samples whose back-end power deviation under the reference load disturbance leave the range $(0, 0.25)$ p.u., then valid model samples are very few, as shown in figure 4.22. All parameter sets that can fulfill this requirement have a 10 s capacitor inertia constant.

This is, however, more restrictive than reality, as the back-end power will in fact saturate. In this situation, DC link undervoltage may be prevented through front-end converter action. The front-end converter must limit output power when there is risk of tripping from DC link undervoltage, then it may continue providing power during the disturbance. Limiting output power would limit also its contribution to grid frequency, but the alternative, protection tripping and cutting off power output completely, is worse.

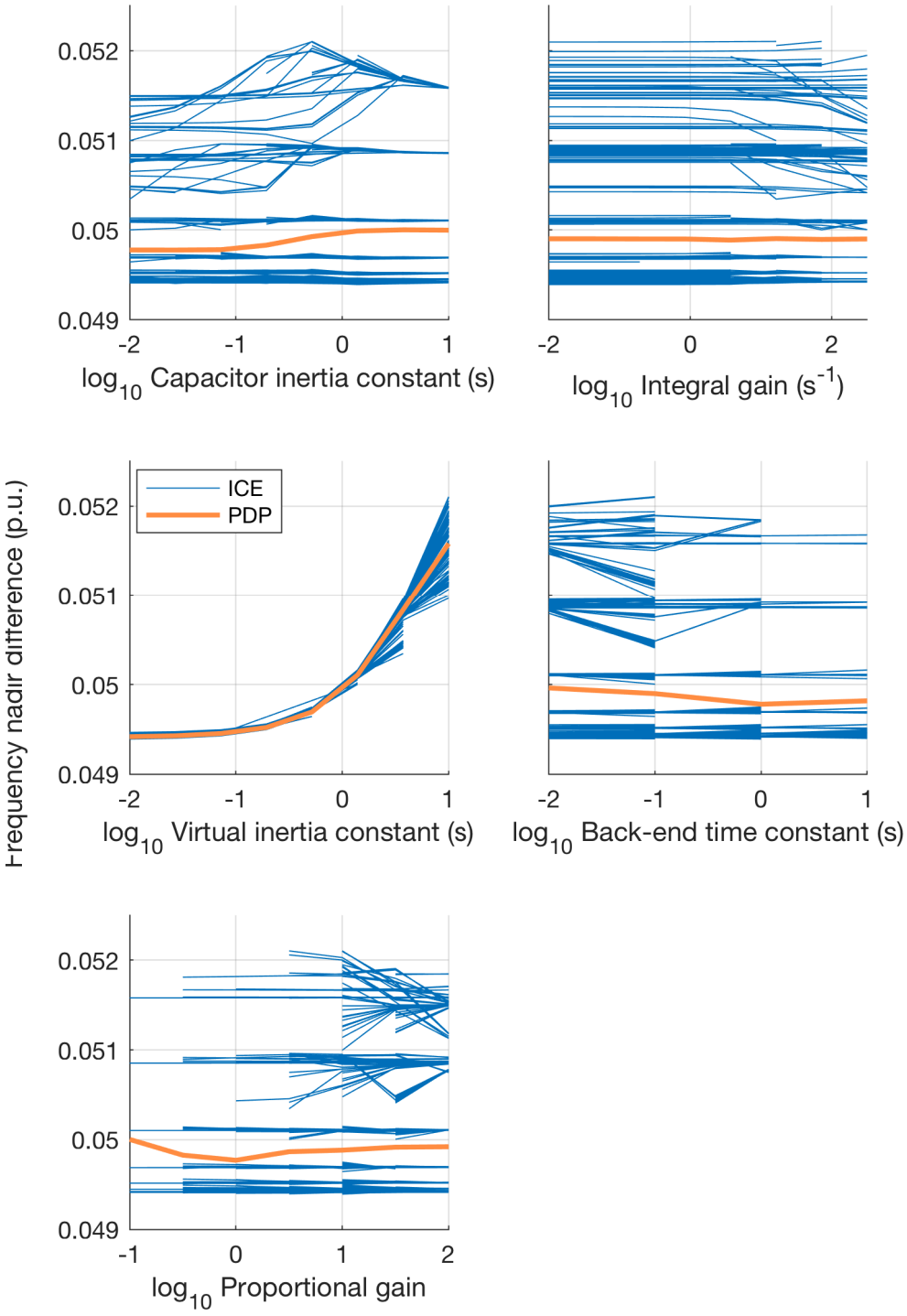


Figure 4.21: Mean frequency nadir difference for the synchronverter with back-end DC link regulation. The horizontal axis is an identifier for the sampled parameter value and may be regarded as a logarithmic scale.

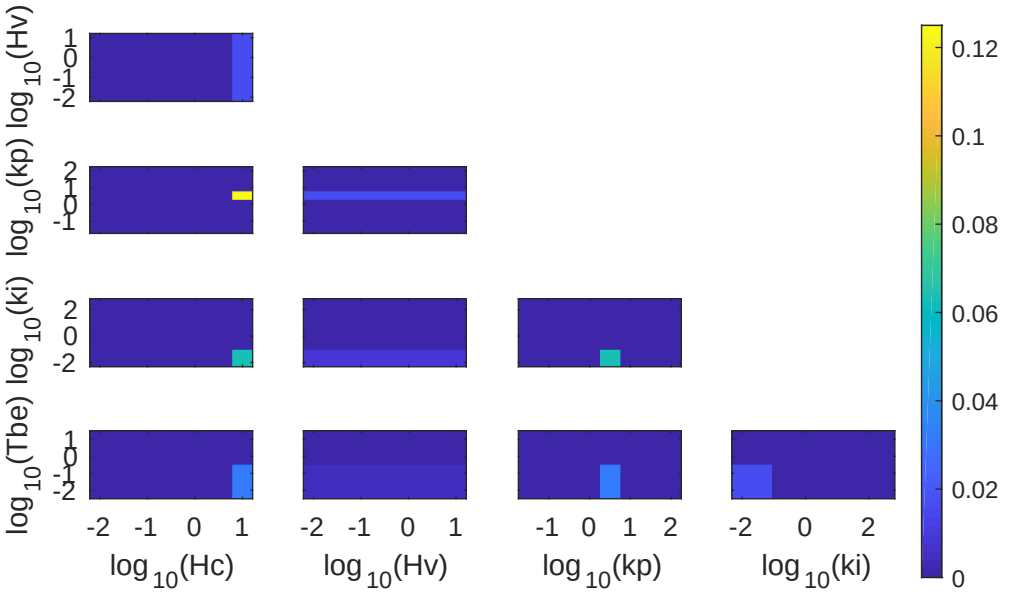


Figure 4.22: Proportion of valid model samples with respect to sampled parameters for the synchronverter with external DC link regulation. Valid samples must be stable, have its DC link voltage be within bounds after a disturbance and have back-end power deviation be inside the range $(0, 0.25)$ p.u. Color axis range was decreased to enable visualization of plot details.

### 4.3.3 Synchronverter with DC link regulation and back-end converter droop

Consideration for the back-end converter's power saturation brings us back to the synchronverter that regulates its own DC link. Having the synchronverter regulate its DC link will keep it from tripping from DC undervoltage. The DC link control will effectively limit output power in order to keep voltage within bounds.

If the back-end converter is nevertheless allowed to modulate its power output when necessary, then it can contribute to frequency stability as long as it has power reserve to do so. A droop controller may be implemented in the back-end converter with the same 5% characteristic as the synchronverter's. The back-end droop controller may act upon measured grid frequency or upon the synchronverter's own virtual rotor speed, if that information is easily accessible through communication or if both controllers are implemented in the same microcontroller.

In such an arrangement, a major disturbance will quickly saturate back-end power, consuming power reserve. For a 5% droop curve, a 0.5% drop in frequency, to 59.7 Hz, will cause a 10% increase in back-end power output. The synchronverter-controlled front-end's droop loop will be sensing the same frequency change and ordering an increase in power output through $T_d(t)$. If back-end power reserve is 10%

and frequency drops further, the synchronverter's droop loop continues to increase its power output order, even though back-end power remains constant at 10% above its initial value. DC link voltage will then begin to drop and the synchronverter's DC link controller starts to act, compensating the droop command and stabilizing power output at 10% above the initial value.

This scheme was simulated in PSCAD$^{TM}$, with the simulation shown in figures 3.7 and 3.8, with the hydraulic and turbine LFC model and the back-end droop control shown in figure 4.23. The described effect is shown in frequency, DC link

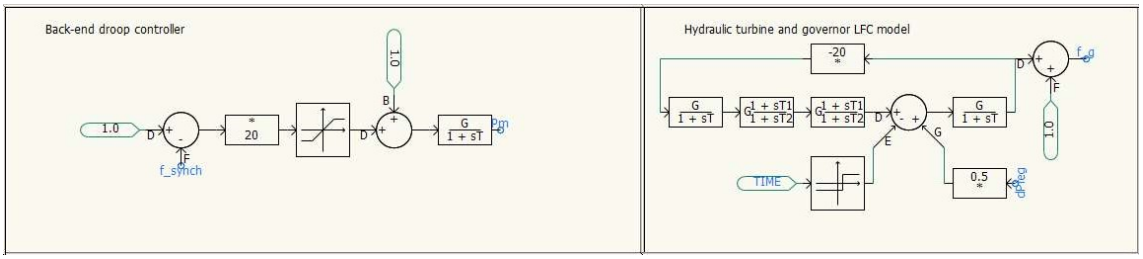


Figure 4.23: Back-end active power droop controller and hydraulic turbine and governor LFC model. The back-end active power droop controller has 10% saturation, using synchronverter's virtual rotor speed $f\_synch$, a power setting in the summing block's $B$ port and a low-pass filter.

voltage, back-end and front-end powers in the time plots in figure 4.24. Back-end power implemented a 5% droop curve with saturation at 10%, an initial output power of 1 p.u. and a low-pass filter in its output with $T_{be} = 1$ s models the transfer function from back-end power reference to actual back-end power. The synchronverter had $k_p = 2.7$, $k_i = 3.0$ s$^{-1}$ and $H_V = H_C = 51.4$ ms. The LFC model's base power was twice the synchronverter's, and at 5 s into the simulation, a 19.7% load step was applied, which would have a 4 Hz deviation if the LFC model had been disconnected from the synchronverter. Frequency nadir difference was 0.012 p.u., equivalent to a normalized frequency nadir difference (a reduction in frequency nadir) of $0.012/(4/60) = 18\%$.

Saturation can be considered in the developed small-signals model if it is possible to consider that the signal saturates very quickly. For large disturbances, as the one shown in figure 4.24, frequency drops quickly, in this case with an average ROCOF of 1.08 Hz/s. This means back-end power reference saturates within $0.3/1.08 \approx 0.278$ ms and the signal into the low-pass filter in figure 4.23 can be approximated by a step function of amplitude equal to the saturation limit of 10%.

The synchronverter model developed in section 3.2 was then modified through the addition of a low-pass filter with unit static gain and time constant $T_{be}$ in series with the input variable $\Delta\bar{p}_{be}(t)$. New data were generated applying a 10% step to the synchronverter's back-end power reference additionally to the load step in the

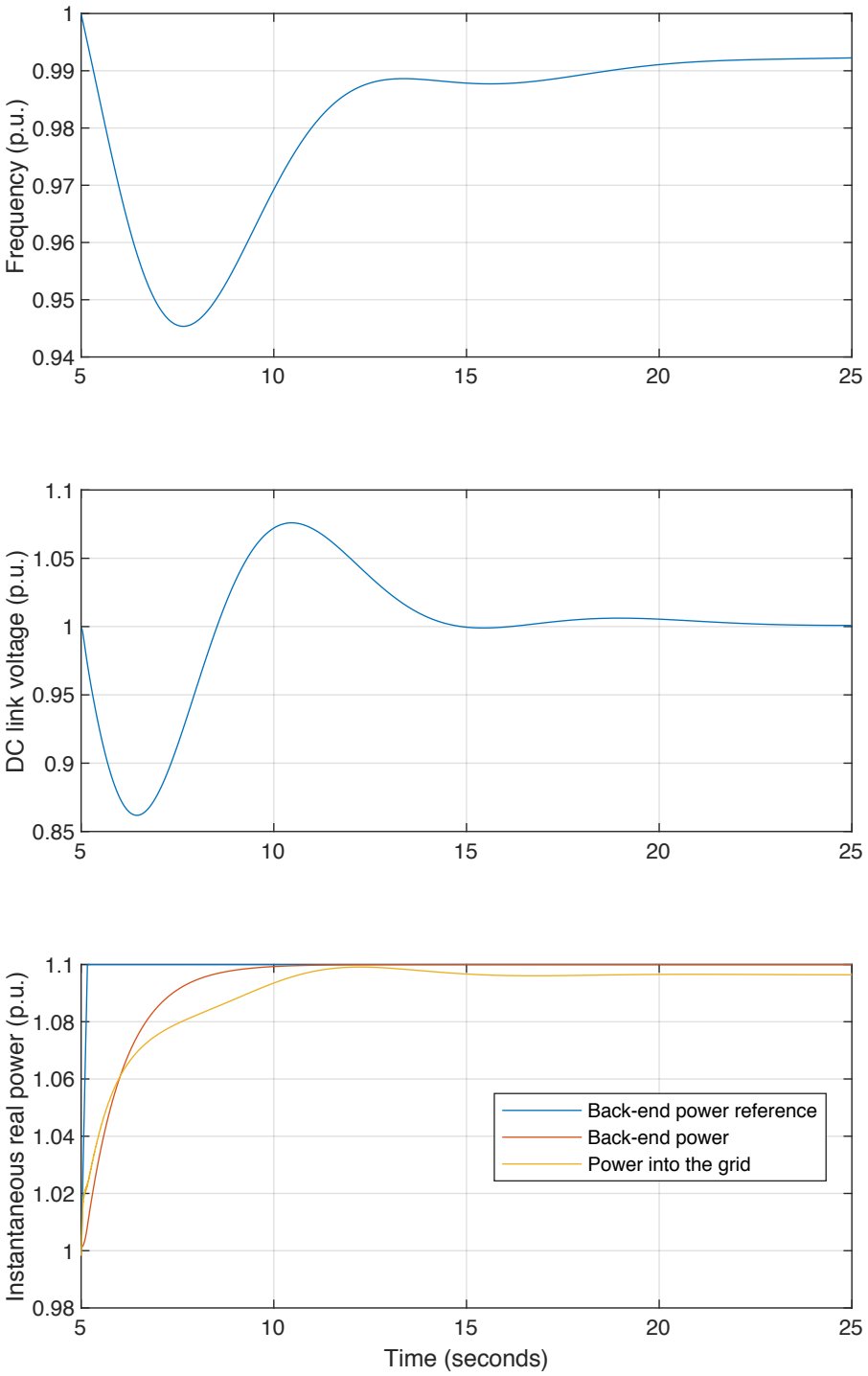


Figure 4.24: Frequency, synchronverter DC link voltage, back-end power reference, back-end power and power injected in the voltage source controlled by the LFC model in the case the back-end converter implements an active power droop curve upon the synchronverter's frequency.

LFC model. ICE plots for the sampled models in this new configuration are shown in figure 4.25. The plots for integral gain, proportional gain and virtual inertia constant have similar structures as the ones seen in figure 4.17.

The capacitor inertia constant ICE plot has three distinguishable levels across mid and lower ranges. These correspond to different back-end time constants, with smaller time constants leading to higher frequency nadir differences. As can be seen from the back-end time constant PDP in figure 4.25, mean frequency nadir difference falls with growing back-end time constant. As the back-end converter takes longer to throttle up its power output, DC link voltage drops and the synchronverter's DC link controller limits power output, limiting also contribution to frequency stability.

Finally, if one considers the frequency nadir difference possibilities once the capacitor inertia constant is determined, it is possible to analyze sensitivity to control parameters and back-end time constant for typical capacitor inertia constant. Capacitor inertia constant is usually in the range of $(10^{-2}, 10^{-1})$ s. The back-to-back converters used in chapter 5 have a 51.4 ms capacitor inertia constant and this value will be used for the following plots.

Two-dimensional valid sample regions in this case are plotted in figure 4.26, for all stable model samples, and figure 4.27, applying the DC link voltage restriction. Back-end time constant has no effect in these plots, since the developed model considers back-end power saturation, meaning back-end power control is an open loop.

The one-dimensional plot for valid samples with DC link voltage restriction is presented in figure 4.28. It highlights the trend shown in the two previous plots of a declining number of valid models for an increasing virtual inertia constant. Additionally, its peaks suggest DC link controller gains for implementation.

ICE plots for the 51.4 ms capacitor inertia constant, with saturated 10% back-end power increase, DC link regulating synchronverter show how, in these conditions, contribution to grid frequency is almost exclusively determined by the back-end power dynamics. The plots are shown in figure 4.29.

Control parameters have comparatively very little influence over frequency nadir difference. A decrease in the back-end time constant from 1 s to 0.1 s, i.e., the back-end converter's ability to more quickly increase power extraction from its primary power source, increases mean frequency nadir difference from 0.0026 p.u. to 0.0168 p.u., a $60 \times (0.0168 - 0.0026) = 0.852$ Hz increase, or 21.3% with respect to the isolated system's frequency deviation nadir of 4 Hz. The control parameter found to cause the most significant change to frequency nadir difference was the proportional gain, as highlighted by the red curve in centered ICE plot in figure 4.30, but it can't be said to be a consistent behavior of changes to proportional gain across different

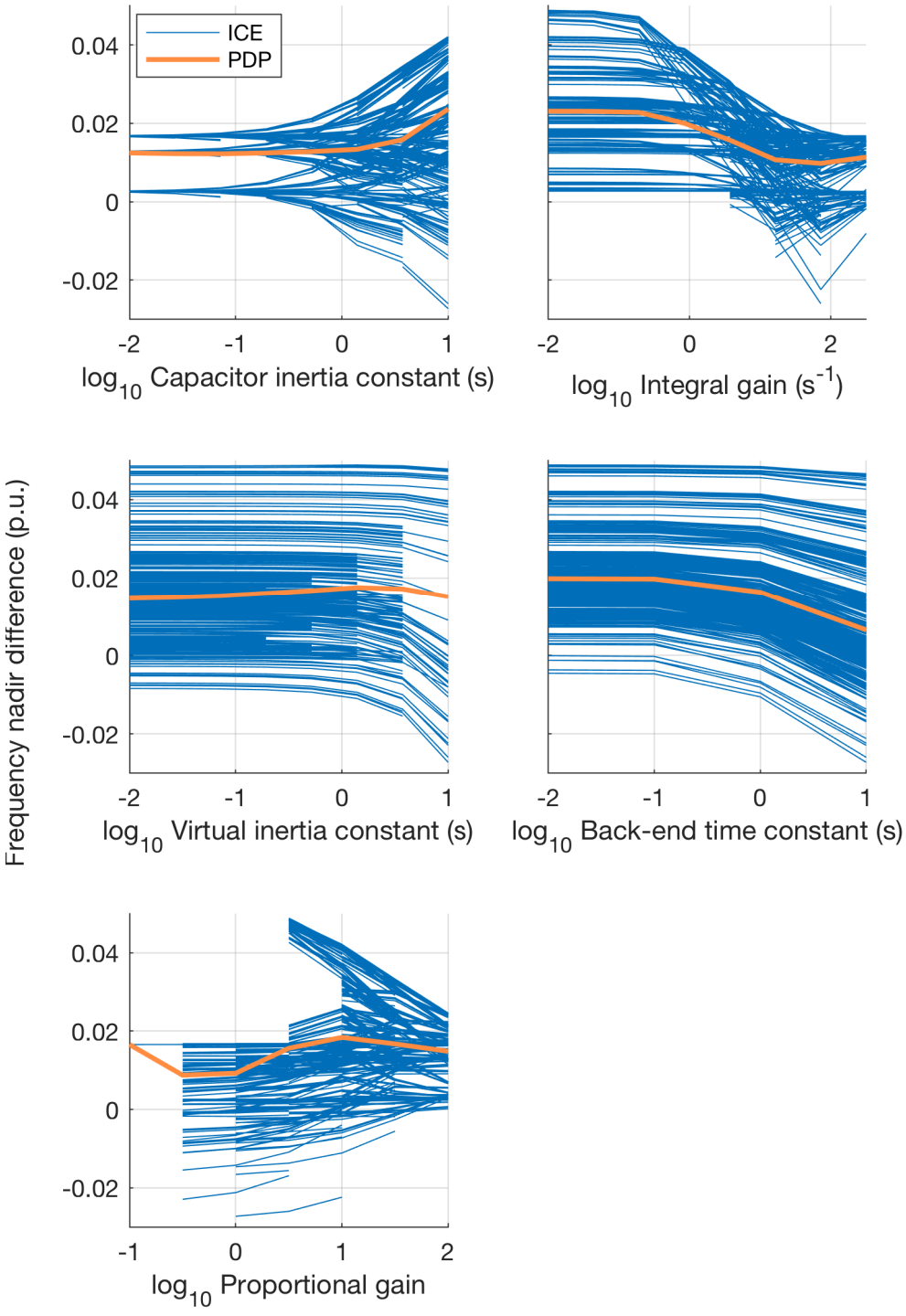


Figure 4.25: Individual Conditional Expectation (ICE) plots for frequency nadir differences (with respect to the isolated system) with superimposed PDP. Results obtained for all stable parameter sets able to keep DC link voltage within bounds, evaluated for the synchronverter that regulates its DC link and receives a 0.1 p.u. power injection from the back-end converter at the moment of the disturbance.

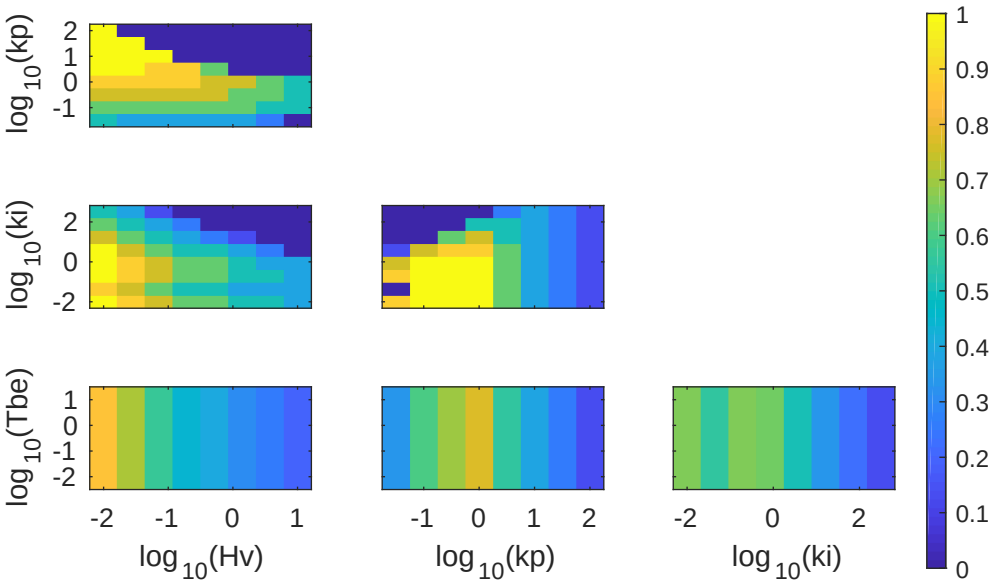


Figure 4.26: Proportion of stable DC link regulating synchronverter model samples for given pair combinations of sampled parameters.

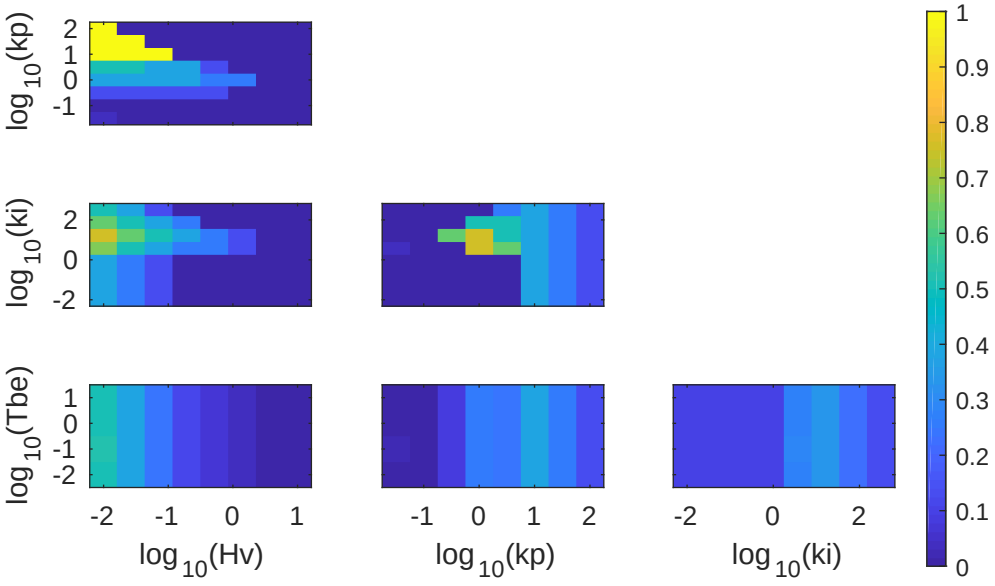


Figure 4.27: Proportion of stable DC link regulating synchronverter model samples capable of regulating DC voltage within ±0.2 p.u. for given pair combinations of sampled parameters.

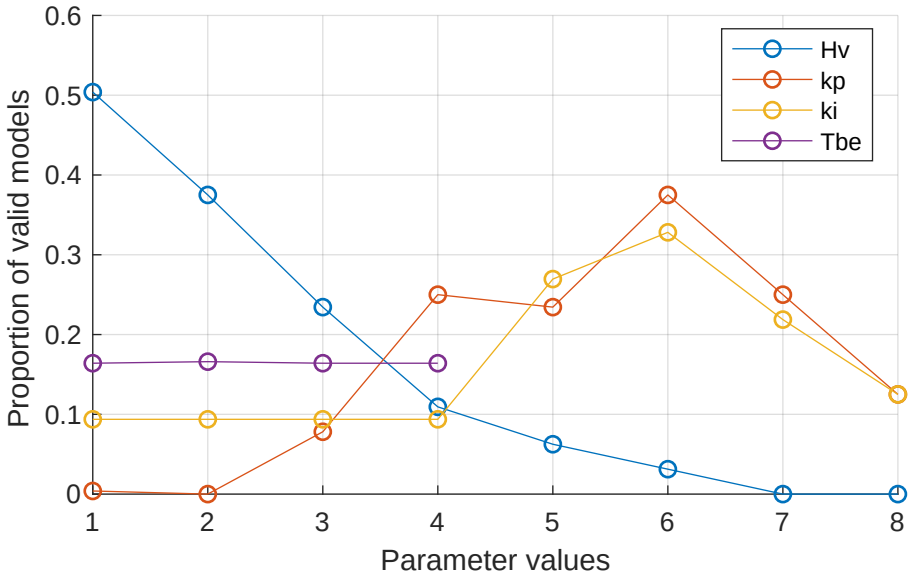


Figure 4.28: Proportion of stable DC link regulating synchronverter model samples capable of regulating DC voltage within ±0.2 p.u. for a given load disturbance for each sampled parameter value.

parameter sets. It caused a 1.8% increase relative to the isolated system's frequency deviation nadir when proportional gain changed from 1 to 10 in the parameter set with a 0.01 s virtual inertia constant, 3.73 $s^{-1}$ integral gain and 10 s back-end time constant.

Figures 4.28 and 4.29 highlight that increasing virtual inertia constant leads to smaller chances of finding a stable set of parameters with no benefit to contribution to grid frequency stability. DC link controller parameters also show no clear trend or possible design guidelines for improving contribution to grid frequency stability, unless new designs and technologies shift towards higher capacitor inertia constants. The main factor in power electronics based generation's contribution to grid frequency stability is primary power sources and ESS's response time and available power reserve. This should be the focus of efforts towards improvement of power electronics based generation's contribution to grid frequency stability.

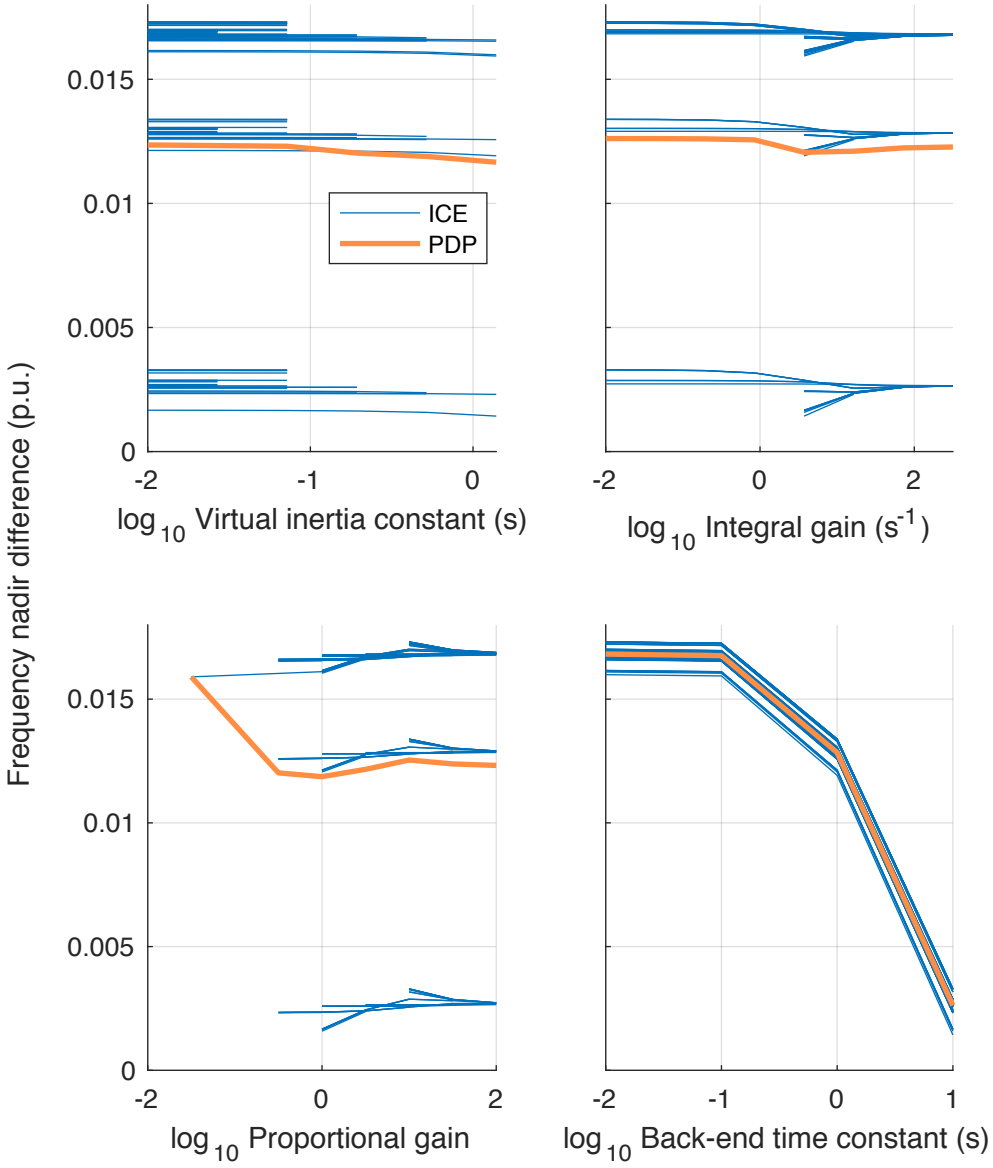


Figure 4.29: Individual Conditional Expectation (ICE) plots for frequency nadir differences (with respect to the isolated system) with superimposed PDP. Results obtained for all stable parameter sets able to keep DC link voltage within bounds, evaluated for the synchronverter that regulates its DC link with a 10% back-end power reference step at the moment of the disturbance.

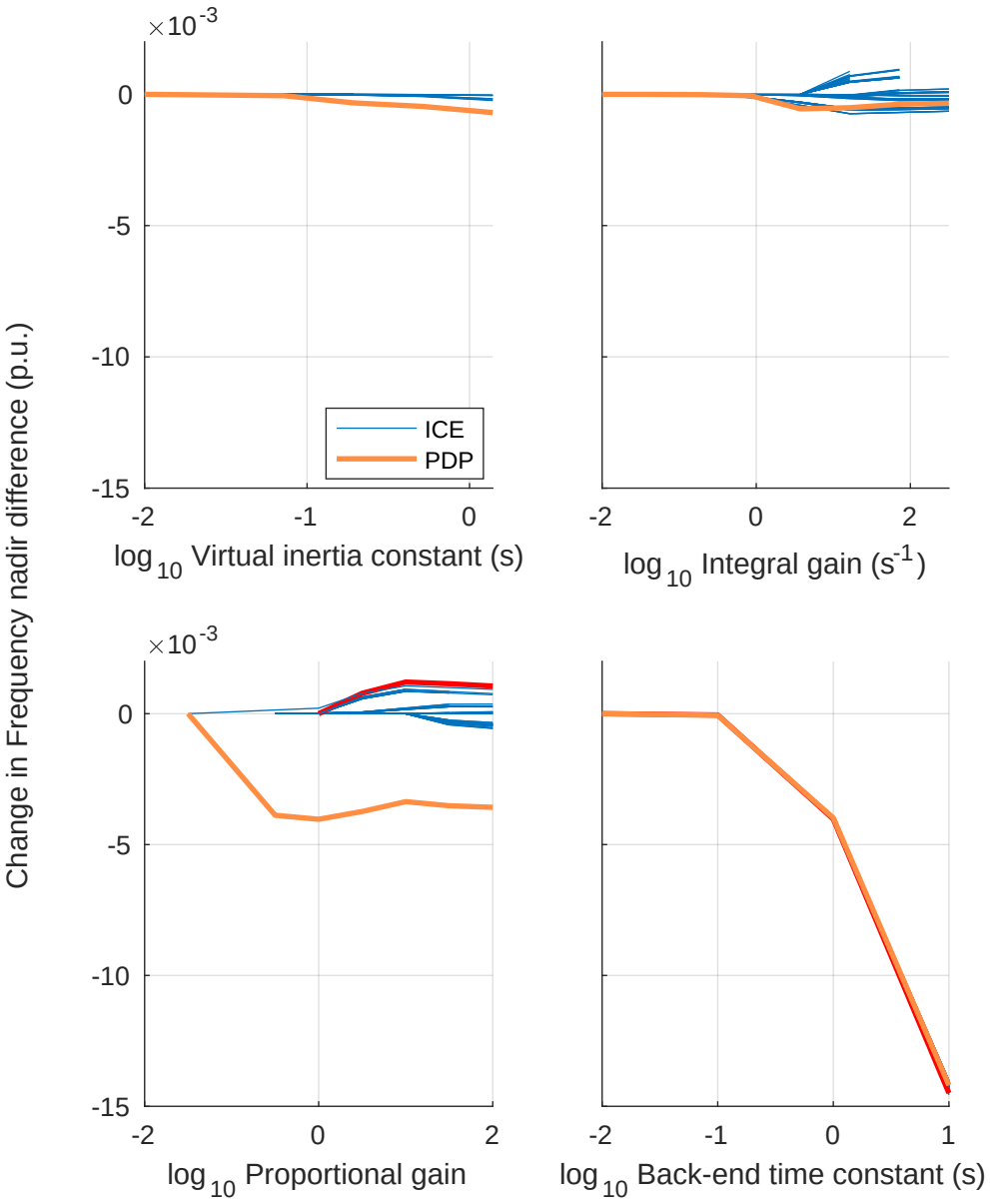


Figure 4.30: Centered Individual Conditional Expectation (ICE) plots for frequency nadir differences (with respect to the isolated system) with superimposed PDP. Results obtained for all stable parameter sets able to keep DC link voltage within bounds, evaluated for the synchronverter that regulates its DC link with a 10% back-end power reference step at the moment of the disturbance. Highlighted in red the parameter set in the proportional gain plot that caused the most significant change in frequency nadir difference, a 1.8% increase relative to the isolated system's frequency deviation nadir.

# Chapter 5

# Measurement methodology

In order to test a generating unit, a turbine and governor model may be embedded in a testing unit converter's microcontroller. The testing unit converter will be made to generate three-phase symmetrical voltages with fixed amplitudes, but with frequency given by the turbine and governor model. The turbine and governor model will take the electrical power coming from the tested converter as input. The tester converter, *Converter 2*, is connected in series between the grid and the tested unit, *Converter 1*, as in figure 5.1.

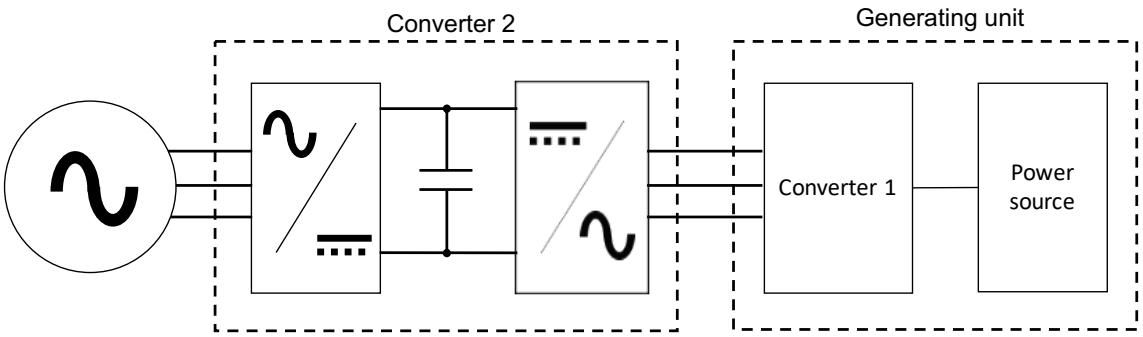


Figure 5.1: Test rig to determine frequency stability contribution of the generating unit whose interface is *Converter 1*, which would otherwise be connected to the grid. *Converter 2* is the equipment used to perform this measurement.

## 5.1 Hydraulic turbine and governor model emulating converter

### 5.1.1 Model discretization

In order to have one of the converters, which shall be called *Converter 2*, the tester unit, behave as a three-phase voltage source whose frequency is given by the hydraulic turbine and governor load-frequency control model, the model must be

translated into a set of difference equations to be computed periodically by the microcontroller. This process is called discretization, i.e., the representation of a continuous-time dynamic system by a discrete-time dynamic system. Final C++ implementation code is presented in Appendix B.

### Discretization method

The small-signals hydraulic turbine and governor model shown in section 3.1.1 was discretized using the zero-order hold method. This method assumes the system's input signals change in regularly-spaced steps, i.e., changes happen at a constant frequency and the input signals are held constant between changes, and the system's output signals are evaluated or measured at the same constant frequency, at the same time input signals change. In other words, the system's input signals are continuous in time, but constant between the measurements of the system's output signals. The interval between measurements of the system's outputs is called the system's sampling period. If such an assumption is true, then the zero-order hold discretization method gives an exact representation of the system's inputs and outputs at the sampling instants in time [77].

For a system described by the state space equations (5.1), zero-order hold yields the new system of state space equations (5.2). It describes the same dynamic system, but at instants in time $t_k = kh$, for an integer $k$, separated by a constant sampling period $h$.

$$\begin{aligned} \dot{\vec{x}}(t) &= A\vec{x}(t) + B\vec{u}(t) \\ \vec{y}(t) &= C\vec{x}(t) + D\vec{u}(t) \end{aligned} \tag{5.1}$$

$$\begin{aligned} \vec{x}(kh+h) &= e^{Ah}\vec{x}(kh) + \int_0^h e^{As} ds B\vec{u}(kh) \\ \vec{y}(kh) &= C\vec{x}(kh) + D\vec{u}(kh) \end{aligned} \tag{5.2}$$

Using such a discretization method for the hydraulic turbine and governor model would be an approximation, as its input signal, the generating unit to be tested's output power, is not guaranteed to be constant between sampling intervals. Furthermore, the original system's continuously-varying frequency output is evaluated at the same, constant, rate and used as the converter's three-phase voltage source frequency. I.e., the output frequency is also approximated to a staircase function.

### Discretized model response convergence

The discretization sampling frequency is the frequency at which the microcontroller periodically measures inputs and calculates its outputs. The discretized model was calculated by MATLAB®'s *c2d* function, with the zero-order hold method, initially with the same sampling frequency as the converter's digital control system, 5100 Hz, resulting in the transfer function in equation (5.3).

$$H(z) = \frac{3.268 \times 10^{-5} z^3 - 9.799 \times 10^{-5} z^2 + 9.795 \times 10^{-5} z - 3.263 \times 10^{-5}}{z^4 - 3.999 z^3 + 5.996 z^2 - 3.996 z + 0.9986} \quad (5.3)$$

Testing the C++ implemented difference equation algorithm for equation (5.4) through a testing routine in a computer showed over 10% difference at some points from the continuous transfer function's response simulated in MATLAB®. Increasing past inputs and past outputs variables' floating-point precision reduced the error, but it was still significant.

$$\begin{aligned}\omega_k = {} & 3.268 \times 10^{-5} p_{k-1} - 9.799 \times 10^{-5} p_{k-2} + 9.795 \times 10^{-5} p_{k-3} - 3.263 \times 10^{-5} p_{k-4} + \\ & 3.999 \omega_{k-1} - 5.996 \omega_{k-2} + 3.996 \omega_{k-3} - 0.9986 \omega_{k-4}\end{aligned} \quad (5.4)$$

The algorithm programmed in C++ to be embedded in the microcontroller was reproduced in MATLAB®language and its output to a step input was compared to those of other MATLAB®functions which could perform the same task, namely *lsim*, *ltitr*, *step* and *filter*. Also used for comparison was the step response of the continuous time transfer function, as given by MATLAB®'s *step* function. These are shown in figure 5.2, where "Implemented difference equation" refers to the implemented algorithm, a recursive calculation of the difference equation taken from the discretized model's transfer function.

Different simulation methods give very different results for this discrete transfer function, the time response does not converge among the different methods. This lead to the suspicion that the system's sampling frequency was too high to precisely emulate the turbine and governor model with the available floating-point precision, which led to the final solution of downsampling presented next. Later, however, it was found that that the difficulty in representing the discrete system only happened when representing it through a transfer function. The system's embedded simulation could have been implemented as a recursive calculation of the discrete state space equation, without needing to resort to downsampling, but at higher computational costs.

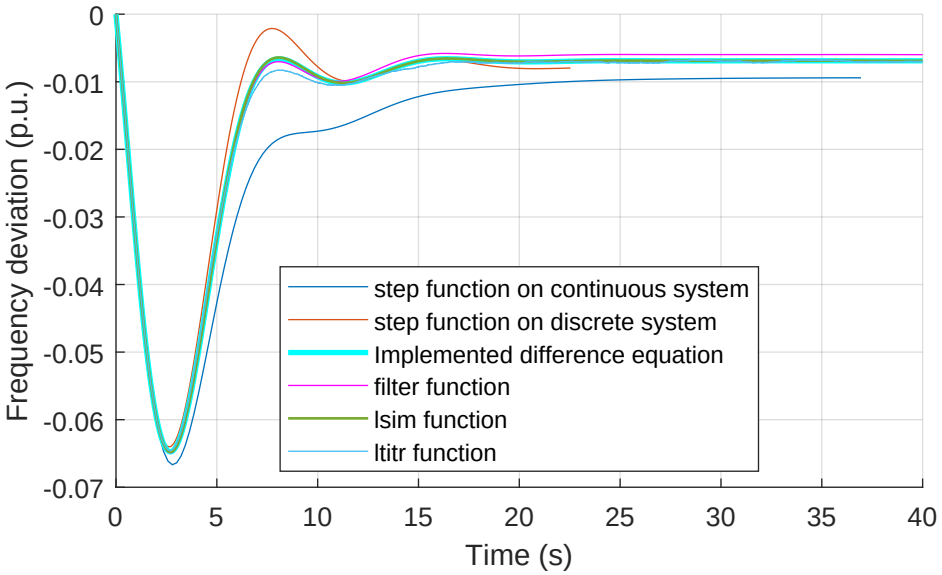


Figure 5.2: Step response (19.7% load power increase) as calculated by different methods, for the continuous and the discretized models, sampled at 5100 Hz.

### Downsampling

The solution to the discretized model stability was to downsample the model, only calculating its response for every $n$ calls to the microprocessor's interruption routine. A choice of $n = 10$, leading to the transfer function in equation (5.5) at a 510 Hz sampling frequency, was sufficient to achieve a stable system and yet, fast enough to be able to respond to the expected power signals.

$$H(z) = \frac{0.0003267z^3 - 0.0009758z^2 + 0.0009713z - 0.0003223}{z^4 - 3.986z^3 + 5.958z^2 - 3.958z + 0.986} \tag{5.5}$$

With this discretization, implemented by difference equation 5.6, all simulation methods yielded the same results, shown in figure 5.3.

$$\begin{aligned}\omega_k = {} & 0.0003267p_{k-1} - 0.0009758p_{k-2} + 0.0009713p_{k-3} - 0.0003223p_{k-4} + \\ & 3.986\omega_{k-1} - 5.958\omega_{k-2} + 3.958\omega_{k-3} - 0.986\omega_{k-4}\end{aligned} \tag{5.6}$$

Zero-order hold discretization means the continuous system's response is calculated once every sampling period for an input signal that is held constant between samplings. For a 510 Hz sampling period, this means the generating unit's power going into the turbine and governor model is allowed to change only in steps approximately 1,96 ms wide. To know whether this sampling rate is adequate for the

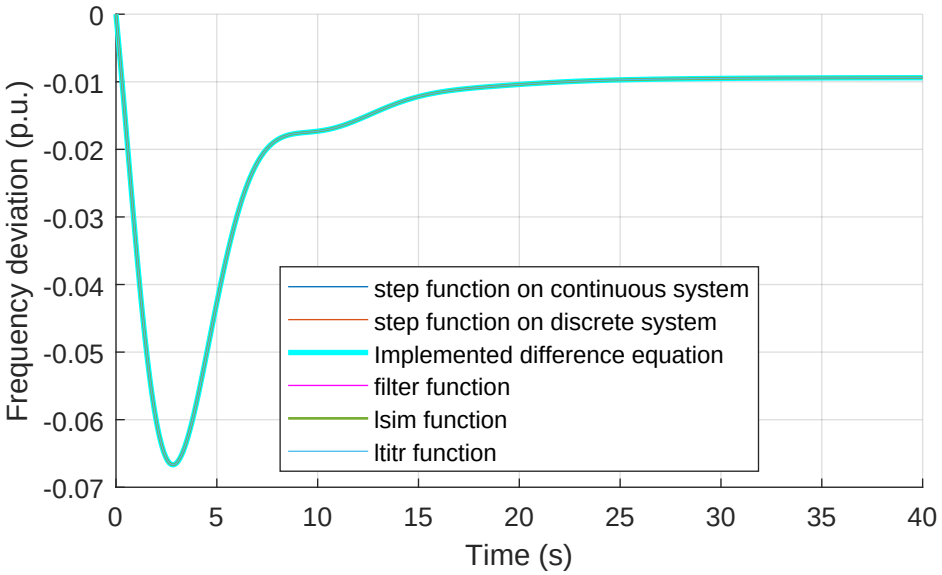


Figure 5.3: Step response (19.7% load power increase) as calculated by different methods, for the continuous and the discretized models, sampled at 510 Hz.

signals expected for the input power, the continuous and the discretized models were simulated for a exponentially-decaying sinusoidal input signal. The input signal's is an excited mode of the 3 s virtual inertia constant, 0.28 s capacitor inertia constant, $k_p = 2.7$, $k_i = 3$ s$^{-1}$ synchronverter with DC link regulation model, associated with the dominant pair of complex poles for the transfer function from grid frequency to front-end power into the grid. The results are shown in figure 5.4.

### Transfer function coefficients representation

When the test routine was first triggered in the embedded environment, the PWM reference signals turned from sinusoids into what seemed like noise, as shown by the CCS debug session screenshot in figure 5.5. It was observed that the internal frequency output variable quickly took absurd values, in the order of thousands of times its base value.

It was found on the computer based testing routines that using a more precise representation, 64-bit floating point, for the difference equation coefficients resulted in the correct emulation of the turbine and governor model. In fact, figure 5.6 shows the difference in computing the transfer function's poles and zeros in MATLAB®when using IEEE®Standard 754's 32-bit floating point (single precision) or 64-bit floating point (double precision, which MATLAB®uses by default) representations for the difference equation coefficients. These are poles and zeros of

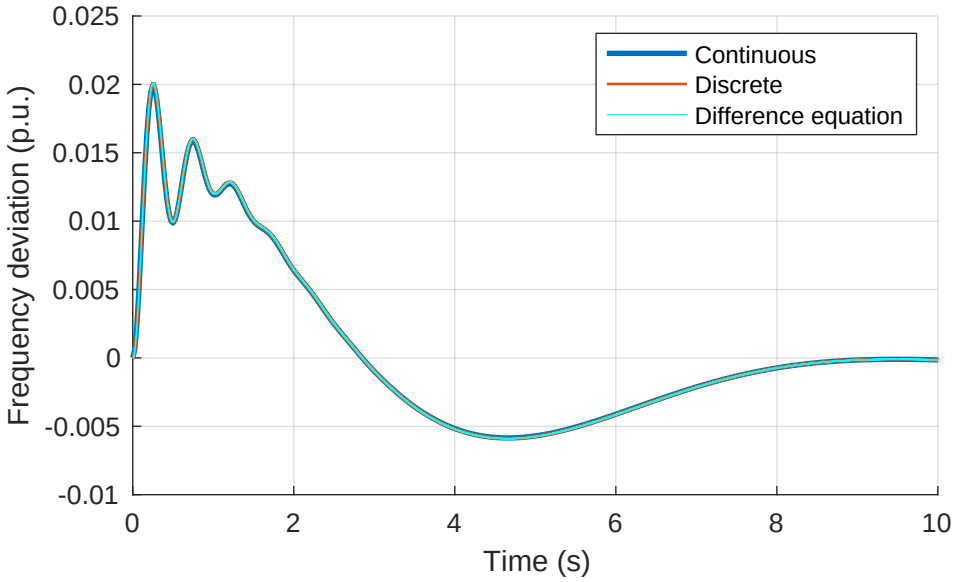


Figure 5.4: Continuous and discretized models' responses to a sample decaying sine signal of frequency 2 Hz and decaying time constant 0.43 s computed through MATLAB®'s *lsim* and through the algorithm implemented in the embedded control (Implemented difference equation).

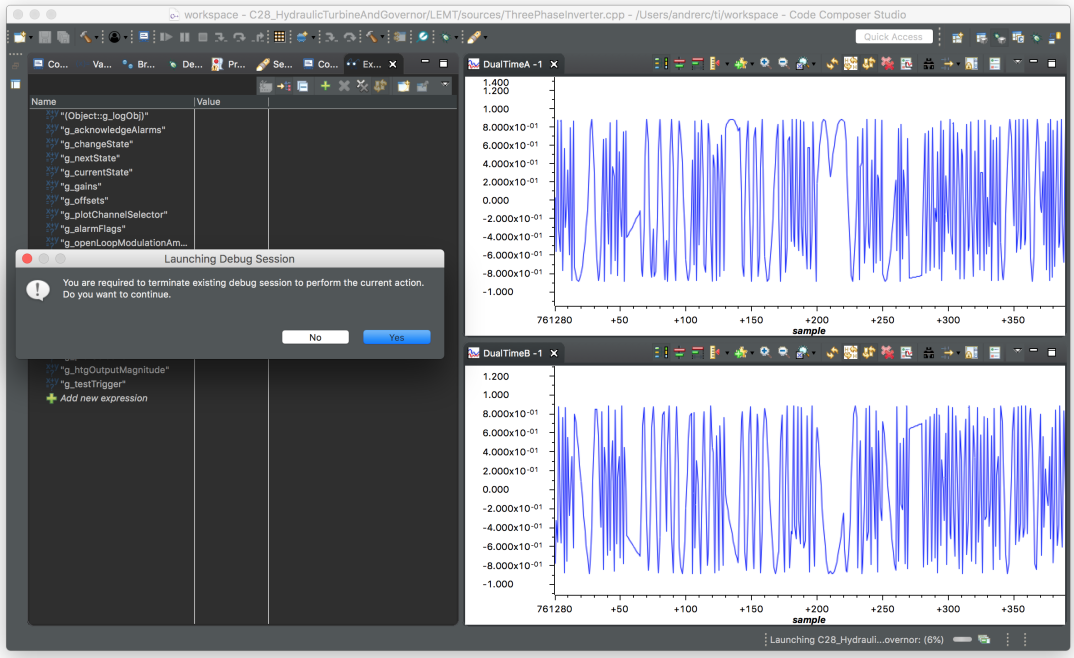


Figure 5.5: Code Composer Studio (CCS)'s debug view with memory readings of PWM reference signals composed of noise.

a discrete system, therefore the rightmost pole, which lies outside the unit circle, denotes an unstable system when its coefficients are represented in single precision. One might question whether the poles of such a sensitive set of coefficients might be accurately computed, however, this conclusion is backed by the observations reported above.

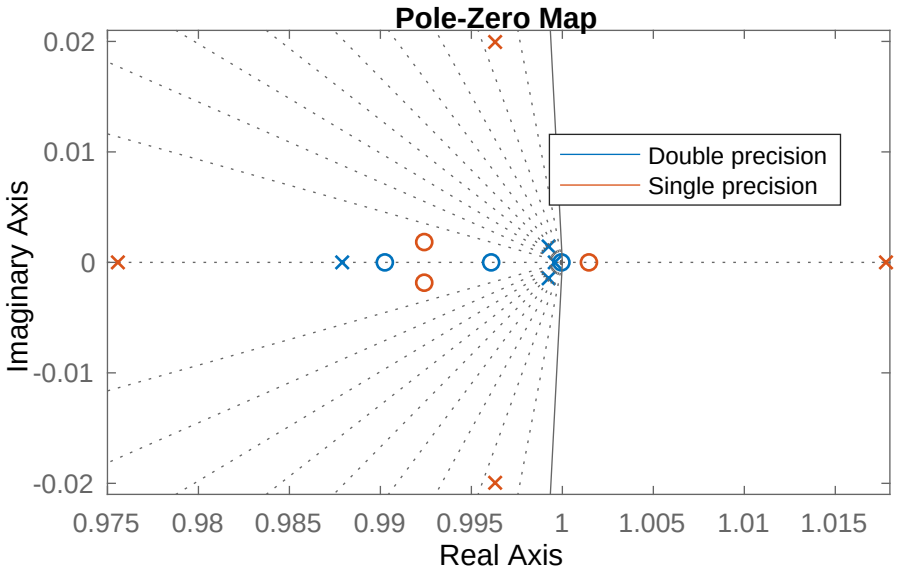


Figure 5.6: Pole-zero maps of discrete systems when coefficients are represented using single (IEEE®754 32-bit floating point) or double precision (IEEE®754 64-bit floating point).

Texas Instruments' C28x microprocessor architecture's C language *float* type, as well as *double* type both use IEEE®Standard 754's 32-bit floating point representation. IEEE®754's double-precision, 64-bit floating point representation is obtained when the *long double* variable type is used. This fact explains the difference between the computer based testing routines, whose *double* type means a 64-bit floating point number, and the microprocessor based execution. After changing the difference equation coefficients and past values variables, the difference equation algorithm for the hydraulic turbine and governor transfer function performed as expected.

### 5.1.2 Power disturbance test cycle

Once both converters are connected and operating, testing is simple, as described by *Converter 2*'s state machine diagram in figure 5.7. The converter is initially in standby mode and operates as a three-phase, symmetrical, constant frequency,

voltage source.

If a trigger signal is sent, which is currently being done through changing a trigger variable in a CCS debug session, the converter changes into a testing state. It then resets the hydraulic turbine and governor transfer function, setting all its past outputs and past inputs variables to zero, records the present real power being absorbed by the converter, resets the test's time counter, which expires after 20 s, and resets the maximum frequency deviation record. A step is applied to the turbine and governor model, emulating a step change in the sum of powers in the systems, such as a load

If the trigger signal is cleared or 20 s pass from the beginning of the test, the converter goes into a recovery state, where it takes the output frequency in a ramp back to 60 Hz in two seconds. After it reaches 60 Hz, the converter goes back to standby.

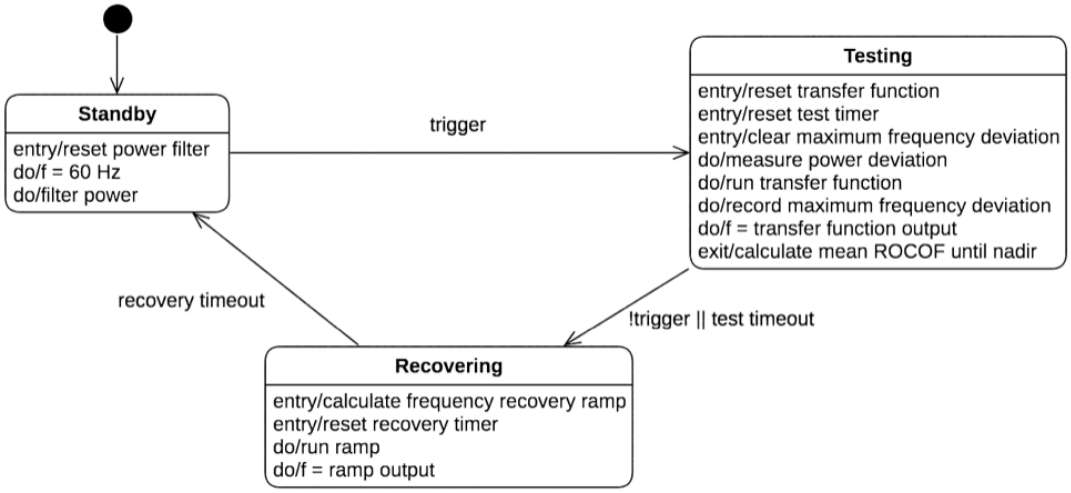


Figure 5.7: State machine implemented in *Converter 2*.

### 5.1.3 Voltage controller design

In order to guarantee a regulated voltage for the equipment being tested, despite frequency and power flow changes that will happen during the power disturbance test, a voltage controller must be implemented in *Converter 2*. *Converter 2* was modelled as an LC filter with a controlled voltage source $v_{conv}$ behind the inductor $L_{conv}$ and an unknown current $i_{grid}$ being drawn after the capacitor $C$, as shown in figure 5.8. The inductor has resistance $R$.

Kirchhoff's voltage law applied to the circuit's left side loop gives equation (5.7).

$$v_{conv} + Ri_{conv} + L_{conv}\frac{di_{conv}}{dt} = v_{cap} \tag{5.7}$$

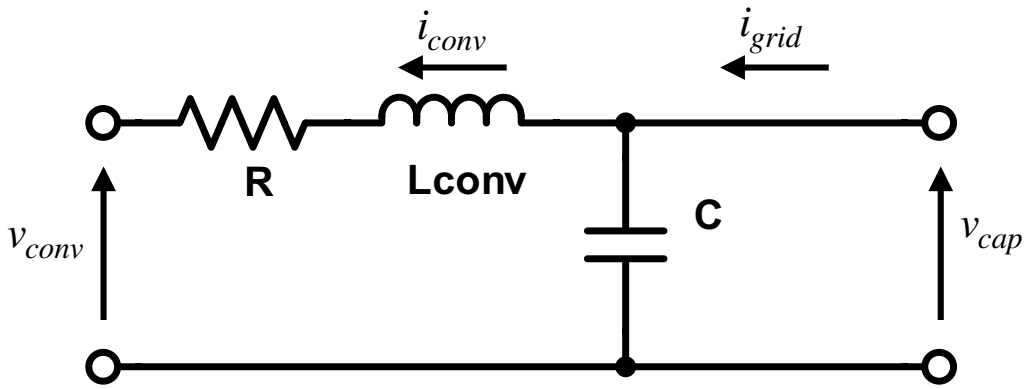


Figure 5.8: Circuit modelled to aid in *Converter 2*'s voltage controller design.

Solving this equation for the derivative term gives equation (5.8).

$$\frac{di_{conv}}{dt} = \frac{v_{cap} - v_{conv} - Ri_{conv}}{L_{conv}} \tag{5.8}$$

The second equation used to describe this circuit can be taken from applying Kirchhoff's current law to the node between the inductor and the capacitor, leading to equation (5.9).

$$C\frac{dv_{cap}}{dt} = i_{grid} - i_{conv} \tag{5.9}$$

Once again, rearranging this last equation to isolate the derivative term leads to equation (5.10).

$$\frac{dv_{cap}}{dt} = \frac{i_{grid} - i_{conv}}{C} \tag{5.10}$$

These equations can now be written in the form of a state equation, having the inductor current $i_{conv}$ and the capacitor voltage $v_{cap}$ as state variables, and grid current $i_{grid}$ and converter voltage $v_{conv}$ as input variables, as in equation (5.11).

$$\begin{bmatrix} \dot{i}_{\text{conv}} \\ \dot{v}_{\text{cap}} \end{bmatrix} = \begin{bmatrix} -\frac{R}{L_{\text{conv}}} & \frac{1}{L_{\text{conv}}} \\ -\frac{1}{C} & 0 \end{bmatrix} \begin{bmatrix} i_{\text{conv}} \\ v_{\text{cap}} \end{bmatrix} + \begin{bmatrix} 0 & \frac{-1}{L_{\text{conv}}} \\ \frac{1}{C} & 0 \end{bmatrix} \begin{bmatrix} i_{\text{grid}} \\ v_{\text{conv}} \end{bmatrix} \tag{5.11}$$

The filter model is then discretized with the zero-order hold method, using MATLAB®function *c2d*, with a 5100 Hz sampling frequency.

A pair of undamped proportional-resonant controllers will be used to control the capacitor voltage in the $\alpha\beta$ coordinates. The discretization used for the resonant controllers is Forward Euler discretization for one of its integrators, and a Backward Euler discretization for the other, or a *Forward-Backward* discretization, shown to have good performance for voltage control in [78], and it's given by the transfer function in equation (5.12), where $h$ is the sampling period and $\omega$, the angular

frequency coming from the turbine and governor model.

$$R_{fb}(z) = \frac{h(z-1)}{z^2 + [(\omega h)^2 - 2]z + 1} \tag{5.12}$$

The complete controller is then given by equation (5.13).

$$C(z) = k_p + k_i R_{fb}(z) \tag{5.13}$$

The system's actuator, the three-phase converter, is modelled as a unit delay with a gain. The unit delay models the fact that a digital control implementation samples the system's measurements, calculates a control effort and applies said control effort in the next sampling instant. This block's gain is the ratio between the fundamental frequency amplitude generated by this type of converter, under a PWM scheme, and the voltage reference amplitude [61]. The converter transfer function is given by equation (5.14).

$$H_{conv}(z) = \frac{1}{2}\frac{v_{dc}}{z} \tag{5.14}$$

The developed linear system model was compared against the converter model in PSCAD™, which uses the same control code which will be embedded in a microcontroller, before closing the control loop, validating the model developed in MATLAB®. Figures 5.9 and 5.10 show the first 100 ms of the $\alpha$ and $\beta$ capacitor voltages, respectively, normalized against the base peak phase voltage, with $k_p = 0$ and $k_i = 201.7$. The grey, sinusoidal, signal was the input signal to the model, a cosine in $\alpha$ and a sine in $\beta$, i.e., a positive sequence, unit amplitude reference.

After closing the control loop in MATLAB®, model sampling was used to pick a set of gains for the voltage controller. Sampling positive, logarithmically spaced proportional gain values suggests that the proportional gain should take negative values instead, as can be seen in the pole-zero plot in figure 5.11. Indeed, sampling negative values of the proportional gain leads to not only stable, but better damped systems than with zero proportional gain. Figure 5.12 shows poles and zeros for combinations of negative proportional gains, logarithmically spaced between -0.1 and -3.16, and positive resonant gains logarithmically spaced between 20 and $200 s^{-1}$.

The set of gains was chosen from the time responses to a cosine input, as shown in figure 5.13. Although this set of gains gives zeros outside the unit circle, corresponding to a non-minimum-phase system, as can be seen from the time response figure, it still locks onto the reference signal to within a 2% error in under one fundamental period, as shown in figure 5.14.

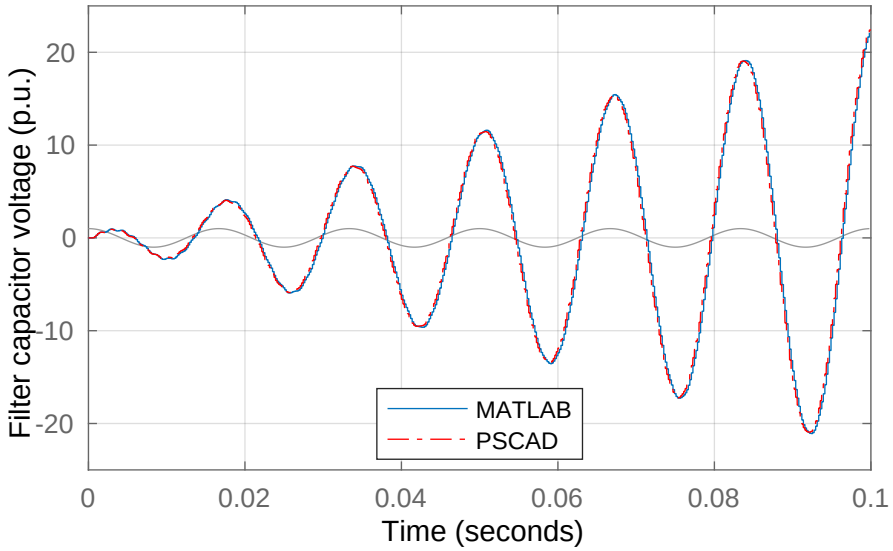


Figure 5.9: Comparison between filter capacitor's $\alpha$ voltage in the MATLAB®model and in the PSCAD™simulation, before closing the voltage control loop. The grey signal is presented in grey, a cosine reference for the $\alpha$ voltage.

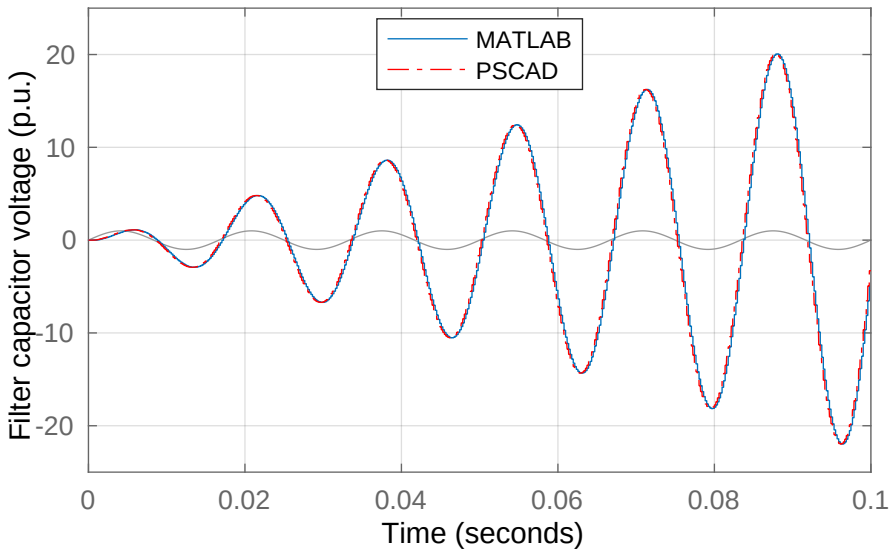


Figure 5.10: Comparison between filter capacitor's $\beta$ voltage in the MATLAB®model and in the PSCAD™simulation, before closing the voltage control loop. The grey signal is presented in grey, a sine reference for the $\beta$ voltage.

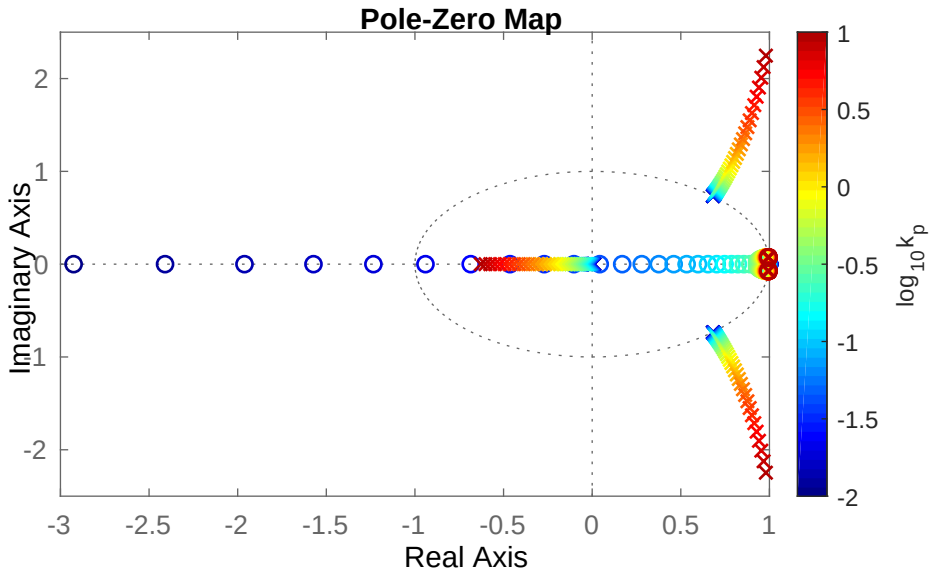


Figure 5.11: Poles and zeros of sampled systems for a proportional gain taking positive values.

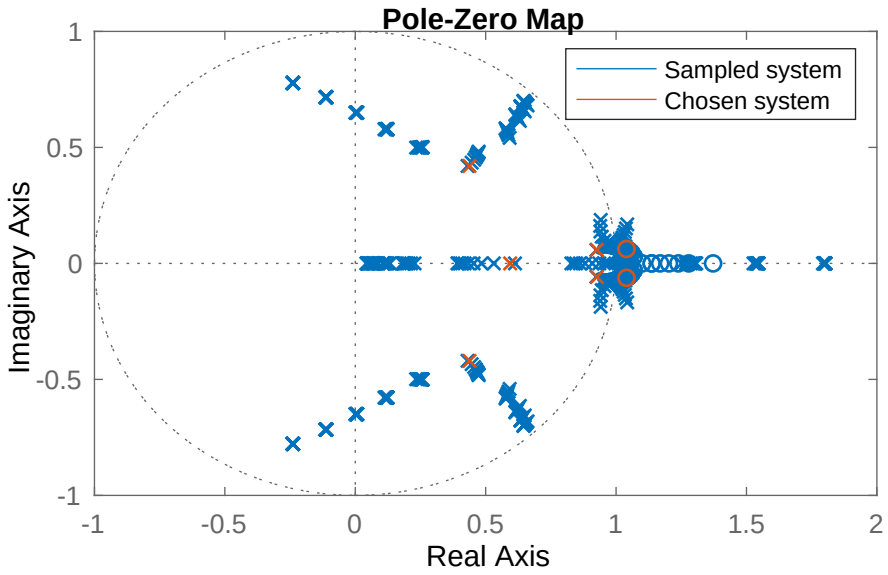


Figure 5.12: Poles and zeros of sampled systems for a proportional gain taking negative values.

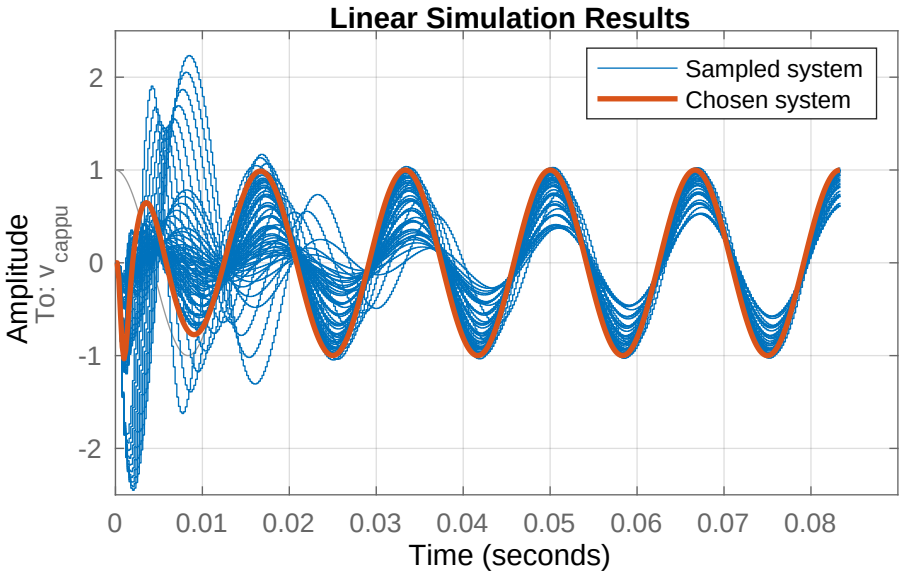


Figure 5.13: Time response, given a cosine, unit amplitude input, of stable sampled systems for negative proportional gains.

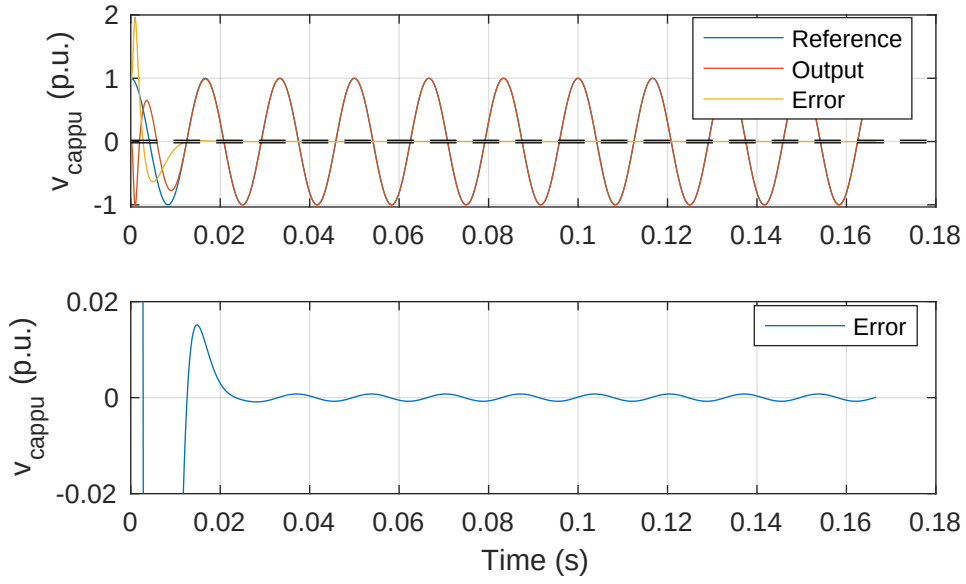


Figure 5.14: Settling time for the error between reference and output signals.

## 5.2 Experimental results

### 5.2.1 Hardware setup

An experimental setup was prepared to test this measurement methodology. The tests were performed on a pair of identical 30 kVA, back-to-back, two-level, IGBT-based, full-bridge converters, shown in figure 5.15. The converters are connected in parallel, with one side only connected to each other and another side connected to the grid, as shown in the diagram in figure 5.16. The converter's three-phase, AC outputs have LCL filters with delta-connected capacitors. Each back-to-back converter's DC link has four 4700 $\mu$F, 450 V, electrolytic capacitors in parallel with four 27 k$\Omega$ resistors, totaling 18.8 mF and is operated at a rated voltage of 405 V, which gives a capacitor inertia constant of $H_C = \frac{1}{2}\frac{Cv_{dcbase}^2}{Pbase} \approx 51.4$ ms.

Figure 5.15: Test rig composed of two back-to-back converters connected in parallel. Also in the picture are the computers used for embedded code loading, debugging and supervision, and the oscilloscope used for all shown measurements, a *Yokogawa DL850EV*.

These converters are controlled by Texas Instruments' F28M35H52C Concerto microcontroller, a dual-core, master/slave system chip. An ARM® Cortex®-M3 serves as a master, communications-oriented, subsystem to a TMS320C28x slave, control-oriented, subsystem. Three-phase voltages are generated through PWM

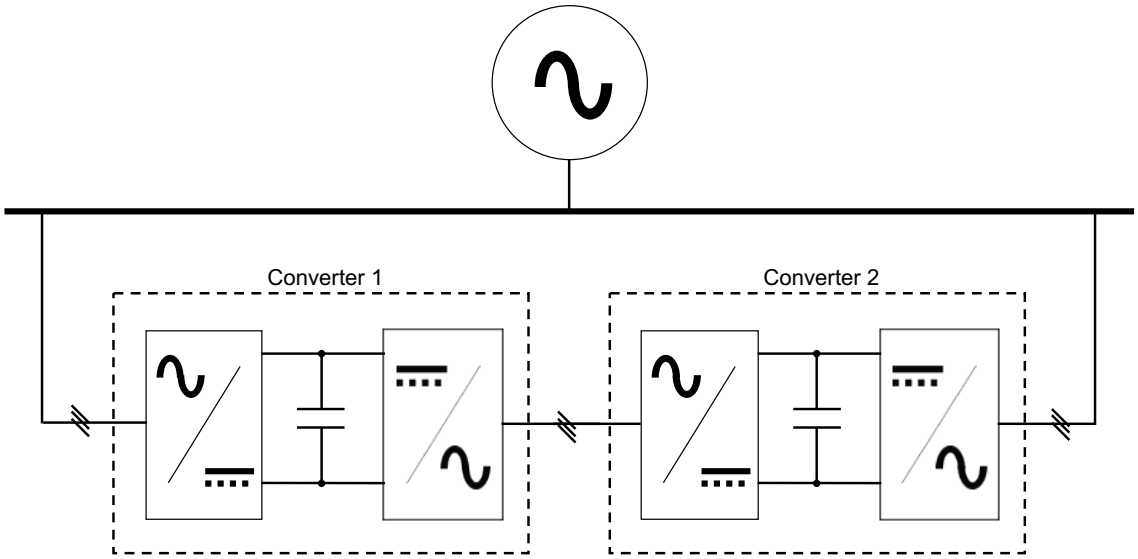


Figure 5.16: Diagram showing connection between back-to-back converters used to test the measurement methodology.

with a 5100 Hz triangle carrier wave and 8 $\mu$s dead time.

### 5.2.2 Hydraulic turbine and governor system emulator

#### Voltage controller behavior

*Converter 2*'s voltage controller was tested in isolated operation and connected to a 6.7 kW (0.22 p.u.). Transient behavior during connection of the same load was also observed. Figure 5.17 shows harmonic components in the converter's output voltage in open circuit operation. It shows a 2.6% Total Harmonic Distortion (THD), composed mainly of second, third, fifth and seventh harmonics. This is expected as there is no harmonic compensation control and dead time, at 8 $\mu$s in this setup, is known to cause non-negligible low order harmonics [79].

When a 22%, three-phase, wye-connected, purely resistive load is connected to the converter output terminal, THD drops to 1.7%, but eleventh and thirteenth harmonics rise, as can be seen in figure 5.18.

Transient behavior can be observed in figure 5.19, which captures the moment of connection of the load. The three-phase line voltages suffer immediately from the load connection, but recover in amplitude well within one cycle of the fundamental period. Some voltage unbalance can be observed in the cycles following connection, and disappears approximately after 7 cycles, or 120 ms.

This behavior is shown in greater detail when calculating a collective three-phase voltage amplitude, given by equation (5.15), in per-unit system. Figure 5.20 shows

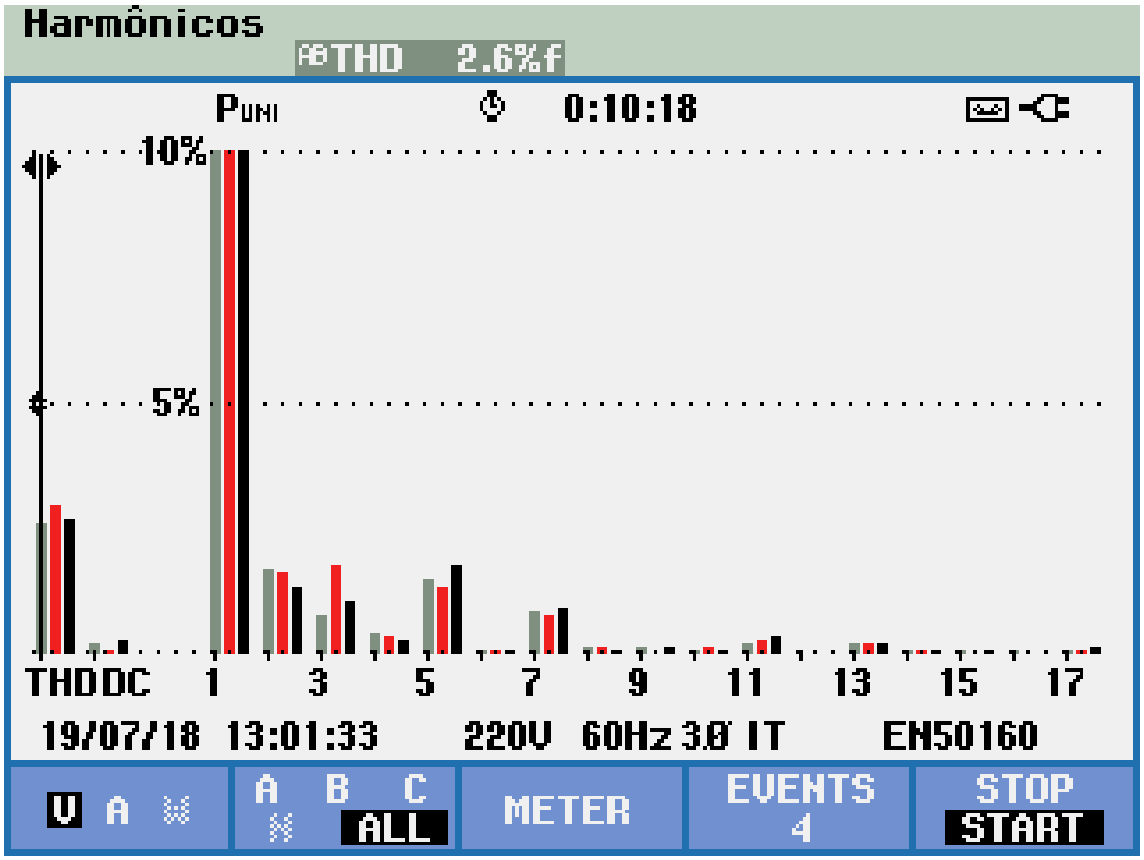


Figure 5.17: Inverter's open-circuit voltage harmonics.

the collective voltage during the event shown in figure 5.19.

$$\bar{V}_{col}(t) = \frac{\sqrt{\frac{2}{3}(V_{ab}(t)^2 + V_{bc}(t)^2 + V_{ca}(t)^2)}}{\sqrt{2}V_{rated,line}} \tag{5.15}$$

### Power disturbance test

A power disturbance test was performed in an open circuit condition, with *Converter 2*'s output terminals open, to verify the converter and the generated voltages' frequency behavior during the test. Figure 5.21 shows the converter performed as expected, reproducing the original transfer function's behavior when a step is applied to its input. Twenty seconds after applying the load step, *Converter 2* goes into the *Recovering* state, leading frequency back to its base value of 60 Hz within two seconds. Finally, it is in *Standby*, ready for another test.

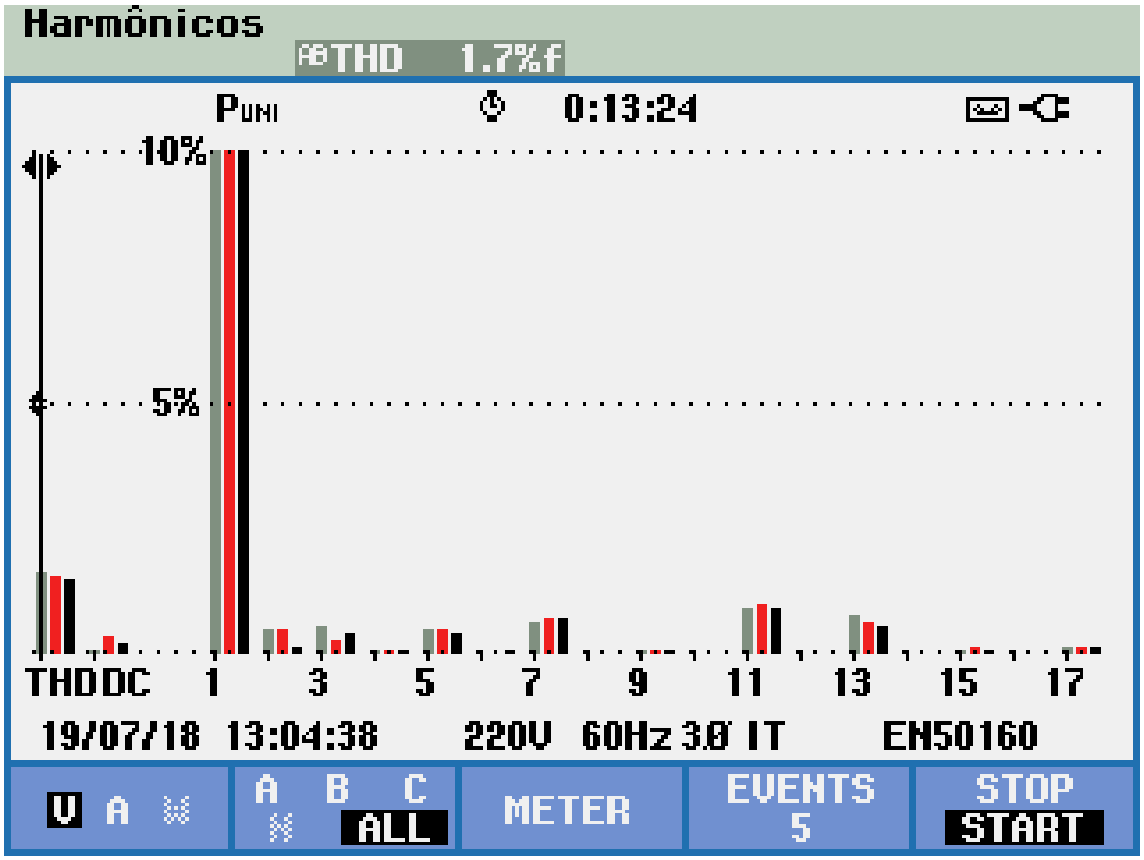


Figure 5.18: Inverter's voltage harmonics when connected to a 6.7 kW load.

### 5.2.3 Load disconnection

A simple load disconnection test was performed to evaluate if the setup and the turbine and governor model were working as expected. If there is a load connected to *Converter 2* before the test begins, disconnecting the load during the test emulates an UFLS scheme, a load disconnection to alleviate a power unbalance.

Figure 5.22 is an oscilloscope screenshot showing two runs at the test, one without any intervention, and another having a 22% load disconnection before the frequency reaches its minimum. The system's original power disturbance was a 5% step, considering a base power 10 times higher that the equipment's. Therefore, in the emulated system's base, there was a 2.2% load disconnection nearly 2 s after the disturbance, corresponding to an alleviation of almost half the original power disturbance. This caused the system frequency to stop falling in under 400 ms and recover to a higher quasi-steady-state frequency than the case with no load disconnection. For this test, therefore, the UFLS action can be characterized, in terms of contribution to grid frequency stability, by the system's response to a standard disturbance, under its influence:

- a frequency nadir of 0.013 p.u., or 0.79 Hz below rated frequency;

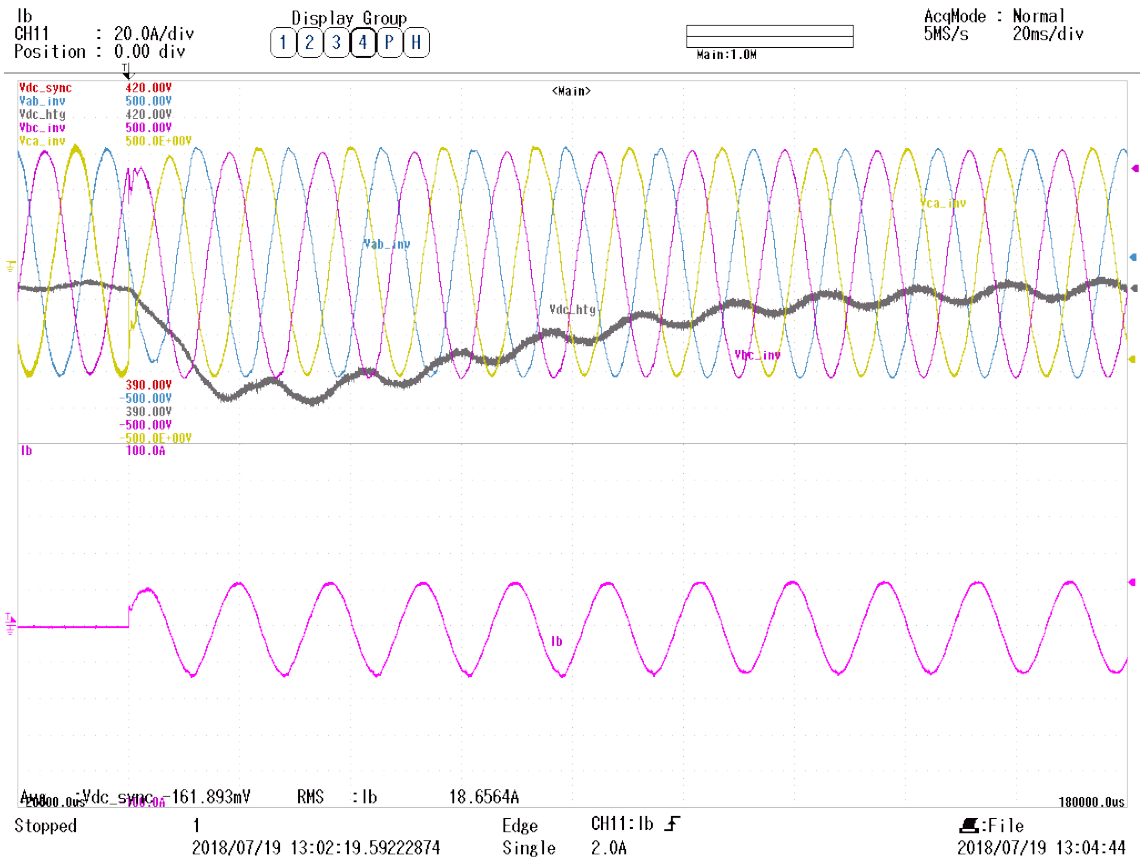


Figure 5.19: Converter 2's voltage controller performance when 6.7 kW three-phase load is connected. Upper window shows output line voltages and DC link voltage; lower window shows line current, highlighting the moment of load connection.

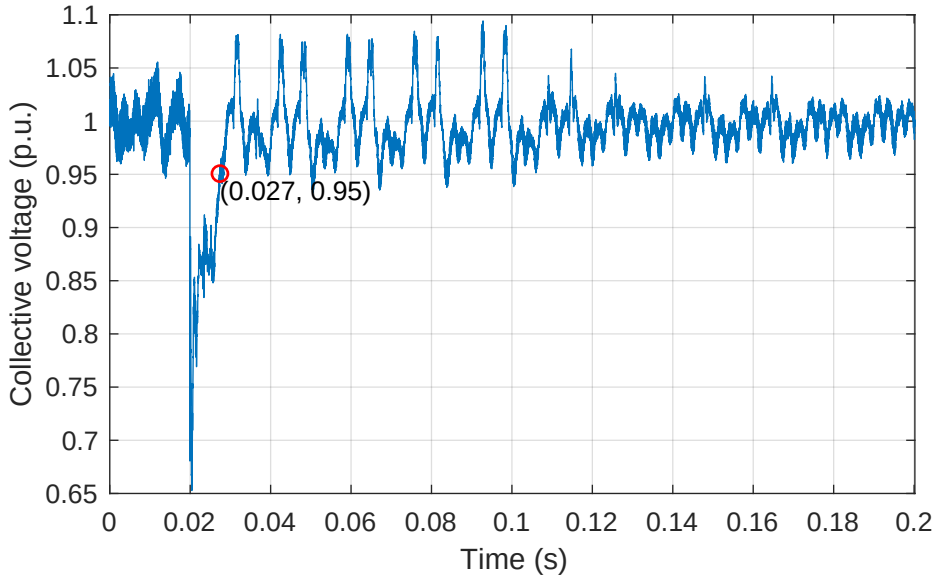


Figure 5.20: Collective voltage behavior on a 22% resistive load connection.

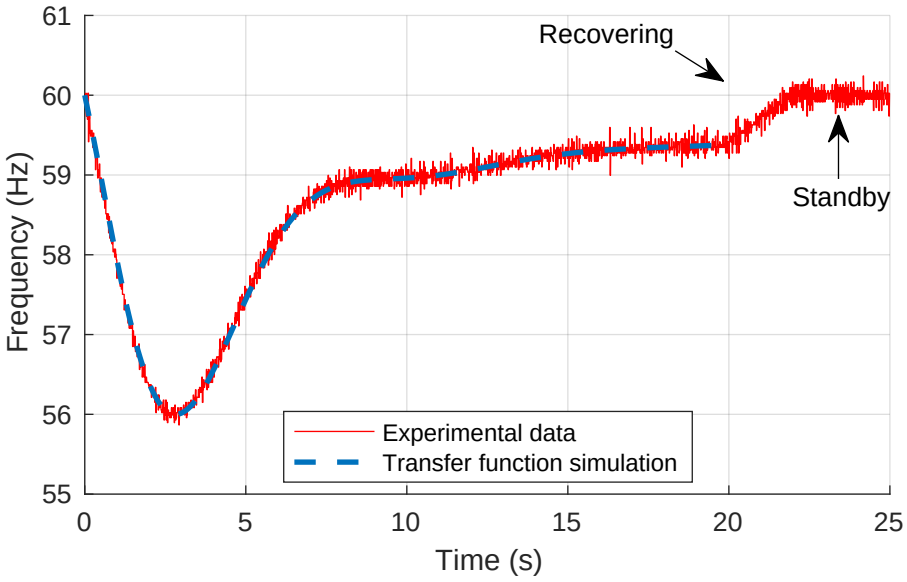


Figure 5.21: Power disturbance test performed with an isolated *Converter 2*, with its output terminals open, and the simulation of the same transfer function in MATLAB®, for a 56 Hz frequency nadir. The experimental data is the equipment's output line voltages' frequency, as calculated by the oscilloscope, a *Yokogawa DL850EV*.

- a frequency nadir difference of 0.22 Hz, i.e., frequency nadir was 0.22 Hz higher than in the case of zero contribution;
- a normalized frequency nadir of 78.3%, where values lower than 100% mean a positive contribution (it represents how much the frequency deviated from rated value, relative to the zero contribution case).
- a 21.7% frequency nadir reduction, i.e., the ratio between frequency nadir difference and the frequency nadir when there is no contribution. This value would normally vary between 0 and 100% for positive contributions, and may be negative if frequency nadir is lower than the isolated system case.

### 5.2.4 Fixed DC link synchronverter

Two synchronverters were implemented: one which assumes a fixed DC link voltage and another one which regulates its own DC link voltage. In the case that the synchronverter assumes a fixed DC link voltage, its back-end converter operates connected to the grid as a current controlled converter and regulates the DC link voltage, as described by the block diagram in figure 5.23.

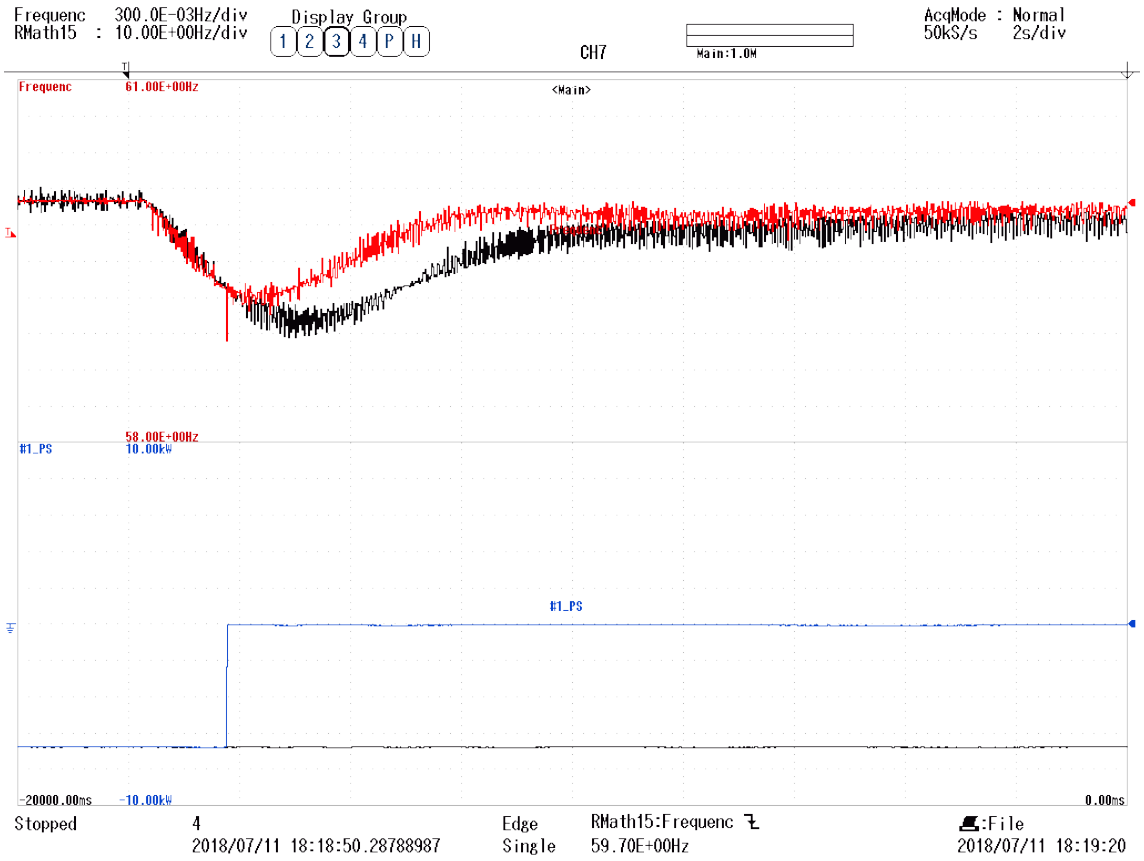


Figure 5.22: Comparison between test with no intervention (in black) and test test with UFLS emulation (in colors). The upper window shows the equipment's output line voltages' frequency. The lower window shows the measured three-phase active power going into *Converter 2*.

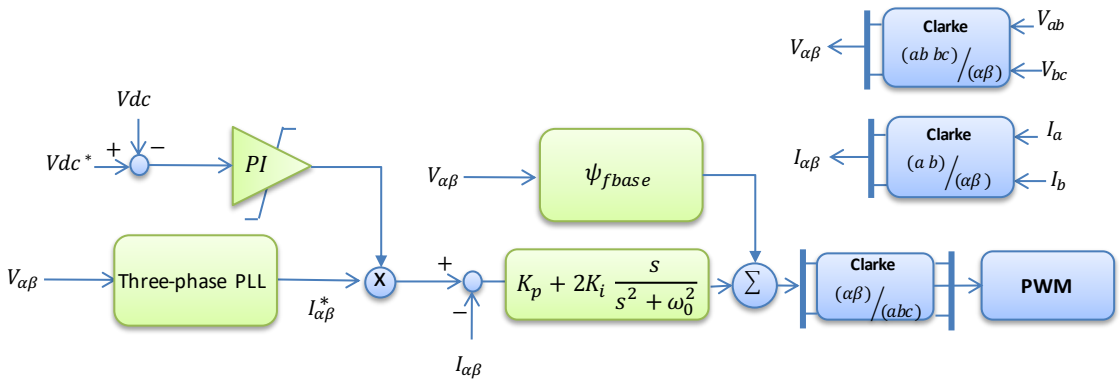


Figure 5.23: Current controller implemented in the back-end converter to regulate DC link voltage.

The implemented synchronverters also regulate its output reactive power, calculated through the instantaneous imaginary power [80], neglecting the current drained by the filter capacitor. I.e., synchronverter powers are calculated from its internal voltage reference and the currents measured on the LCL filter's outer, grid side inductors.

### Synchronization

A Phase-Locked Loop (PLL) was used to provide the synchronverter with its initial virtual rotor speed and phase at the moment of connection. The voltage amplitude at the moment of connection is also measured from length of its $\alpha\beta$ vector, as calculated from the equipment's line voltage measurements, AB and BC, to provide the synchronverter with its initial voltage amplitude, setting the reactive power error integrator's initial output.

When given a command to turn on, the synchronverter updates its initial amplitude, frequency and phase, enables switching signals firing, and commands a contactor to close the circuit, connecting its three-phase output terminal. This procedure minimizes connection transients.

### Power disturbance test

The proposed methodology was able to clearly detect a contribution to grid frequency stability from the 0.3 s virtual inertia synchronverter with fixed DC link, in the form of a reduction in the maximum frequency deviation for the given system disturbance, when compared to the maximum frequency deviation observed when the tester converter is not connected to any other converters. This is observed in figure 5.24, an oscilloscope screenshot containing waveforms from both the test with the synchronverter, in black, and the test for the isolated system, in colors.

Figure 5.25 is a screenshot of the computer running the Code Composer Studio (CCS) debug session used to operate *Converter 2*. It recorded frequency deviation nadir *g_maxFrequencyDeviation_pu* for this test and compared it to a simulated frequency nadir for the isolated system $\Delta\bar{\omega}_{max,isol}$. From these numbers, two more are calculated, as highlighted in the *Expression* window, which contains data read from the microcontroller memory: $g\_normalizedFrequencyNadir = g\_maxFrequencyDeviation\_pu/\Delta\bar{\omega}_{max,isol}$ and $g\_frequencyNadirDifference = 60 \times (g\_maxFrequencyDeviation\_pu - \Delta\bar{\omega}_{max,isol})$. For this test, therefore, the tested converter showed a contribution to frequency stability which can be represented in terms of:

- a frequency nadir of 0.012 p.u., or 0.70 Hz below rated frequency;
- a frequency nadir difference of 0.32 Hz;

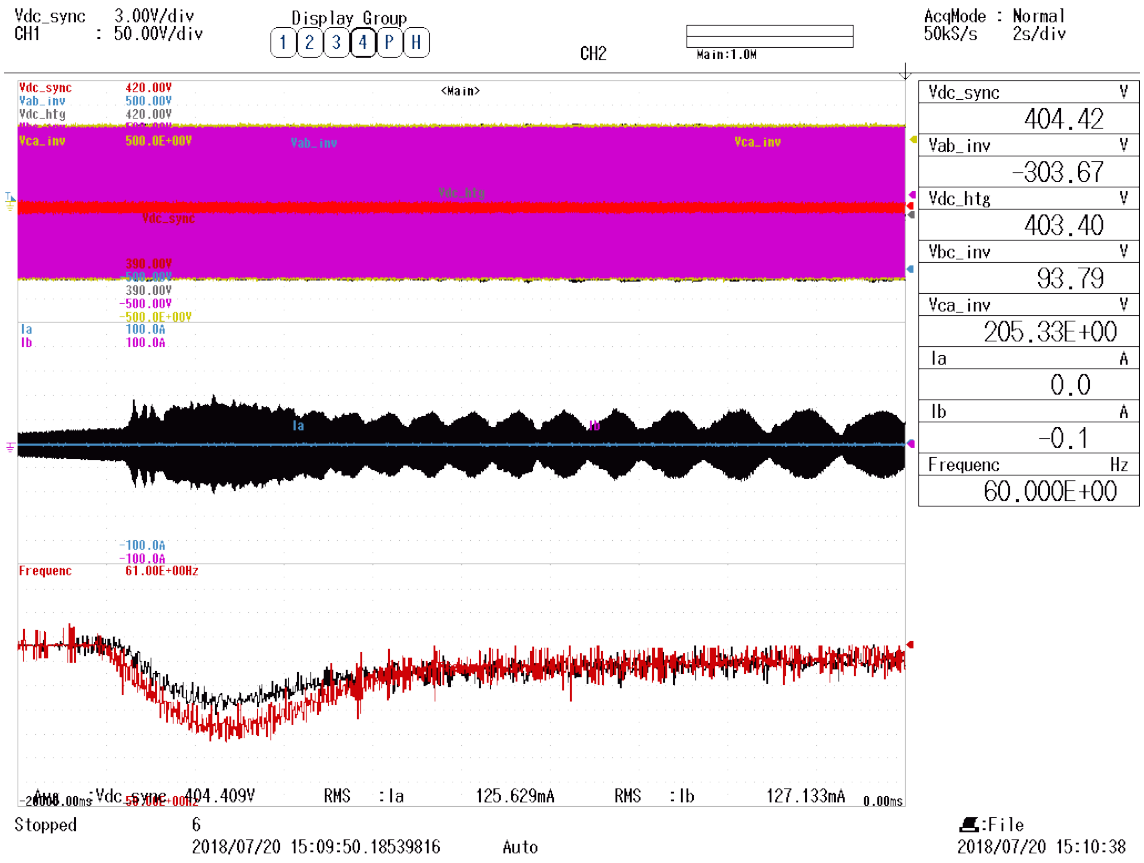


Figure 5.24: Oscilloscope readings of test of the fixed DC link (controlled by a back-end rectifier) synchronverter with a 0.3 s virtual inertia, in black, and test when the synchronverter is disconnected, i.e., the isolated hydraulic turbine and governor system.

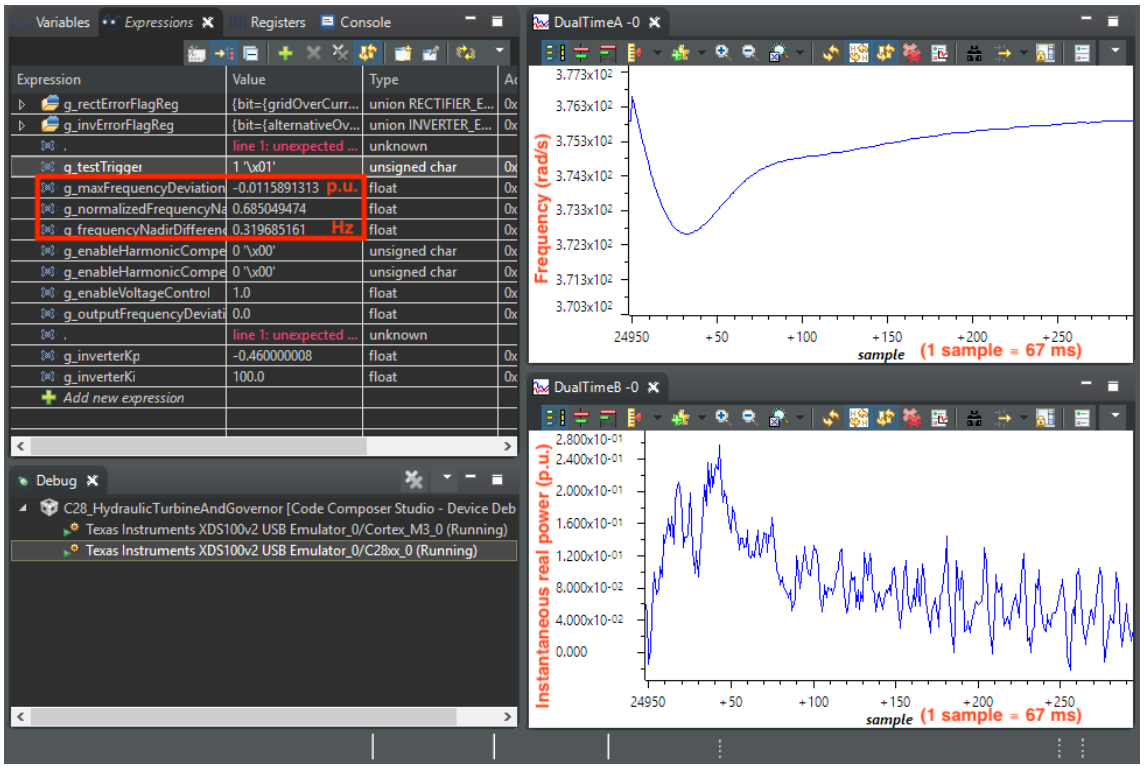


Figure 5.25: CCS's debug view after frequency variation test, showing readings from the microcontroller memory.

- a normalized frequency nadir of 68.5%;
- a 31.5% frequency nadir reduction.

These are all equivalent ways of quantifying the test result.

The same figure further shows plots for the output frequency and for instantaneous real power absorbed during the test that had the synchronverter connected to *Converter 2*. The instantaneous real power shown is the one measured by *Converter 2*, in per-unit system. These values are multiplied by the tester converter's power base, divided by the tested converter's power base and then divided by the intended ratio between power bases for tested converter and emulated turbine and governor system $r_{power}$, as in equation (5.16). Power values that actually serve as input to the turbine and governor model are the deviations $\Delta\bar{p}_g(t)$ from the recorded, filtered input power up until the moment $t_0$ when the test begins, as described by equation (5.17).

$$\bar{p}_g(t) = \bar{p}_{measured}(t)\frac{P_{base,tester}}{P_{base,tested}}\frac{P_{base,tested}}{P_{base,system}} = \frac{\bar{p}_{measured}(t)}{r_{power}}\frac{P_{base,tester}}{P_{base,tested}} \tag{5.16}$$

$$\Delta\bar{p}_g(t) = \bar{p}_g(t) - \bar{p}_g(t_0) \tag{5.17}$$

### 5.2.5 DC link regulating synchronverter

A synchronverter with the same virtual inertia constant as its own capacitor inertia constant shows quite different results if it needs to regulate its own DC link voltage. The tested synchronverter with DC link regulation has an even higher virtual inertia constant, $H_V = 0.3$ s. Indeed, this is expected as the DC link controller tries to stop or compensate any energy flow from the DC link, effectively working against the synchronverter's droop loop, which tries to increase active power output if the system frequency drops. In the previous case this was not a problem, as another power source existed, the back-end converter, and modulated its output in order to keep the DC link regulated without affecting the synchronverter's active power control. Figure 5.26 shows the oscilloscope screen across the 20 s of the test, with a visibly smaller response from the synchronverter. The results recorded by *Converter 2*'s microcontroller can be seen in figure 5.27. For this test, therefore, the tested converter showed a contribution to frequency stability which can be represented in terms of:

- a frequency nadir of 0.017 p.u., or 1.00 Hz below rated frequency;
- a frequency nadir difference of 0.01 Hz;
- a normalized frequency nadir of 99.0%;
- a 1.0% frequency nadir reduction.

### 5.2.6 Static synchronous machine

A static synchronous machine was programmed into *Converter 1*'s front-end, with its back-end operating as a current controlled, DC link regulating grid-tied converter. It uses the same back-end controller as described in figure 5.23, except for the integral part in the DC link controller. The DC link control implemented the same droop curve as is usually implemented for grid frequency control, a proportional gain of 20 (so a 5% DC link voltage deviation causes a 100% active power deviation), with no integral controller. It should be noted that the DC link control operates with an integral part before the front-end connection, so as to have its DC link voltage, and therefore its angular speed, be 1 p.u. at the moment of connection, when the integral control is immediately turned off (the input to the integral part of the controller is forced to be zero).

The synchronization procedure is as implemented for the synchronverter, explained in section 5.2.4. That is, a PLL sets the DC link voltage integrator's initial output so that the initial phase angle matches the grid's. The reactive power integrator, which gives the generated voltage amplitude, has its initial output set to match the grid's voltage amplitude.


Figure 5.26: Oscilloscope readings of test of the DC link regulating synchronverter with a 0.3 s virtual inertia, $k_p = 2.7$ and $k_i = 3\ s^{-1}$. Synchronverter DC link voltage and AC line voltages on the top window, A and B line currents on the middle window, and system frequency on the bottom window.

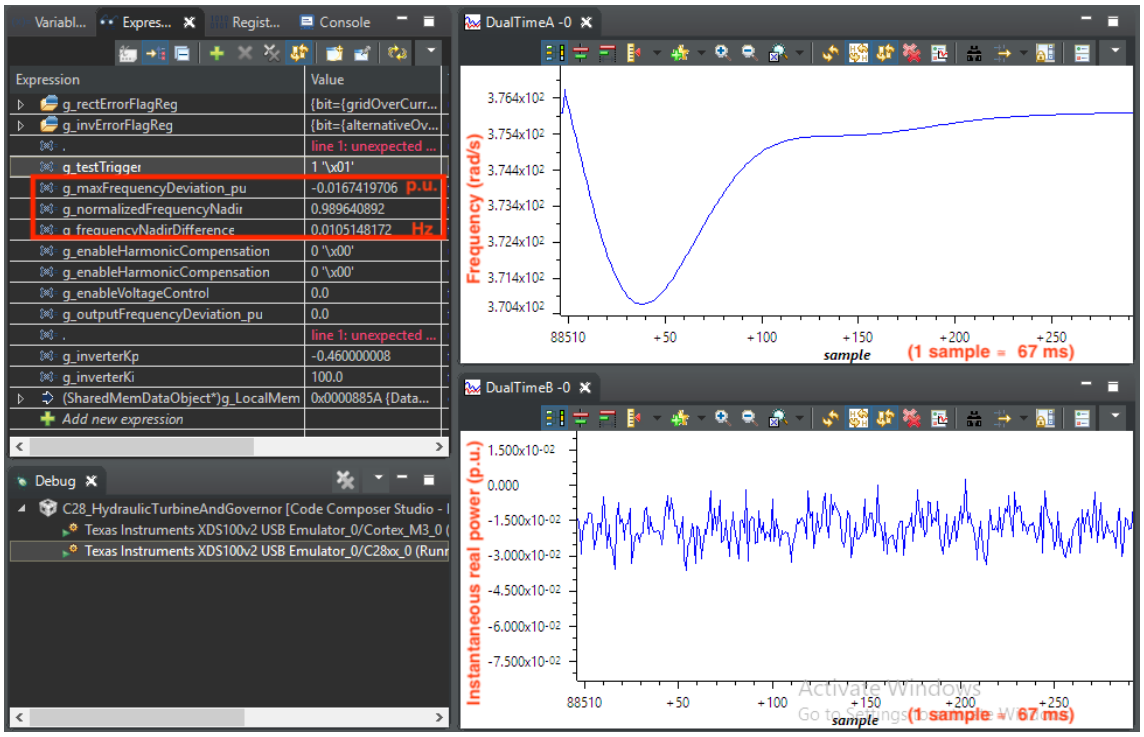


Figure 5.27: CCS's debug view after power disturbance test, showing readings from the microcontroller memory.

### Proof of concept

The static synchronous machine was successfully connected to the grid, as shown in figure 5.28. It maintained continuous, stable operation in this condition for over three minutes.

The next step was to connect the static synchronous machine to a load. Figure 5.29 shows an oscilloscope screenshot encompassing the moments of load connection and disconnection. One can observe the correlation between measured frequency and DC link voltage, hard-coded into the static synchronous machine controller, as they swing during load connection and disconnection.

On load connection, oscilloscope readings show frequency spiking over 61 Hz. In fact, data collected from figure 5.29 give constant frequency readings of $\tilde{1}36.5$ Hz during the fundamental cycle following load connection. Figure 5.30 shows this was in fact just a frequency measurement glitch, as there were no changes to line voltages behavior in this period, except for a decrease in amplitude.

### Power disturbance test

A power disturbance test was performed in the static synchronous machine controlled converter. Results are shown in figures 5.31 and 5.32. For this test, therefore, the tested converter showed a contribution to frequency stability which can be represented in terms of:

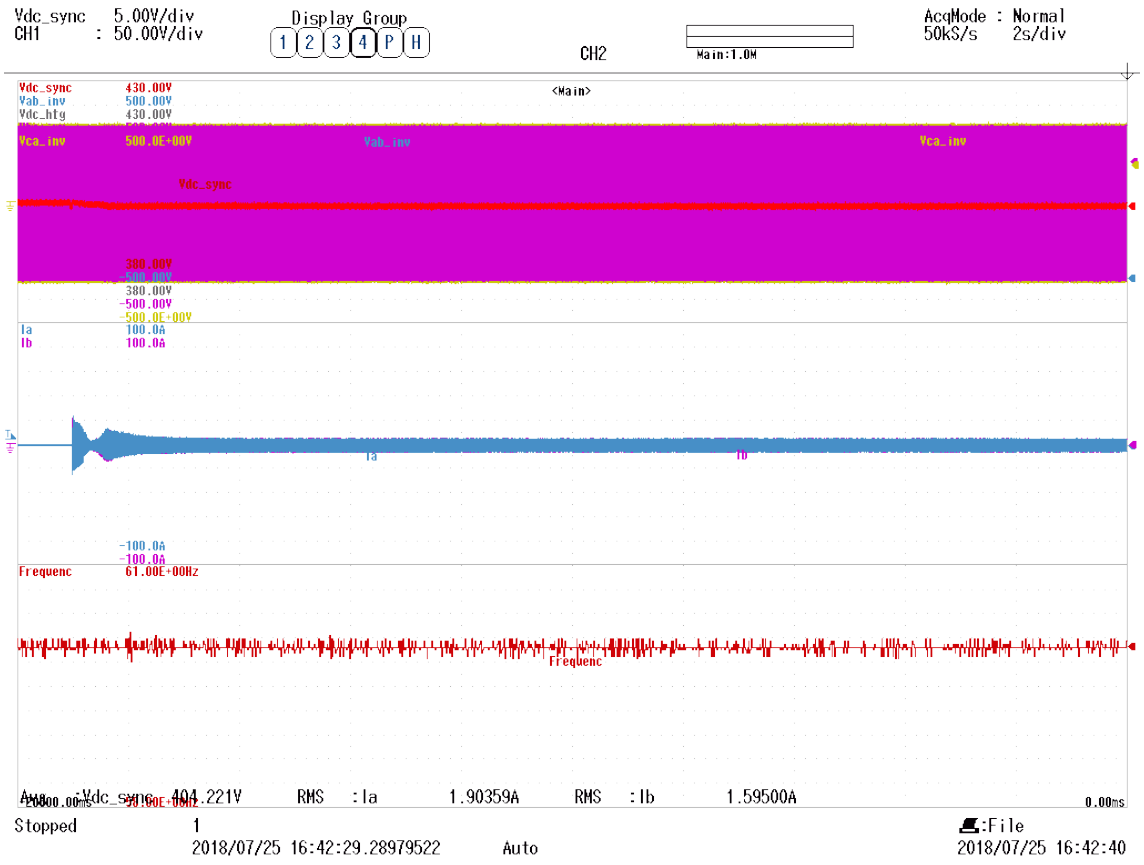


Figure 5.28: Moment of SSM connection to the grid and associated transients, small for line currents and imperceptible for DC link voltage.

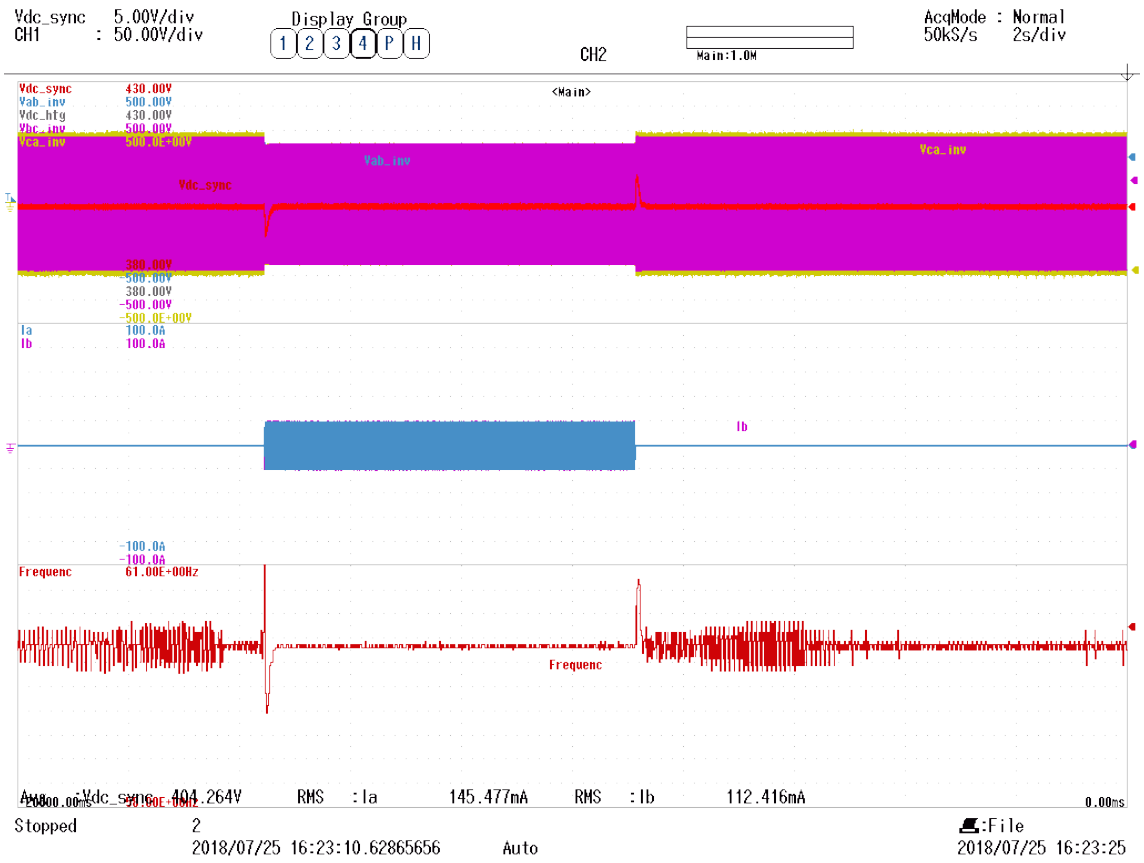


Figure 5.29: Oscilloscope screeschot of the moment a load was connected and then disconnected from *Converter 1*, which was operating as a static synchronous machine.

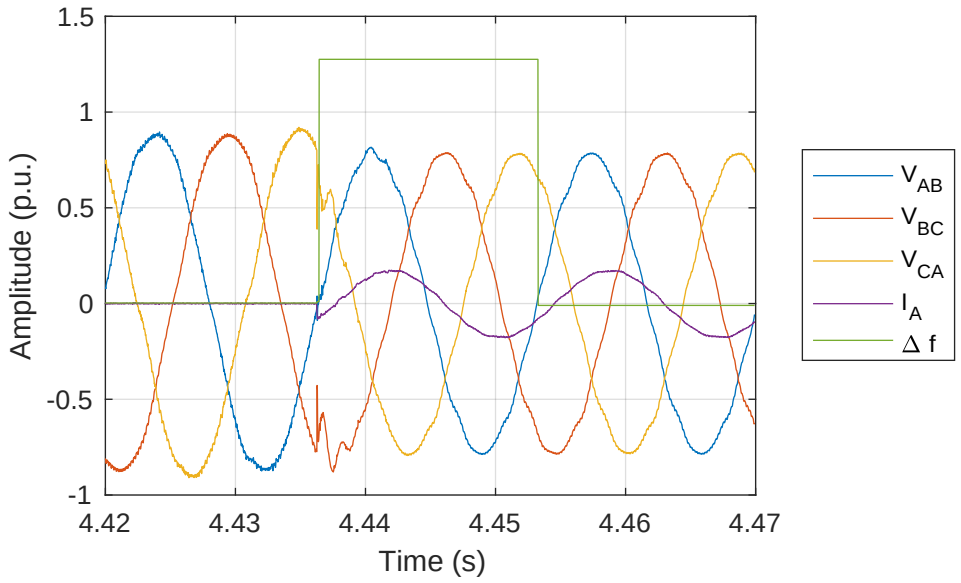


Figure 5.30: Detail of the moment the load is connected to *Converter 1*, which was operating as a static synchronous machine.


Figure 5.31: Oscilloscope readings of test of the static synchronous machine. *Converter 1* DC link voltage and AC line voltages on the top window, A and B line currents on the middle window, and system frequency on the bottom window.

- a frequency nadir of 0.011 p.u., or 0.68 Hz below rated frequency;
- a frequency nadir difference of 0.33 Hz;
- a normalized frequency nadir of 67.2%;
- a 32.8% frequency nadir reduction.

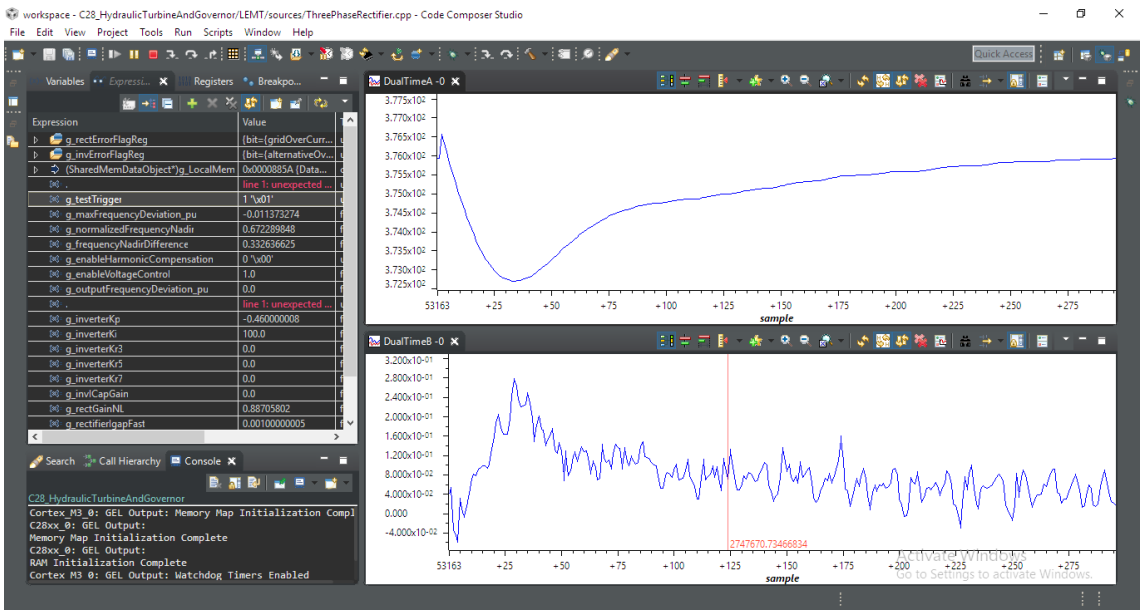


Figure 5.32: CCS's debug view after static synchronous machine power disturbance test, showing readings from the microcontroller memory.

### 5.2.7 Test batteries

Test batteries were executed, consisting of 40 cycles of the load disturbance test, separated by 3 seconds between test cycles. The load step amplitude was such that a 4 Hz frequency deviation, to a 56 Hz frequency nadir, was obtained if *Converter 2* had its terminal in open circuit, if the LFC model receives no power from an additional generating unit, besides its own primary controller. Base power ratio was set to 2, so that measured instantaneous real power deviation is halved before being fed into the embedded LFC model, meaning the LFC model's base power is considered to be twice the base power of the tested generating unit.

Decreasing the base power ratio increases frequency nadir's sensitivity to the tested generating unit's response. High correlations between results across different base power ratios, presented in section 4.2.2, mean it is possible to take advantage of the higher sensitivity of a lower base power ratio with little compromise in applicability of measured contribution to other system sizes.

Confidence intervals at 99% for mean frequency nadir and mean ROCOF (calculated as average ROCOF until the moment of frequency nadir) were calculated for each control strategy, for a single set of parameters. These computations approximated measurement standard deviation by the measured values' standard deviation (i.e. took the sample standard deviation for the population standard deviation), considered to be a valid approximation for sample sizes over 30 [81]. A 99% confidence coefficient means there is a 99% probability that a measured confidence interval will encompass the population's true mean value.

Synchronverter droop constants were kept at $D_p = 1/0.05 = 20$. All tested *Converter 1* controllers additionally regulated their output instantaneous imaginary power with zero reference. Error between measured and reference imaginary power pass through a unit gain integrator whose output is the output voltage amplitude.

### Isolated case

The isolated case is measured by opening the breaker on *Converter 2*'s output terminals and running a test. In this situation, the converter is only connected to its output LCL filter. The standard deviations on measurements such as this, when comparing to previous results shown, is expected to decrease due to the decrease in base power ratio.

A test battery was performed and frequency nadir values were recorded for each test. The standard deviation among 40 recorded frequency nadir samples was $60.5 \times 10^{-6}$ p.u. or 3.63 mHz. That represents a 76% reduction in standard deviation when compared to previous results, obtained before implementation of the power filter documented in figure 5.8 and for the 5% load step amplitude, base power ratio 10 case. An oscilloscope screenshot encompassing the complete test battery is shown in figure 5.33. It is possible to observe the series of tests and, in detail, the varying voltage frequency as a load step is applied to the LFC model. Twenty seconds later, the test is complete, frequency is driven back to its base value within two seconds in a ramp, and the converters are allowed to settle for three seconds, before another test begins.

Measured confidence intervals at 99% are as stated below:

- Frequency deviation nadir: $-3.9996 \pm 0.0015$ Hz;
- Normalized frequency nadir difference (reduction in frequency nadir): $(0.022 \pm 0.037)\%$;
- Mean ROCOF: $-1.4172 \pm 0.0016$ Hz/s;
- Normalized mean ROCOF difference (reduction in mean ROCOF): $(-0.02 \pm 0.11)\%$.

Confidence intervals for reduction in frequency nadir and mean ROCOF are compatible with an isolated measurement, with no contribution provided through *Converter 2*'s three phase terminals. A hypothesis of zero reduction in frequency nadir is accepted under a statistical $Z$-test for confidence coefficients as low as approximately 88%, i.e., a $p$-value of 0.12. The $p$-value for the hypothesis of a zero reduction in mean ROCOF is 0.60. High $p$-values mean collected data don't support rejection of the hypothesis under test. A typical threshold below which a hypothesis is rejected is a $p$-value of 0.05. Rejection of these hypotheses would mean this methodology presented biased measurements of reduction in frequency nadir and reduction in mean ROCOF, as measurements would, on average, be different from the true values for reduction in frequency nadir and reduction in mean ROCOF, necessarily zero in the isolated case.

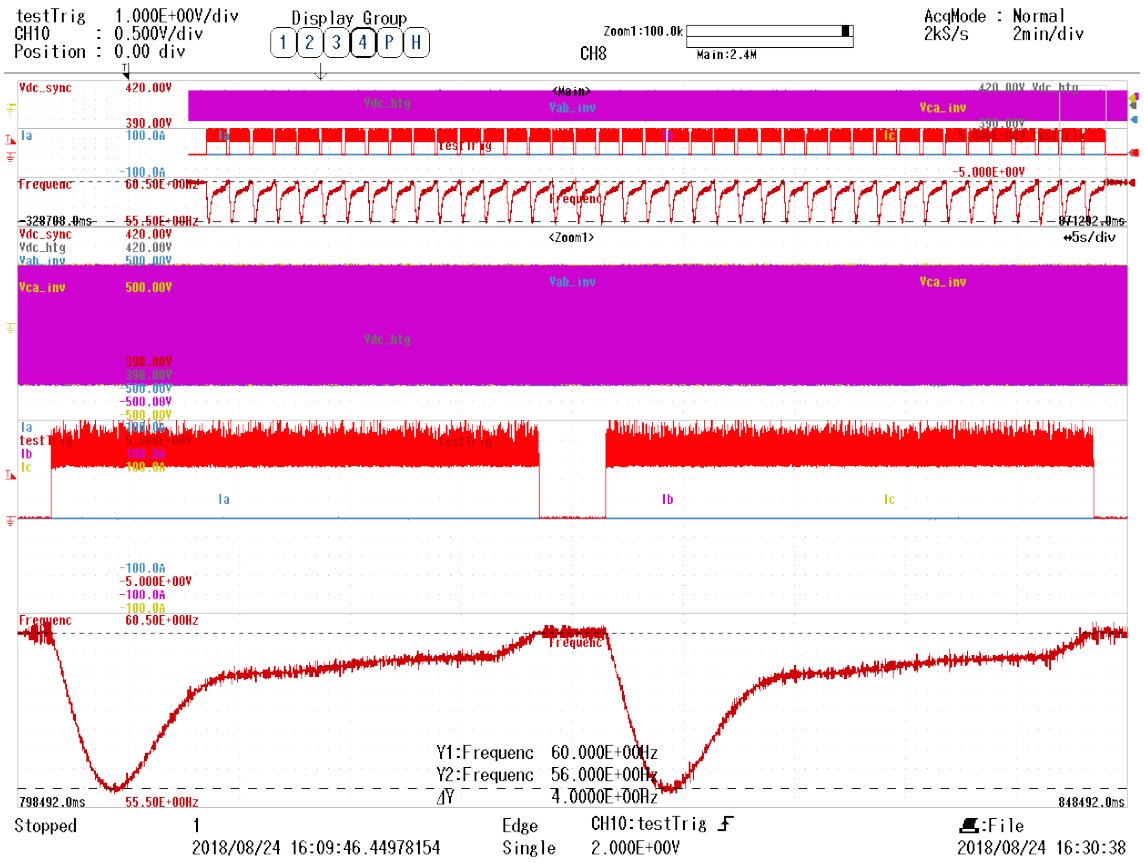


Figure 5.33: Oscilloscope screenshot showing the isolated test battery. The oscilloscope screen is divided in three upper, 2 min/div windows for a test battery overview and three lower, 5 s/div windows for detailed views of single tests. Each trio of windows has AC line and DC voltages (*Vdc_sync* is *Converter 1*'s DC link voltage, *Vdc_htg* is *Converter 2*'s) on the upper window, AC currents and a test trigger signal on the middle window, and AC voltage frequency on the lower window.

### DC link regulating synchronverter

The DC link regulating synchronverter was tested with $k_p = 3.3$, $k_i = 3\ \mathrm{s}^{-1}$ and $H_V = H_C \approx 51.4$ ms. The oscilloscope screenshot for the DC link regulating synchronverter test battery is shown in figure 5.34. The effect of the DC link controller is visible through the currents' behaviors in the middle window, as they climb when frequency starts dropping and and subside in under 6 seconds, approximately. *Converter 1* DC link voltage (*Vdc_sync*) varies greatly, approximately between 345 and 435 V.

Measured confidence intervals at 99% are as stated below:

- Frequency deviation nadir: $-4.0354 \pm 0.0021$ Hz;
- Normalized frequency nadir difference (reduction in frequency nadir): $(-0.873 \pm 0.052)\%$;
- Mean ROCOF: $-1.4234 \pm 0.0018$ Hz/s;
- Normalized mean ROCOF difference (reduction in mean ROCOF): $(-0.46 \pm 0.12)\%$.

### Fixed DC link synchronverter

The synchronverter without DC link control was tested with $H_V = H_C \approx 51.4$ ms. Its back-end converter controlled DC link voltage with a PI controller with proportional gain $k_p = 7$ and integral gain $k_i = 120\ \mathrm{s}^{-1}$. The oscilloscope screenshot for the DC link regulating synchronverter test battery is shown in figure 5.35. AC currents climb with frequency drop and persist, declining slowly as frequency returns to 60 Hz. *Converter 1* DC link voltage (*Vdc_sync*) is kept well regulated at 405 V, as its control is being performed by *Converter 1*'s grid-tied, current controlled back-end converter.

Measured confidence intervals at 99% are as stated below:

- Frequency deviation nadir: $-1.1543 \pm 0.0045$ Hz;
- Normalized frequency nadir difference (reduction in frequency nadir): $(71.15 \pm 0.11)\%$;
- Mean ROCOF: $-0.852 \pm 0.018$ Hz/s;
- Normalized mean ROCOF difference (reduction in mean ROCOF): $(39.8 \pm 1.2)\%$.

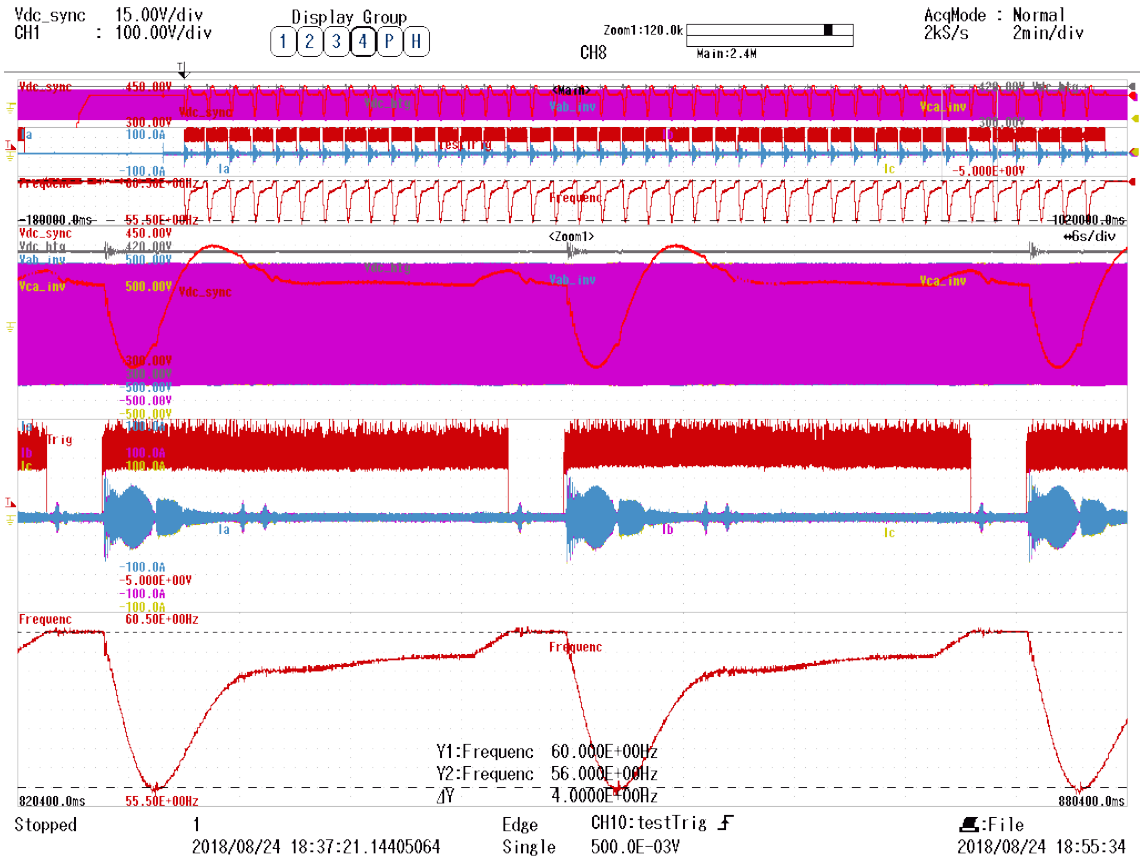


Figure 5.34: Oscilloscope screenshot showing the test battery for the synchronverter with DC link regulation. The oscilloscope screen is divided in three upper, 2 min/div windows for a test battery overview and three lower, 5 s/div windows for detailed views of single tests. Each trio of windows has AC line and DC voltages ( *Vdc_ sync* is *Converter 1*'s DC link voltage, *Vdc_ htg* is *Converter 2*'s) on the upper window, AC currents and a test trigger signal on the middle window, and AC voltage frequency on the lower window.

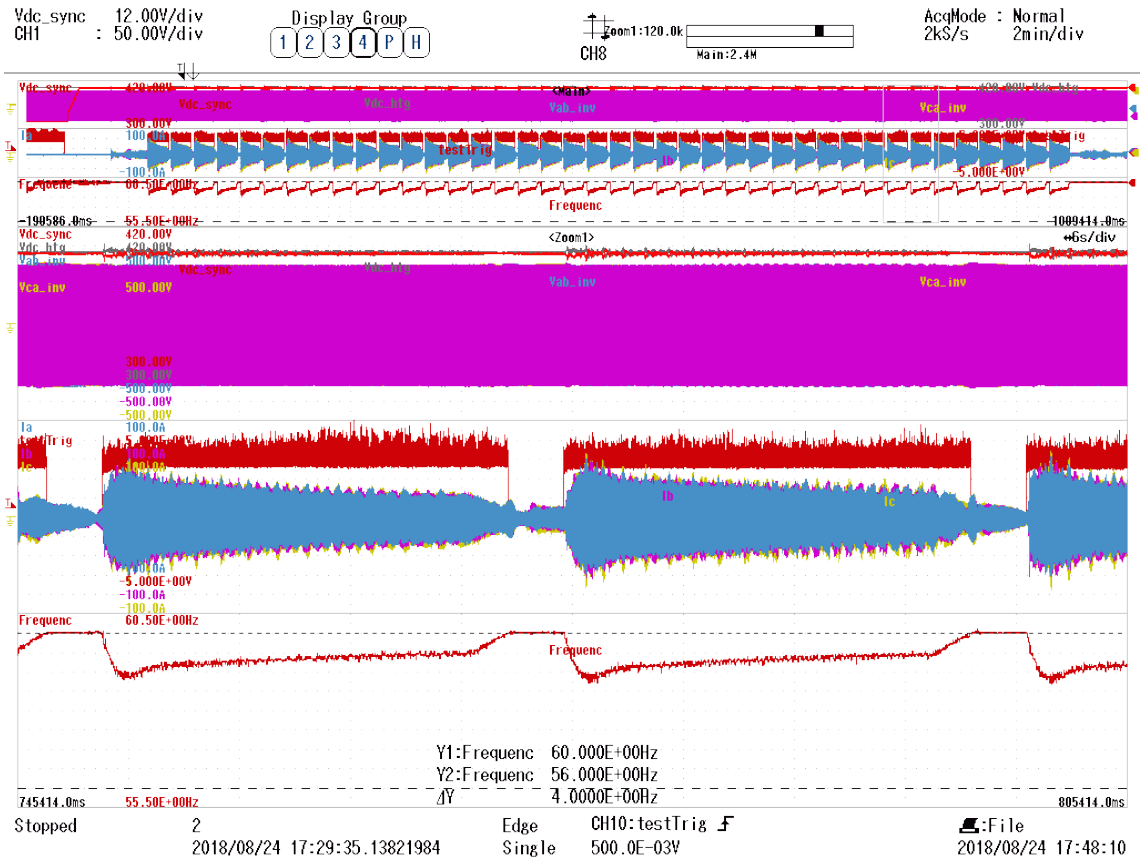


Figure 5.35: Oscilloscope screenshot showing the test battery for the synchronverter with DC link regulated independently by a back-end converter. The oscilloscope screen is divided in three upper, 2 min/div windows for a test battery overview and three lower, 5 s/div windows for detailed views of single tests. Each trio of windows has AC line and DC voltages (*Vdc_sync* is *Converter 1*'s DC link voltage, *Vdc_htg* is *Converter 2*'s) on the upper window, AC currents and a test trigger signal on the middle window, and AC voltage frequency on the lower window.

### Static synchronous machine

The static synchronous machine was tested with its back-end converter controlling DC link voltage with $k_p = 1/0.05 = 20$, a 5% droop. The oscilloscope screenshot for the DC link regulating synchronverter test battery is shown in figure 5.36. AC currents show a similar behavior to the fixed DC link synchronverter AC currents', declining slowly as frequency is restored. Close inspection of *Converter 1*'s DC link voltage shows how it follows the frequency pattern, as would the speed of a synchronous machine.

Measured confidence intervals at 99% are as stated below:

- Frequency deviation nadir: $-1.0599 \pm 0.0088$ Hz;
- Normalized frequency nadir difference (reduction in frequency nadir): $(73.50 \pm 0.22)$%;
- Mean ROCOF: $-0.765 \pm 0.029$ Hz/s;
- Normalized mean ROCOF difference (reduction in mean ROCOF): $(46.0 \pm 2.1)$%.

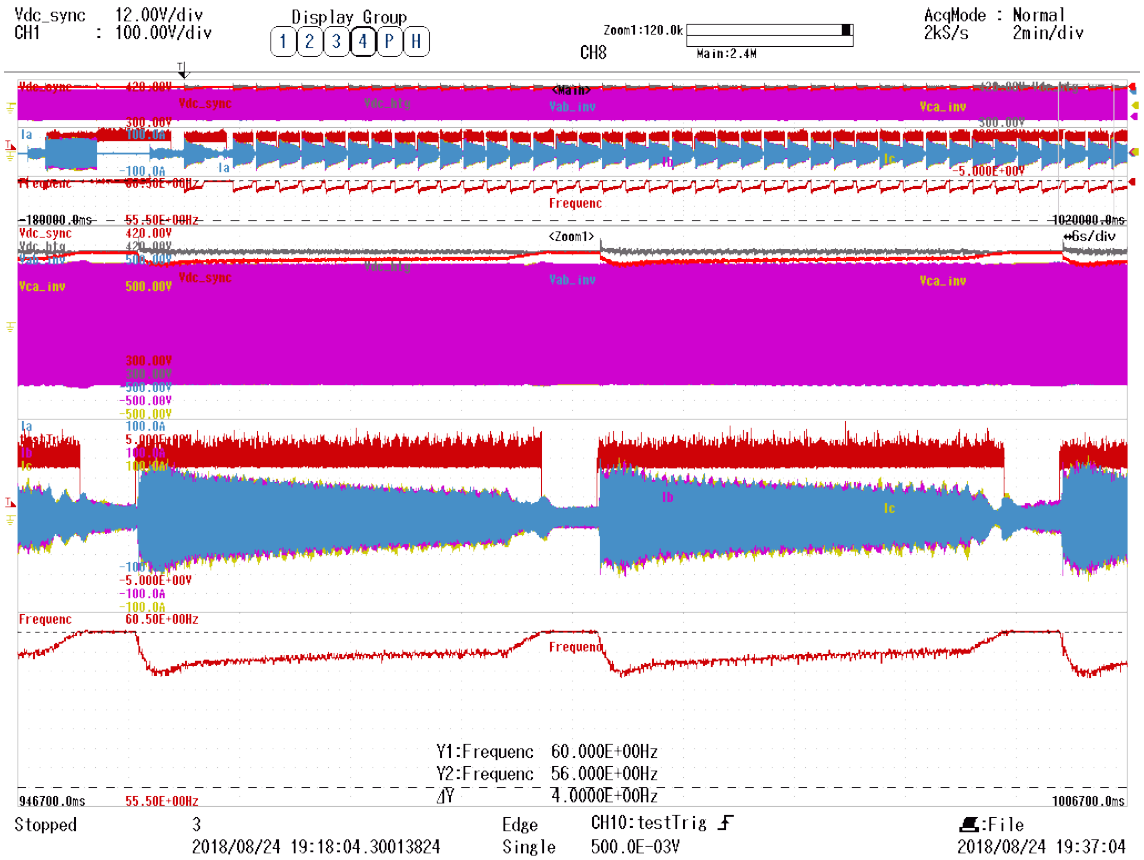


Figure 5.36: Oscilloscope screenshot showing the test battery for the SSM. The oscilloscope screen is divided in three upper, 2 min/div windows for a test battery overview and three lower, 5 s/div windows for detailed views of single tests. Each trio of windows has AC line and DC voltages (*Vdc_sync* is *Converter 1*'s DC link voltage, *Vdc_htg* is *Converter 2*'s) on the upper window, AC currents and a test trigger signal on the middle window, and AC voltage frequency on the lower window.

# Chapter 6

# Conclusions

A methodology for frequency stability contribution measurement has been proposed. The methodology was able to distinguish between control strategies that offer different frequency stability contributions. Test batteries consisting of 40 individual tests, lasting a total of 17 minutes, were able to measure frequency nadir confidence intervals with width as low as 0.78% of the mean measured value. At times when EPS regulations begin to demand frequency stability contribution from wind power plants, this methodology is a way of direct assessment of contribution to system frequency stability.

A new VSC controller, and indeed a converter based generating unit control strategy, was proposed, tested experimentally and its contribution to frequency stability was measured. The SSM is a simple concept which establishes a closer relationship between synchronous machine based generation units and VSC based generation units and may be worthy of further investigation.

Model sampling analysis indicated that the proposed methodology is robust to changes in the LFC model considered as a reference against which to test a target generating unit. There are positive, strong correlations between measured contributions to different LFC models, considering different turbine models and considering different relationships between system base power and generating unit base power.

The proposed methodology allowed for numerical analysis on controller parameters' influence on frequency stability contribution. This was applied to a synchronverter that regulates its own DC link voltage, but whose back-end converter doesn't modulate power output during grid frequency disturbances, to a synchronverter that isn't required to regulate its own DC link voltage, but has its back-end converter do this task, and to a synchronverter that regulates its DC link voltage, but whose back-end converter modulates power output during grid disturbances. This comparison lead to an interesting perspective on the differences between these control strategies.

Furthermore, consideration for primary power sources was made through generic

characteristics: power reserve and time constant for power output modulation. Operation outside the MPP is, in terms of energy costs and power balance, equivalent to having a controllable or switchable dedicated load connected during normal operation. Switching off or modulating load output during disturbances is a way of quickly responding to grid frequency disturbances, bypassing slow WTG governors or solar photovoltaic MPPT algorithms. Already implemented WTG techniques for response to grid frequency disturbances through temporary increase in electromagnetic torque present quicker response time than traditional generation governors. Power reserve and primary power source time response were found to be important characteristics in determining contribution to grid frequency.

Among considered VSC generating unit control strategies, the most suited for realistic applications was found to be the strategy with a front-end converter regulating DC link voltage and a back-end converter modulating power output as much as possible to compensate for grid frequency disturbances. In this scenario, front-end control parameters were found to have negligible effect on contribution to grid frequency stability as long as capacitor inertia constants are low, below 1 s.

## 6.1 Future work

The methodology and the prototype developed for measurement of contribution to frequency stability can be applied to a PV plant once the laboratory's 11 kWp PV plant is operational and a WTG emulator. The PV plant can be used as a test bed for MPPT algorithms, the possibility of operating outside the MPP, and possibly other forms of responding to frequency variation. The WTG emulator, which has the turbine emulated by a converter-driven motor and whose generator may be connected as a Doubly-Fed Induction Generator (DFIG) or through a full converter, can be used as a test bed for different generator control strategies and their effects on contribution to frequency stability.

The availability of a PV plant also enables studying the variability of frequency support by PV plants in terms of weather conditions daily variability. I.e., given daily oscillations in PV power output, how often and how big would the effects be when great changes in power output coincide with disturbances in grid frequency? How long should the test battery be to capture this information?

It would be interesting to study the behavior of the SSM if it is used as the front-end to the PV plant, and as other loads and generations are connected to the DC bus, forming a DC microgrid. Having multiple SSM converters operating in parallel between DC and AC microgrids will allow studies of load sharing and how DC link voltage and generating respond to AC frequency and vice-versa.

# Bibliography


[1] *Procedimentos de Distribuição de Energia Elétrica no Sistema Elétrico Nacional, Módulo 8 – Qualidade da Energia Elétrica.* Agência Nacional de Energia Elétrica (ANEEL), 2016.

[2] *IEEE Standard for Interconnecting Distributed Resources with Electric Power Systems.* IEEE, July 2003.

[3] ARRHENIUS, S., HOLDEN, E. S. "On the Influence of Carbonic Acid in the Air upon the Temperature of the Earth", *Publications of the Astronomical Society of the Pacific*, v. 9, n. 54, pp. 14–24, 1897.

[4] CALLENDAR, G. S. "The artificial production of carbon dioxide and its influence on temperature", *Quarterly Journal of the Royal Meteorological Society*, v. 64, n. 275, pp. 223–240, 1938.

[5] REVELLE, R., SUESS, H. E. "Carbon dioxide exchange between atmosphere and ocean and the question of an increase of atmospheric CO2 during the past decades", *Tellus*, v. 9, n. 1, pp. 18–27, 1957.

[6] BAES, C. F., GOELLER, H. E., OLSON, J. S., et al. "Carbon Dioxide and Climate: The Uncontrolled Experiment: Possibly severe consequences of growing $CO_2$ release from fossil fuels require a much better understanding of the carbon cycle, climate change, and the resulting impacts on the atmosphere", *American Scientist*, v. 65, n. 3, pp. 310–320, 1977. ISSN: 00030996. Available at: <`http://www.jstor.org/stable/27847841`>.

[7] EDENHOFER, O., PICHS-MADRUGA, R., SOKONA, Y., et al. *Special Report on Renewable Energy Sources and Climate Change Mitigation.* United Kingdom and New York, NY, USA, Cambridge University Press, 2011.

[8] REN21. *Renewables 2016 Global Status Report.* Technical report, Renewable Energy Policy Network fo the 21st Century, 2016.

[9] LEVINSON, A. *How much energy do building energy codes really save? Evidence from California.* Technical report, National Bureau of Economic Research, 2014.

[10] COMMISSION, E. "EU Energy in Figures Statistical Pocketbook 2014". 2013.

[11] CHEN, Z., GUERRERO, J. M., BLAABJERG, F. "A Review of the State of the Art of Power Electronics for Wind Turbines", *IEEE Transactions on Power Electronics*, v. 24, n. 8, pp. 1859–1875, Aug 2009. ISSN: 0885-8993. doi: 10.1109/TPEL.2009.2017082.

[12] ACKERMANN, T., ANDERSSON, G., SÖDER, L. "Distributed generation: a definition", *Electric power systems research*, v. 57, n. 3, pp. 195–204, 2001.

[13] MILLER, N., SHAO, M., PAJIC, S., et al. *Western Wind and Solar Integration Study Phase 3–Frequency Response and Transient Stability (Report and Executive Summary).* Technical report, National Renewable Energy Laboratory (NREL), Golden, CO., 2014.

[14] LOPES, J. P., HATZIARGYRIOU, N., MUTALE, J., et al. "Integrating distributed generation into electric power systems: A review of drivers, challenges and opportunities", *Electric power systems research*, v. 77, n. 9, pp. 1189–1203, 2007.

[15] ULBIG, A., BORSCHE, T. S., ANDERSSON, G. "Impact of low rotational inertia on power system stability and operation", *IFAC Proceedings Volumes*, v. 47, n. 3, pp. 7290–7297, 2014.

[16] ULBIG, A., BORSCHE, T. S., ANDERSSON, G. "Analyzing Rotational Inertia, Grid Topology and their Role for Power System Stability", *IFAC-PapersOnLine*, v. 48, n. 30, pp. 541–547, 2015.

[17] TELEGINA, E. *Impact of Rotational Inertia Changes on Power System Stability.* Masters Thesis, Swiss Federal Institute of Technology Zurich, November 2015.

[18] BORSCHE, T. S., LIU, T., HILL, D. J. "Effects of rotational inertia on power system damping and frequency transients". In: *Conference on Decision and Control*, 2015.

[19] TIELENS, P., HERTEM, D. V. "The relevance of inertia in power systems", *Renewable and Sustainable Energy Reviews*, v. 55, pp. 999 – 1009, 2016. ISSN: 1364-0321. doi: http://dx.doi.org/10.1016/j.rser.

2015.11.016. Available at: <http://www.sciencedirect.com/science/article/pii/S136403211501268X>.

[20] POOLLA, B. K., BOLOGNANI, S., DORFLER, F. "Placing Rotational Inertia in Power Grids", *arXiv preprint arXiv:1510.01497*, 2015.

[21] WINTER, W., ELKINGTON, K., BAREUX, G., et al. "Pushing the Limits: Europe's New Grid: Innovative Tools to Combat Transmission Bottlenecks and Reduced Inertia", *IEEE Power and Energy Magazine*, v. 13, n. 1, pp. 60–74, Jan 2015. ISSN: 1540-7977. doi: 10.1109/MPE.2014.2363534.

[22] SOVACOOL, B. K. "The intermittency of wind, solar, and renewable electricity generators: Technical barrier or rhetorical excuse?" *Utilities Policy*, v. 17, n. 3–4, pp. 288 – 296, 2009. ISSN: 0957-1787. doi: http://dx.doi.org/10.1016/j.jup.2008.07.001. Available at: <http://www.sciencedirect.com/science/article/pii/S0957178708000611>.

[23] KATIRAEI, F., AGUERO, J. R. "Solar PV Integration Challenges", *IEEE Power and Energy Magazine*, v. 9, n. 3, pp. 62–71, May 2011. ISSN: 1540-7977. doi: 10.1109/MPE.2011.940579.

[24] TARROJA, B., MUELLER, F., EICHMAN, J. D., et al. "Spatial and temporal analysis of electric wind generation intermittency and dynamics", *Renewable Energy*, v. 36, n. 12, pp. 3424–3432, 2011.

[25] MILLIGAN, M., FREW, B., KIRBY, B., et al. "Alternatives No More: Wind and Solar Power Are Mainstays of a Clean, Reliable, Affordable Grid", *IEEE Power and Energy Magazine*, v. 13, n. 6, pp. 78–87, Nov 2015. ISSN: 1540-7977. doi: 10.1109/MPE.2015.2462311.

[26] *ERCOT Nodal Protocols, Section 8: Performance Monitoring*. Electric Reliability Council of Texas (ERCOT), July 2016.

[27] *ISO Rules Part 500 Facilities Division 502 Technical Requirements Section 502.1 Wind Aggregated Generating Facilities Technical Requirements*. Alberta Electric System Operator (AESO), 2015.

[28] BECK, D. I. H.-P., HESSE, D. I. R. "Virtual synchronous machine". In: *Electrical Power Quality and Utilisation, 2007. EPQU 2007. 9th International Conference on*, pp. 1–6. IEEE, 2007.

[29] DRIESEN, J., VISSCHER, K. "Virtual synchronous generators". In: *Power and Energy Society General Meeting-Conversion and Delivery of Electrical Energy in the 21st Century, 2008 IEEE*, pp. 1–3. IEEE, 2008.

[30] ZHONG, Q.-C., WEISS, G. "Static synchronous generators for distributed generation and renewable energy". In: *Power Systems Conference and Exposition, 2009. PSCE'09. IEEE/PES*, pp. 1–6. IEEE, 2009.

[31] ZHONG, Q. C., WEISS, G. "Synchronverters: Inverters that mimic synchronous generators", *Industrial Electronics, IEEE Transactions on*, v. 58, n. 4, pp. 1259–1267, 2011.

[32] D'ARCO, S., SUUL, J. A., FOSSO, O. B. "Control system tuning and stability analysis of Virtual Synchronous Machines". In: *Energy Conversion Congress and Exposition (ECCE), 2013 IEEE*, pp. 2664–2671. IEEE, 2013.

[33] D'ARCO, S., SUUL, J. A. "Virtual synchronous machines—Classification of implementations and analysis of equivalence to droop controllers for microgrids". In: *PowerTech (POWERTECH), 2013 IEEE Grenoble*, pp. 1–7. IEEE, 2013.

[34] KUNDUR, P., PASERBA, J., AJJARAPU, V., et al. "Definition and classification of power system stability IEEE/CIGRE joint task force on stability terms and definitions", *IEEE Transactions on Power Systems*, v. 19, n. 3, pp. 1387–1401, Aug 2004. ISSN: 0885-8950. doi: 10.1109/TPWRS.2004.825981.

[35] *Gerenciamento da Carga para Controle de Frequência no Sistema*. Operador Nacional do Sistema Elétrico (ONS), 2017.

[36] *Requisitos técnicos mínimos para a conexão às instalações de transmissão*. Operador Nacional do Sistema Elétrico (ONS), 12 2016.

[37] *Gerenciamento Da Carga Por Atuação Do ERAC*. Operador Nacional do Sistema Elétrico (ONS), 2017.

[38] *IEEE Application Guide for IEEE Std 1547(TM), IEEE Standard for Interconnecting Distributed Resources with Electric Power Systems*. IEEE, April 2009.

[39] UCTE. *UCTE Operation Handbook Appendix 1: Load-Frequency Control and Performance*. UCTE, June 2004.

[40] *Controle da geração*. Operador Nacional do Sistema Elétrico (ONS), 12 2016.

[41] BOEMER, J., BURGES, K., NABE, C., et al. *All Island TSO Facilitation of Renewables Studies*. Technical report, EirGrid and SONI, 2010.

[42] MILLER, N., CLARK, K., SHAO, M. "Impact of frequency responsive wind plant controls on grid performance". In: *Proceedings of the 9th Annual Large-Scale Integration of Wind Power into Power Systems and Transmission Networks for Offshore Wind Power Plant, Quebec, Canada*, 2010.

[43] RODRIGUEZ, P., CANDELA, I., CITRO, C., et al. "Control of grid-connected power converters based on a virtual admittance control loop". In: *Power Electronics and Applications (EPE), 2013 15th European Conference on*, pp. 1–10, Sept 2013. doi: 10.1109/EPE.2013.6634621.

[44] D'ARCO, S., SUUL, J. A. "Equivalence of virtual synchronous machines and frequency-droops for converter-based microgrids", *Smart Grid, IEEE Transactions on*, v. 5, n. 1, pp. 394–395, 2014.

[45] VASQUEZ, J. C., GUERRERO, J. M., LUNA, A., et al. "Adaptive droop control applied to voltage-source inverters operating in grid-connected and islanded modes", *Industrial Electronics, IEEE Transactions on*, v. 56, n. 10, pp. 4088–4096, 2009.

[46] ZHONG, Q. C., BOROYEVICH, D. "A droop controller is intrinsically a phase-locked loop". In: *Industrial Electronics Society, IECON 2013 - 39th Annual Conference of the IEEE*, pp. 5916–5921, Nov 2013. doi: 10.1109/IECON.2013.6700105.

[47] SAO, C. K., LEHN, P. W. "Autonomous load sharing of voltage source converters", *Power Delivery, IEEE Transactions on*, v. 20, n. 2, pp. 1009–1016, 2005.

[48] PIAGI, P., LASSETER, R. H. "Autonomous control of microgrids". In: *Power Engineering Society General Meeting, 2006. IEEE*, pp. 8–pp. IEEE, 2006.

[49] DE BRABANDERE, K., BOLSENS, B., VAN DEN KEYBUS, J., et al. "A voltage and frequency droop control method for parallel inverters", *Power Electronics, IEEE Transactions on*, v. 22, n. 4, pp. 1107–1115, 2007.

[50] GUERRERO, J. M., VASQUEZ, J. C., MATAS, J., et al. "Control strategy for flexible microgrid based on parallel line-interactive UPS systems", *Industrial Electronics, IEEE Transactions on*, v. 56, n. 3, pp. 726–736, 2009.

[51] EDRIS, A. A. "Proposed terms and definitions for flexible AC transmission system (FACTS)", *IEEE Transactions on Power Delivery*, v. 12, n. 4, pp. 1848–1853, Oct 1997. ISSN: 0885-8977. doi: 10.1109/61.634216.

[52] RODRIGUEZ, P., CANDELA, I., LUNA, A. "Control of PV generation systems using the synchronous power controller". In: *2013 IEEE Energy Conversion Congress and Exposition*, pp. 993–998, Sept 2013. doi: 10.1109/ECCE.2013.6646811.

[53] REMON, D., CANTARELLAS, A. M., RAKHSHANI, E., et al. "An active power self-synchronizing controller for grid-connected converters emulating inertia". In: *Renewable Energy Research and Application (ICRERA), 2014 International Conference on*, pp. 424–429. IEEE, 2014.

[54] REMON, D., CANTARELLAS, A. M., ELSAHARTY, M. A. A., et al. "Synchronous PV support to an isolated power system". In: *2015 IEEE Energy Conversion Congress and Exposition (ECCE)*, pp. 1982–1987, Sept 2015. doi: 10.1109/ECCE.2015.7309940.

[55] CONROY, J. F., WATSON, R. "Frequency Response Capability of Full Converter Wind Turbine Generators in Comparison to Conventional Generation", *IEEE Transactions on Power Systems*, v. 23, n. 2, pp. 649–656, May 2008. ISSN: 0885-8950. doi: 10.1109/TPWRS.2008.920197.

[56] ZHANG, L., HARNEFORS, L., NEE, H.-P. "Power-synchronization control of grid-connected voltage-source converters", *Power Systems, IEEE Transactions on*, v. 25, n. 2, pp. 809–820, 2010.

[57] XIONG, L., ZHUO, F., WANG, F., et al. "Static Synchronous Generator Model: A New Perspective to Investigate Dynamic Characteristics and Stability Issues of Grid-Tied PWM Inverter", *IEEE Transactions on Power Electronics*, v. 31, n. 9, pp. 6264–6280, Sept 2016. ISSN: 0885-8993. doi: 10.1109/TPEL.2015.2498933.

[58] KUNDUR, P., BALU, N. J., LAUBY, M. G. *Power system stability and control*, v. 7. New York, McGraw-hill New York, 1994.

[59] REPORT, I. C. "Dynamic Models for Steam and Hydro Turbines in Power System Studies", *IEEE Transactions on Power Apparatus and Systems*, v. PAS-92, n. 6, pp. 1904–1915, Nov 1973. ISSN: 0018-9510. doi: 10.1109/TPAS.1973.293570.

[60] FRANÇA, B. W., DE CASTRO, A. R., AREDES, M. "Wind and photovoltaic power generation integrated to power grid through dc link and synchronverter". In: *2015 IEEE 13th Brazilian Power Electronics Conference and 1st Southern Power Electronics Conference (COBEP/SPEC)*, pp. 1–6, Nov 2015. doi: 10.1109/COBEP.2015.7420216.

[61] MOHAN, N., UNDELAND, T. M. *Power electronics: converters, applications, and design*. New Jersey, John Wiley & Sons, 2007.

[62] HOLMES, D. G., LIPO, T. A. "Modulation of Three-Phase Voltage Source Inverters". In: *Pulse Width Modulation for Power Converters: Principles and Practice*, cap. 5, pp. 215–258, Piscataway, New Jersey, IEEE, 2003. doi: 10.1109/9780470546284.ch5. Available at: <`https://ieee.proxy.ufrj.br/xpl/articleDetails.jsp?arnumber=5311949`>.

[63] PARK, R. H. "Two-reaction theory of synchronous machines generalized method of analysis-part I", *Transactions of the American Institute of Electrical Engineers*, v. 48, n. 3, pp. 716–727, 1929.

[64] PARK, R. "Two-reaction theory of synchronous machines-II", *Transactions of the American Institute of Electrical Engineers*, v. 52, n. 2, pp. 352–354, 1933.

[65] FRIEDMAN, J. H. "Greedy Function Approximation: A Gradient Boosting Machine", *The Annals of Statistics*, v. 29, n. 5, pp. 1189–1232, 2001. ISSN: 00905364. Available at: <`http://www.jstor.org/stable/2699986`>.

[66] HASTIE, T., TIBSHIRANI, R., FRIEDMAN, J. *The Elements of Statistical Learning*. Springer Series in Statistics. 2 ed. New York, NY, Springer-Verlag New York, 2009. doi: 10.1007/978-0-387-84858-7.

[67] GOLDSTEIN, A., KAPELNER, A., BLEICH, J., et al. "Peeking Inside the Black Box: Visualizing Statistical Learning With Plots of Individual Conditional Expectation", *Journal of Computational and Graphical Statistics*, v. 24, n. 1, pp. 44–65, 2015. doi: 10.1080/10618600.2014.907095. Available at: <`https://doi.org/10.1080/10618600.2014.907095`>.

[68] FEMIA, N., GRANOZIO, D., PETRONE, G., et al. "Predictive & Adaptive MPPT Perturb and Observe Method", *IEEE Transactions on Aerospace and Electronic Systems*, v. 43, n. 3, pp. 934–950, July 2007. ISSN: 0018-9251. doi: 10.1109/TAES.2007.4383584.

[69] CLARK, K., WALLING, R. A., MILLER, N. W. "Solar photovoltaic (PV) plant models in PSLF". In: *2011 IEEE Power and Energy Society General Meeting*, pp. 1–5, July 2011. doi: 10.1109/PES.2011.6039117.

[70] KILLI, M., SAMANTA, S. "Modified perturb and observe MPPT algorithm for drift avoidance in photovoltaic systems", *IEEE Transactions on Industrial Electronics*, v. 62, n. 9, pp. 5549–5559, 2015. doi: 10.1109/TIE.2015.2407854.

[71] PENG, B., HO, K., LIU, Y. "A Novel and Fast MPPT Method Suitable for Both Fast Changing and Partially Shaded Conditions", *IEEE Transactions on Industrial Electronics*, v. 65, n. 4, pp. 3240–3251, April 2018. ISSN: 0278-0046. doi: 10.1109/TIE.2017.2736484.

[72] QI, J., ZHANG, Y., CHEN, Y. "Modeling and maximum power point tracking (MPPT) method for PV array under partial shade conditions", *Renewable Energy*, v. 66, pp. 337 – 345, 2014. ISSN: 0960-1481. doi: https://doi.org/10.1016/j.renene.2013.12.018. Available at: <http://www.sciencedirect.com/science/article/pii/S0960148113006952>.

[73] ISHAQUE, K., SALAM, Z. "A Deterministic Particle Swarm Optimization Maximum Power Point Tracker for Photovoltaic System Under Partial Shading Condition", *IEEE Transactions on Industrial Electronics*, v. 60, n. 8, pp. 3195–3206, Aug 2013. ISSN: 0278-0046. doi: 10.1109/TIE.2012.2200223.

[74] MORREN, J., DE HAAN, S. W. H., KLING, W. L., et al. "Wind turbines emulating inertia and supporting primary frequency control", *IEEE Transactions on Power Systems*, v. 21, n. 1, pp. 433–434, Feb 2006. ISSN: 0885-8950. doi: 10.1109/TPWRS.2005.861956.

[75] LALOR, G., MULLANE, A., O'MALLEY, M. "Frequency control and wind turbine technologies", *IEEE Transactions on Power Systems*, v. 20, n. 4, pp. 1905–1913, Nov 2005. ISSN: 0885-8950. doi: 10.1109/TPWRS.2005.857393.

[76] CLARK, K., MILLER, N. W., SANCHEZ-GASCA, J. J. "Modeling of GE wind turbine-generators for grid studies", *GE Energy*, v. 4, pp. 0885–8950, 2010.

[77] ÅSTRÖM, K., WITTENMARK, B. *Computer-Controlled Systems: Theory and Design*. Dover Books on Electrical Engineering. 3 ed. New Jersey, NJ, Prentice Hall, 1997. Available at: <https://books.google.com.br/books?id=TynEAgAAQBAJ>.

[78] CASTAÑO, J. E. C. *High Performance Voltage Control For Three-Phase Ups Inverter*. Masters Thesis, Universidade Federal do Rio de Janeiro, 2014.

[79] WU, C. M., LAU, W.-H., CHUNG, H. S.-H. "Analytical technique for calculating the output harmonics of an H-bridge inverter with dead time", *IEEE Transactions on Circuits and Systems I: Fundamental Theory and Applications*, v. 46, n. 5, pp. 617–627, May 1999. ISSN: 1057-7122. doi: 10.1109/81.762927.

[80] AKAGI, H., WATANABE, E. H., AREDES, M. *Instantaneous power theory and applications to power conditioning*, v. 62. Hoboken, New Jersey, John Wiley & Sons, 2017.

[81] LEFEBVRE, M. *Applied Probability and Statistics*. 1 ed. New York, NY, Springer-Verlag New York, 2006. doi: 10.1007/0-387-28505-9.

# Appendix A

# Partial Dependence Plots and Individual Conditional Expectation

This appendix exemplifies the usage of the developed code for PDP and ICE plots through a trivial example. Consider that we have a function of three variables $f(x, y, z)$ and its value is known for the combinations of the following values of its input variables:

```
x = column(1:3);
y = column(4:6);
z = column(7:9);
```

We may generate all possible combinations of its input variables:

```
samplingGrid = makeSamplingGridStructure(...
    'x',x,...
    'y',y,...
    'z',z)
```

Example output values for $f(x, y, z)$ are generated below so that, whenever $y$ and $z$ are held constant, $f(x, y, z)$ becomes a zero-crossing, straight line in terms of $x$. Every different combination of $(y, z)$ gives a different slope.

```
f = zeros(3,3,3);
for i=1:(length(y)*length(z))
    iceOutput = -i:i:i;
    [j,k] = ind2sub([3,3],i);
    f(:,j,k) = iceOutput;
end
```

## A.1 Individual Conditional Expectation

The following code uses the developed ICE plot function to make an ICE plot for $f(x, y, z)$ on variable $x$, shown in figure A.1. Each curve represents a different $(y, z)$ pair. The plot function was provided with a table of $x$ values, a table of $(y, z)$ pairs and a table of the associated $f(x, y, z)$ output values.

```
focusParameterValuesTable = table(samplingGrid.x(:),...
'VariableNames',{'x'});
focusParameterValuesTable.Properties.VariableUnits = ...
{'p.u.'};
focusParameterValuesTable.Properties...
.VariableDescriptions = {'Parameter x'};
parameterSetsTable = table(samplingGrid.y(:),...
samplingGrid.z(:), 'VariableNames',{'y','z'});
parameterSetsTable.Properties.VariableUnits = {'p.u.',...
'p.u.'};
fTable = table(f(:),'VariableNames',{'Output'});
fTable.Properties.VariableUnits = {'p.u.'};
fTable.Properties.VariableDescriptions = {'f(x,y,z)'};
figure;
individualConditionalExpectationPlot(...
focusParameterValuesTable,parameterSetsTable,fTable,'-o');
```

The offset between the curves' first point may be eliminated to highlight the effect of the variable being analyzed. I.e. all curves are shifted vertically so they begin at the same point and each curve shows a different way the variable being analyzed may affect the output. This option is activated by the flag *centered* in the code below. Figure A.2 shows how data from the plot in figure A.1 is presented when the first point's offset is eliminated.

```
figure;
individualConditionalExpectationPlot(...
focusParameterValuesTable,parameterSetsTable,fTable,...
'centered','-o');
```

## A.2 Partial Dependence Plots

Having an Individual Conditional Expectation (ICE) plot, the Partial Dependence Plot (PDP) is simply the mean value, for each value for $x$, over all ICE curves. I.e., a PDP gives the mean output value for each value of a variable that is held

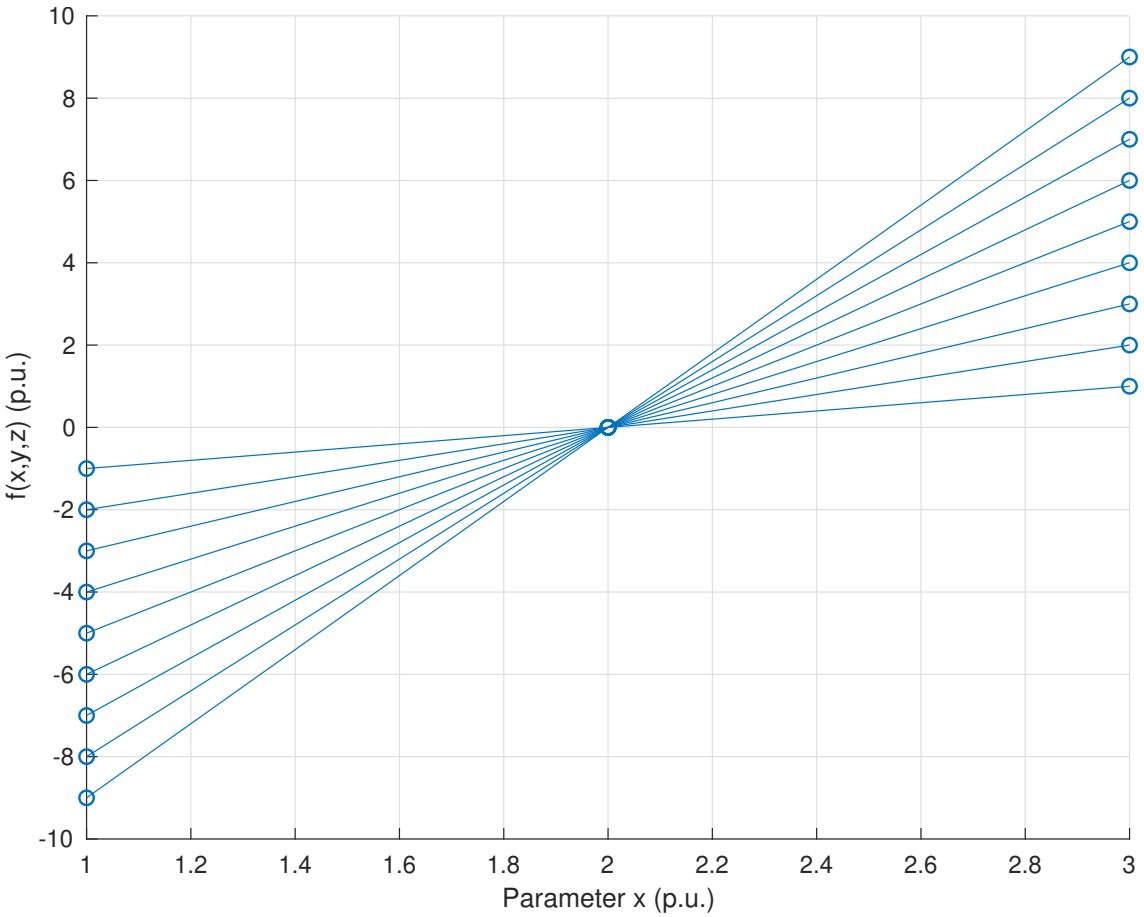


Figure A.1: Individual conditional expectation plot for $f(x, y, z)$ on variable $x$.

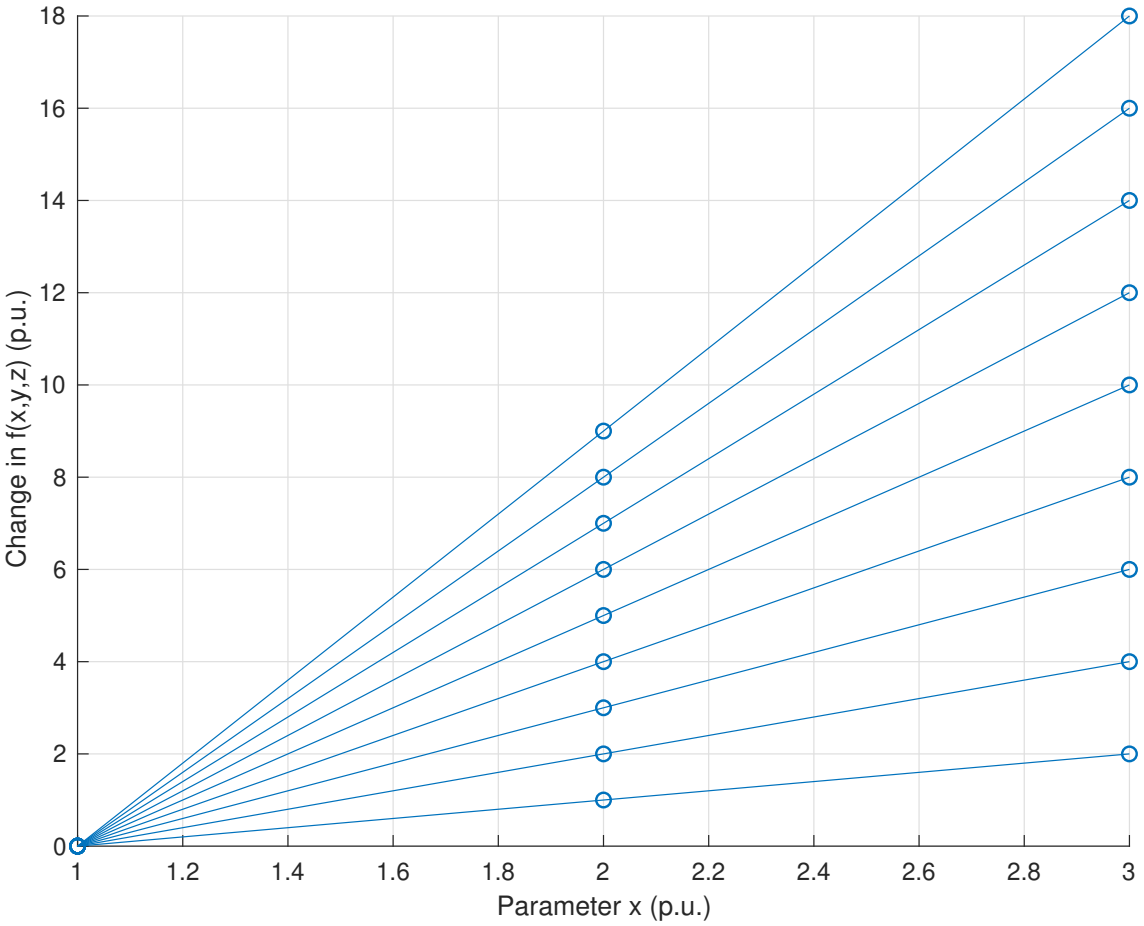


Figure A.2: Individual conditional expectation plot for $f(x, y, z)$ on variable $x$ considering changes from $f(x, y, z)$'s value for the first value considered for $x$.

constant at each plot point ($x$ in this example). The code below uses the flag *includePartialDependencePlot* to include a PDP to the plot shown in figure A.1. It's output is shown in figure A.3.

```
figure;
individualConditionalExpectationPlot(...
focusParameterValuesTable,parameterSetsTable,fTable,...
'includePartialDependencePlot','-o');
```

A PDP plot may also be used with the *centered* option. The code below exemplifies this, as shown in figure A.4.

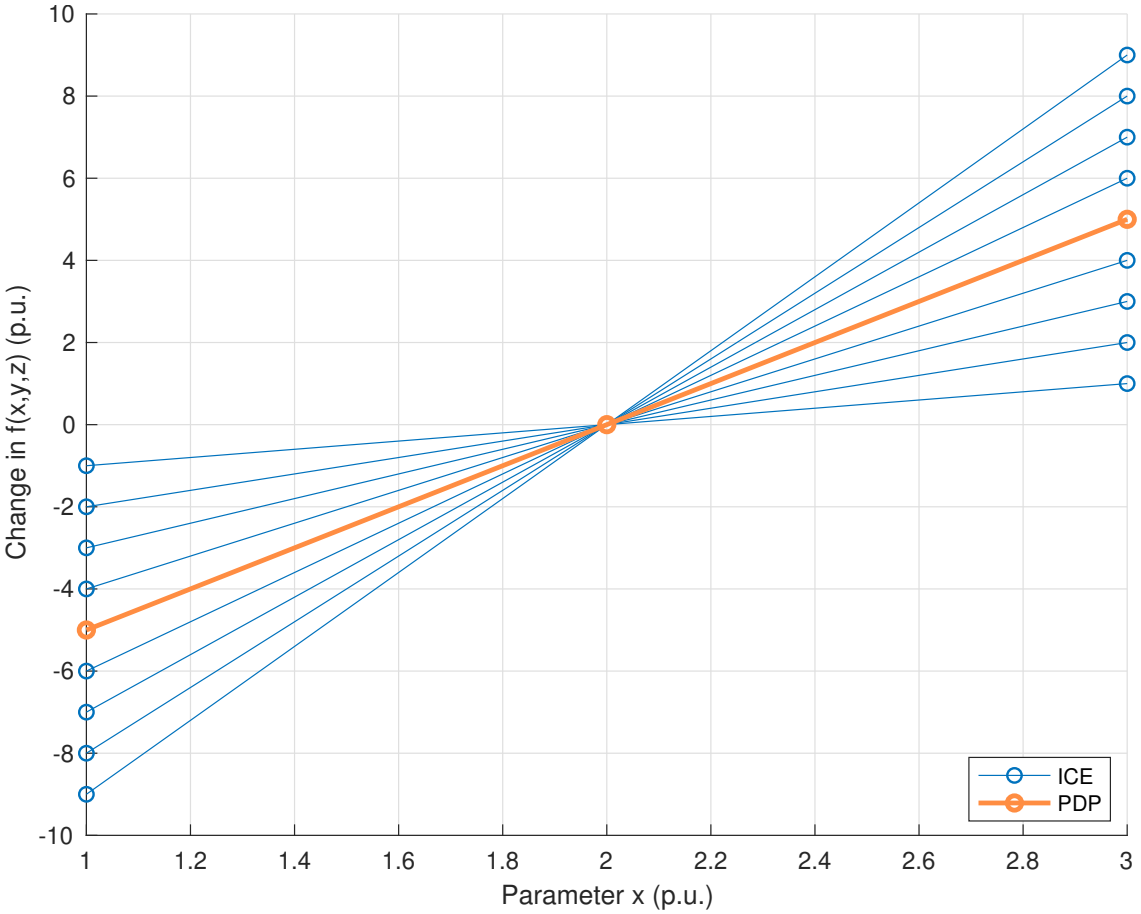


Figure A.3: Individual conditional expectation plot for $f(x, y, z)$ on variable $x$ including a partial dependence plot.

```
figure;
individualConditionalExpectationPlot(...
focusParameterValuesTable,parameterSetsTable,fTable,...
'includePartialDependencePlot','centered','-o');
```

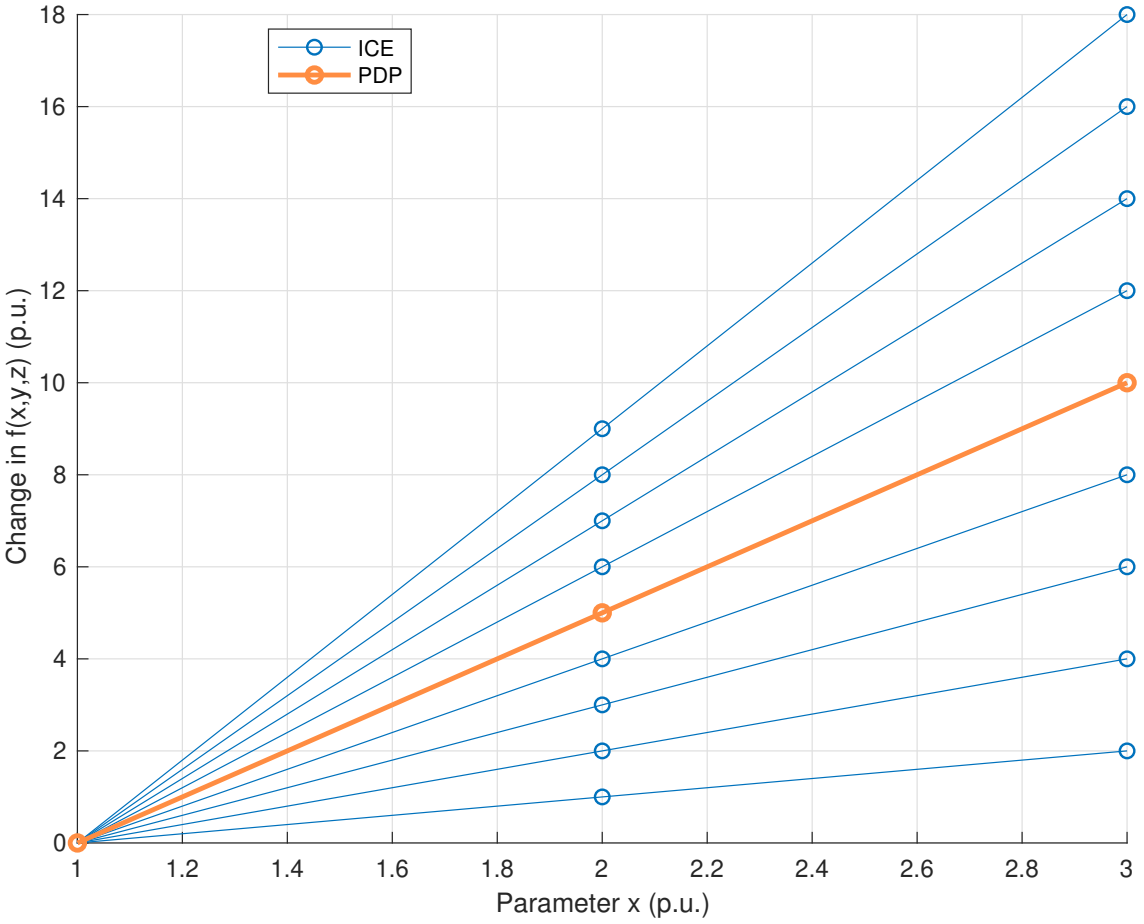


Figure A.4: Individual conditional expectation plot for $f(x, y, z)$ on variable $x$ considering changes from $f(x, y, z)$'s value for the first value considered for $x$ and including a partial dependence plot.

# Appendix B

# Hydraulic turbine and governor LFC model implementation

The hydraulic turbine and governor LFC model was discretized and embedded in a microcontroller. The developed C++ implementation is presented below.

```
1  #include "ControlMath.h"
2  #include "HydraulicTurbineAndGovernorTransferFunction.h"
3
4  HydraulicTurbineAndGovernorTransferFunction::
5  HydraulicTurbineAndGovernorTransferFunction(void)
6  {
7  populateVector(this->pastInputs, 0.0,
       NUMBER_OF_PAST_POWER_DEVIATION_INPUTS);
8  populateVector(this->pastOutputs, 0.0,
       NUMBER_OF_PAST_FREQUENCY_DEVIATION_OUTPUTS);
9  this->samplingFrequencyRatio = 1;
10 this->samplingCounter = this->samplingFrequencyRatio;
11 }
12
13 #if RAM_ALLOCATION
14         __attribute__((ramfunc))
15 #endif
16 long double HydraulicTurbineAndGovernorTransferFunction::
17 calculateFrequencyDeviation(float powerInputDeviation)
18 {
19 if (this->samplingCounter == this->samplingFrequencyRatio)
20 {
21         this->samplingCounter = 1;
```

```
22
23          long double frequencyDeviation =
24          3.98596847962201e+000L * this->pastOutputs[0]
25          - 5.95793210690060e+000L * this->pastOutputs[1]
26          + 3.95795873396686e+000L * this->pastOutputs[2]
27          - 985.995106701793e-003L * this->pastOutputs[3]
28          + 326.744907949934e-006L * this->pastInputs[0]
29          - 975.751298153621e-006L * this->pastInputs[1]
30          + 971.280579328338e-006L * this->pastInputs[2]
31          - 322.274188480890e-006L * this->pastInputs[3];
32
33          updatePastValuesArray(this->pastOutputs,
34          NUMBER_OF_PAST_FREQUENCY_DEVIATION_OUTPUTS,
35                              frequencyDeviation);
36          updatePastValuesArray(this->pastInputs,
37          NUMBER_OF_PAST_POWER_DEVIATION_INPUTS,
38                              powerInputDeviation);
39 }
40 else
41 {
42          this->samplingCounter++;
43 }
44
45 return this->getOutput();
46 }
47
48 void HydraulicTurbineAndGovernorTransferFunction::
49 setSamplingFrequencyRatio(unsigned int
50 samplingFrequencyRatio)
51 {
52 this->samplingFrequencyRatio = samplingFrequencyRatio;
53 this->samplingCounter = this->samplingFrequencyRatio;
54 }
55
56 void HydraulicTurbineAndGovernorTransferFunction::reset(void
       )
57 {
58 populateVector(this->pastInputs, 0.0,
     NUMBER_OF_PAST_POWER_DEVIATION_INPUTS);
```

```
59 populateVector(this->pastOutputs, 0.0,
     NUMBER_OF_PAST_FREQUENCY_DEVIATION_OUTPUTS);
60 this->samplingCounter = this->samplingFrequencyRatio;
61 }
62
63 #if RAM_ALLOCATION
64         __attribute__((ramfunc))
65 #endif
66 long double HydraulicTurbineAndGovernorTransferFunction::
67 getOutput(void)
68 {
69 return this->pastOutputs[0];
70 }
71
72 populateVector( long double *input,
73 long double value,
74 unsigned int length)
75 {
76 for (unsigned int i = 0; i < length; i++)
77 {
78         input[i] = value;
79 }
80 }
81
82 updatePastValuesArray(  long double * pastValuesArray,
83 unsigned int arrayLength,
84 long double latestValue)
85 {
86 for (unsigned int i = arrayLength - 1; i > 0; i--)
87 {
88         pastValuesArray[i] = pastValuesArray[i - 1];
89 }
90
91 pastValuesArray[0] = latestValue;
92 }
```